Evidence for methane hydrate stability zones during Pleistocene glaciation at the Bruce Nuclear Site

by

Michael Takeda

A thesis
presented to the University of Waterloo
in fulfillment of the
thesis requirement for the degree of
Master of Applied Science
in
Civil Engineering

Waterloo, Ontario, Canada, 2013

Abstract

A gas hydrate refers to the state in which hydrogen-bonded water molecules form a rigid lattice structure of so-called ‘cages’, wherein ‘guest’ molecules of natural gas are entrapped. Not unlike ice, gas hydrates are prone to form at low temperatures and high pressures; however, their crystalline structure allows them to remain stable at temperatures and pressures under which the phase limits of ice would otherwise be exceeded. To date, a number of instances of gas hydrates forming in the subsurface of Arctic climates below layers of permafrost have been identified, however the challenge of identifying past occurrences of methane hydrates during episodes of global cooling and glacial advance remains relatively unmet. During these periods of glacial/permafrost cover, the presence of hydrates could have a significant impact on the groundwater flow system due to the significant reduction of the porosity and permeability of hydrate saturated sediments. The purpose of this study is to investigate whether there is evidence to suggest that methane hydrates could have formed in the sedimentary units of the Michigan Basin at the Bruce nuclear site near Kincardine, Ontario, particularly when subjected to the impacts of glacial ice sheet loading. This study aims to provide insight into whether the potential impact of gas hydrates should be considered in the design of the proposed deep-geologic repository (DGR) for low- and intermediate-level nuclear waste.

This study presents a framework employing regional-scale numerical modelling to estimate the evolution of temperature, pressure and salinity profiles across the study area, combined with thermodynamic predictive modelling to identify potential paleo- methane hydrate stability zones in the subsurface at the Bruce nuclear site. This study represents the first step to ultimately assess the extent of paleo-methane hydrates and their impact on subsurface conditions at the site. Transient subsurface conditions at the Bruce nuclear site were modelled over a period of 120,000 years (120 ka), encompassing episodes of glacial advance and retreat during the Pleistocene epoch. The spatial and transient outputs from numerical modelling of the study area were then used as inputs to thermodynamic predictive modelling of methane hydrate stability.

The results of this study show that, based upon the subsurface temperature, pressure and salinity histories determined using a three-dimensional regional-scale numerical modelling approach, paleo- conditions at the Bruce nuclear site become conducive with methane hydrate stability during the study period. Two separate episodes of methane hydrate stability were identified - lasting from 62.5 to 56 thousand years before present (kaBP) and from 23 to 13.5 kaBP, respectively - which were found to correspond to periods of glacial advance across the study area. The vertical extent of the estimated hydrate stability zones varied across the site, however it generally followed the limits of the Upper Silurian units, penetrating to deeper elevations towards the south west end of the study area.

Acknowledgements

There are many individuals to whom I owe a great deal of thanks for what has been a truly formative experience these past years of graduate studies. While many of them are, herein, unjustly relegated to the anonymous groupings of “friends” and “family”, let it be said that without them, this modest accomplishment of mine would not be what it is, nor I who I am – both of which I am as proud of as I would dare to admit.

* * *

There are those who are well-deserving of special recognition for their contributions to my research. To this end, I would like to thank my advisor, Professor Jonathan Sykes, for his faith and encouragement from the very start of this research, as well as Stefano Normani and Yong Yin for their selfless patience and support. I am incredibly grateful for the time and energy you have all donated to my work, and for the inspiration you have afforded me as I move onto my next.

I would also like to thank my like- and unlike-minded support team of friends and peers that have made this extended journey through academia that much more insightful and enjoyable. Finally, I thank my family for their endless love and support, and for having the patience to allow me to play the “student card” for nearly a quarter-century.

Table of Contents

List of Tables

List of Figures

Chapter 1

Introduction

A gas hydrate refers to the state in which hydrogen-bonded water molecules form a rigid lattice structure of so-called ‘cages’, wherein ‘guest’ molecules of natural gas are entrapped. These crystalline lattices occur as three types of structures - called I, II and H - of which structure I is the most commonly occurring in nature with methane being the most common guest molecule. Not unlike ice, gas hydrates are prone to form at low temperatures and high pressures; however, their crystalline structure allows them to remain stable at temperatures and pressures under which the phase limits of ice would otherwise be exceeded (Carroll, 2009). Based on their physical properties, gas hydrates can be regarded as dense non-flowing solids containing highly concentrated amounts of natural gas - greater than 150 volumes of gas per hydrate volume (Sloan Jr and Koh, 2007). These properties have stimulated a growing body of contemporary research motivated by a variety of industrial and scientific interests, ranging from the formation of gas hydrates in oil and gas pipelines and their negative implications on gas conveyance, to the natural occurrence of gas hydrates in subsurface terrestrial environments and ocean sediments of the continental margins, which are regarded as potentially viable sources of energy and are believed to play a significant role in global climate change (Dickens, 2003).

The naturally occurring gas hydrates in subsurface sediments - which are the focus of this study - are predominantly host to methane gas and are believed to represent more than 98% of the methane gas resources on Earth. Moreover, the abundance of methane hydrate is, even by conservative estimates, considered to be equivalent to double the mass of all other fossil fuels (Sloan, 2003), representing a potentially massive resource for natural gas energy, and drawing increasingly more attention from governments and energy suppliers around the world. In addition, a number of researchers have proposed - quite convincingly - that the cataclysmic dissociation of massive natural gas hydrate reservoirs in the ocean sediments could have been the cause for dramatic climate change episodes in the Earth's past. Dickens et al. (1995) cites this as the cause for the Latest Paleocene Thermal Maximum (LPTM), during which a sudden 4°C increase in the ocean water temperature occurred over a span of $<10^4$ years approximately 55 million years ago. This event was proceeded by two larger events - the Early Toarcian Ocean Anoxic Event (OAE) (183 million years ago) and the Early Aptian Event (OAE) (120 million years ago) - which were believed to have released approximately 5000 and 3000 gigatonnes of methane, respectively, and increase the land surface temperature by as much as 2 to 3 °C (Beerling et al., 2002; Hesselbo et al., 2000). While the risk of another large-scale dissociation event is certainly deserving of scientific attention, it is the changes in environmental conditions that bring about these dissociation events that are of particular concern for this study - more specifically those that take place in terrestrial sediments within regions subject to permafrost and glacial cover.

To date, a number of instances of gas hydrates forming in the subsurface below layers of permafrost have been identified (Dallimore et al., 2005; Yakushev and Chuvilin, 2000; Collett et al., 1990), while the challenge of identifying past occurrences of methane hydrates during episodes of global cooling and glacial advance remains relatively unmet. The impacts of global cooling and glacial advance are understood to encourage the stabilize the formation of hydrates in terrestrial polar regions as a result of the lower temperatures and the increased pressures imparted on the subsurface pressure regime (Kvenvolden, 1998). During these periods of glacial/permafrost cover, the presence of hydrates in subsurface sediments could have a significant impact on the groundwater flow system, due to the significant reduction of the porosity and permeability of hydrate saturated sediments, resulting in the obstruction of glacial melt water penetration (Stotler et al., 2010). The impact of hydrates on the evolution of groundwater chemistry can also be significant, not only due to the inhibition of freshening effects by melt water intrusion, but also by the preferential exclusion of solutes, accumulation of gases and fractionation of isotopes that occur during hydrate formation. The challenge of identifying past occurrences of hydrates during these events (termed "paleo-hydrates") in the subsurface sediments arises because dissociated hydrates leave few uniquely definitive markers as to their spatial and temporal extent that are preserved in the geologic time frame of major glacial episodes (Lorenson et al., 2005).

1.1 Research Objectives

The purpose of this study is to investigate whether there is evidence to suggest that methane hydrates could have formed in the sedimentary rock of the Michigan Basin at the Bruce nuclear site – specifically during the advance of glacial ice sheets across the region. This work is being undertaken in support of the Nuclear Waste Management Organization's (NWMO's) proposed deep-geologic repository (DGR) located at a proposed depth of approximately 680 mBGS.

The formation of gas hydrates in the subsurface at the site of the proposed DGR could have significant implications for the proposed repository, potentially altering the present understanding of the natural barrier afforded by the deep geosphere hydrogeologic system. In addition, the impact of gas hydrates on engineered barriers (shafts and seals) may need to be considered, as large volumes of dissociating gas hydrates could result in drastic increases in pressure McIver (1982).

The motivation of this research is therefore to establish whether there is sufficient evidence for the presence of methane hydrates during the site's history to warrant further consideration in the design of the proposed DGR. This study will be undertaken using a framework employing regional-scale numerical modelling and thermodynamic predictive modelling to identify potential paleo- methane hydrate stability zones within the subsurface. This study will also consider present day measurements of methane gas and solute distributions across the study site to evaluate whether residual hydrate dissociation signatures could have persisted, which might be used to corroborate the predictive modelling results.

1.2 Research Scope

The study area is located at Ontario Power Generation's (OPG's) proposed Deep Geologic Repository (DGR) at the Bruce nuclear site in the Municipality of Kincardine, Ontario (Figure 1.1). This study considers transient subsurface conditions over a period of 120 thousand years (ka), encompassing several glacial episodes during the Pleistocene epoch. Since this period is typically characterised by lower subsurface temperatures due to surface cooling, and periods of increased pressures from overlying ice sheets, conditions were ostensibly more conducive to the formation of gas hydrates.

Regional numerical modelling of the study area shown in Figure 1.1 is undertaken using FRAC3DVS-OPG. Developed from the analytical software FRAC3DVS (Therrien et al., 2003), this model provides a solution to three-dimensional density-dependent groundwater flow and solute transport equations in porous and discretely-fractured media. FRAC3DVS-OPG's one-dimensional hydromechanical coupling capabilities also enable the simulation of transient flow affected by the surface loading conditions during the advance and retreat of glacial cycles (Guvanasen, 2007; Neuzil, 2003).

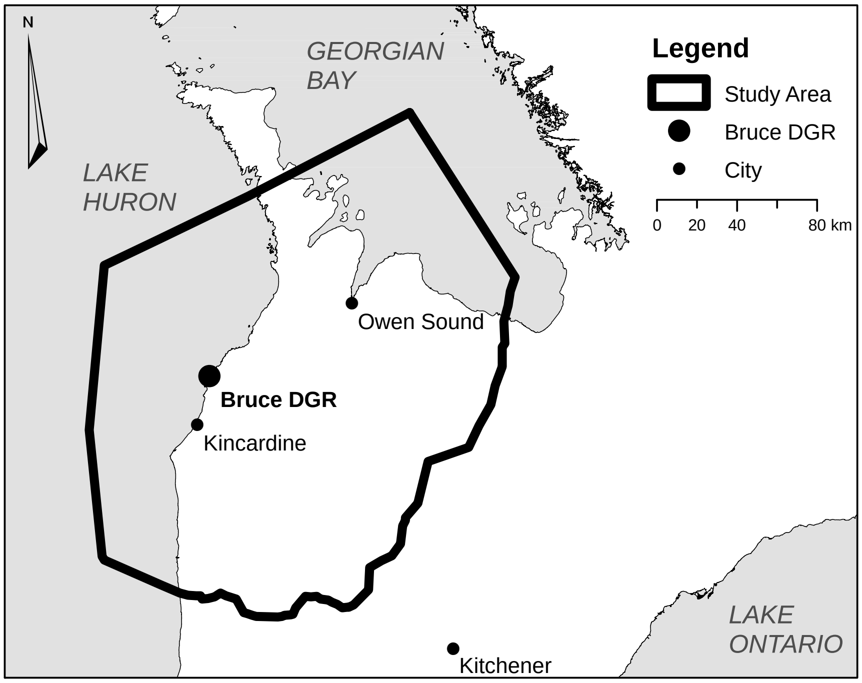

Figure 1.1: Location of the Bruce nuclear site and study area.

The formation of gas hydrates is limited to the locations where (1) the required pressure and temperature conditions for a given aqueous system are such that the equilibrium point between the hydrate, liquid and free-gas phases (called three-phase equilibrium point) is reached or exceeded; and (2) where the abundance of methane is sufficient to exceed the local solubility. As illustrated in Figure 1.2, gas hydrates are stable in the region where the temperature is below the phase boundary at a given pressure (expressed in terms of depth in Figure 1.2). When pressure-temperature conditions are outside of this boundary, gas exists either as free gas or as dissolved gas.

Thermodynamic models proposed by Duan and Mao (2006) and Sun and Duan (2007) are used to determine the solubility of methane gas and the conditions for methane hydrate formation across the study area, respectively. The inputs required for the thermodynamic modelling of methane solubility and methane hydrate stability are generated in this study by combining the independently-run transient three-dimensional temperature model output, with the pressure and salinity outputs from the base-case regional-scale model prepared by Sykes et al. (2011). Not considered in this study are the impacts of sediment porosity on the thermodynamics of methane hydrate stability, which has been recognized as having an inhibitive impact on formation of gas hydrates (Dallimore et al., 2005).

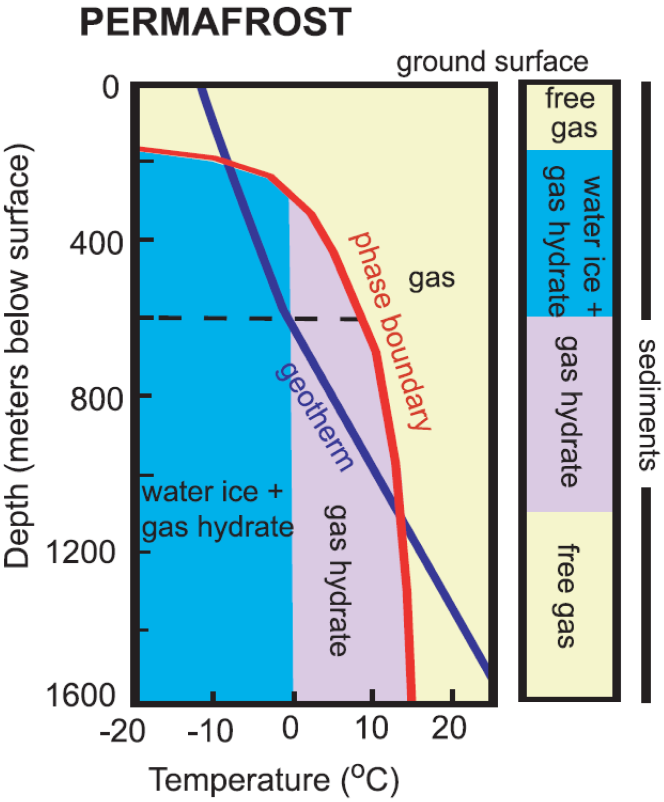

Figure 1.2: Example of pressure-temperature relationship for phase boundary of methane hydrate stability in a permafrost environment. Illustration from Ruppel (2007).

In this study, the formation of methane is expressed in terms of a threshold hydrate stability pressure that must be exceeded in order for methane hydrates to form at a given temperature and salinity. Methane saturation pressure was not incorporated into this hydrate pressure threshold (contrary to Figure 1.2) in an attempt to isolate potential sources of error from unreliable methane distribution data. While this study does attempt to evaluate whether methane is available in sufficient quantities to exceed local solubility (and thus permit hydrate formation), because methane migration/formation was not modelled and present-day formation methane concentration data is of limited availability for the study area (Figure 1.1), comparison with theoretical methane solubility calculations is of limited reliability; however, in recognition of the importance of this step as a necessary component in estimating the extent of hydrate stability zones, it has therefore been included in the framework provided by this study, with the expectation that it be improved upon in future work.

Chapter 2

Background

The following sections are included to provide the reader with a background understanding of the geologic and hydrogeologic characteristics of the Bruce nuclear site, including the site hydrogeochemistry with respect to solute and isotope distributions, and the presence and origin of methane gas within the sedimentary lithologies. Information regarding naturally occurring methane hydrate is also provided in the chapter, with particular emphasis placed on those that form in terrestrial sediments.

2.1 Geological Setting

The Michigan Basin (Figure 2.1) is a roughly circular intracratonic basin bounded by the southwest-northeast trending Findlay/Algonquin arches to the southeast, which acts as the boundary between the Michigan Basin and the Appalachian Basin. The Chatham Sag is a structural low point that separates the Findlay and Algonquin Arches. The Michigan Basin is further bounded by the northwest-southeast trending Frontenac arch to the northeast, and by the southwest-northeast trending Fraserdale arch on the northwestern flank. Like much of south-western Ontario, the study site is underlain by sequences of Paleozoic sedimentary rocks of Upper Cambrian ($\sim$510 million years (Ma)) to Devonian (354 Ma) age, resting unconformably upon a Precambrian basement (ca. 1600-540 Ma) (Figure 2.2 - 2.4). The succession of Paleozoic sedimentary rock atop this basement material thins from a maximum thickness of approximately 4,800 m at the centre of the basin, to approximately 850 m at the study site, located on the flank of the Algonquin arch. A geologic cross-section of the Michigan Basin is presented in Figure 2.3 and again in Figure 2.4, the latter of which focusses on the sedimentary sequences in the vicinity of the study area as they pinch out against the Algonquin arch.

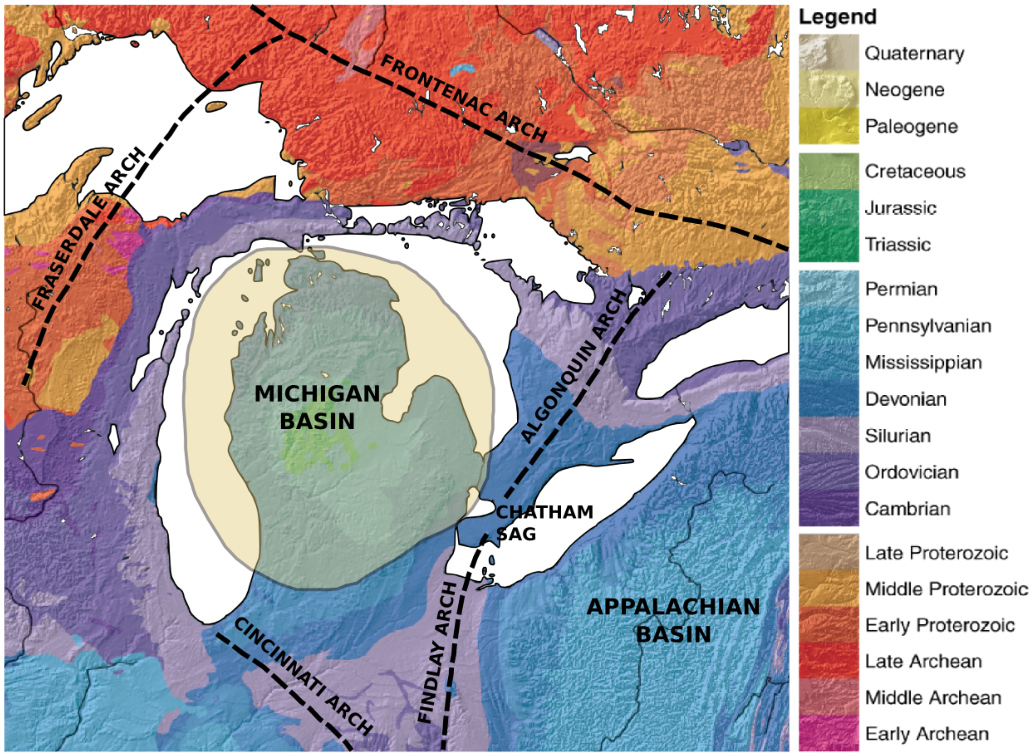

Figure 2.1: Location of the Michigan Basin and bounding Findlay, Algonquin, Frontenac, Cincinnati and Fraserdale Arches. Geologic map shaded based on geologic ages from Quaternary to Archean is adapted from the United States Geologic Survey (Barton et al., 2003).

The sedimentary strata that dominate the lithology below the study site are presented in Figure 2.5 using the generally accepted stratigraphic nomenclature. Also presented in Figure 2.5 are the Paleozoic strata encountered toward the basin centre and in the Appalachian Basin to the west. For ease of conceptualization and discussion, the stratigraphic units at the site can be grouped into three horizons based upon their hydrogeologic characteristics - a shallow zone, an intermediate zone, and a deep zone - which are discussed in the following sections.

Tables 2.1-2.3 present the thicknesses of the sedimentary rock formations of the Michigan Basin for the deep, intermediate and shallow hydrogeologic zones, respectively. The

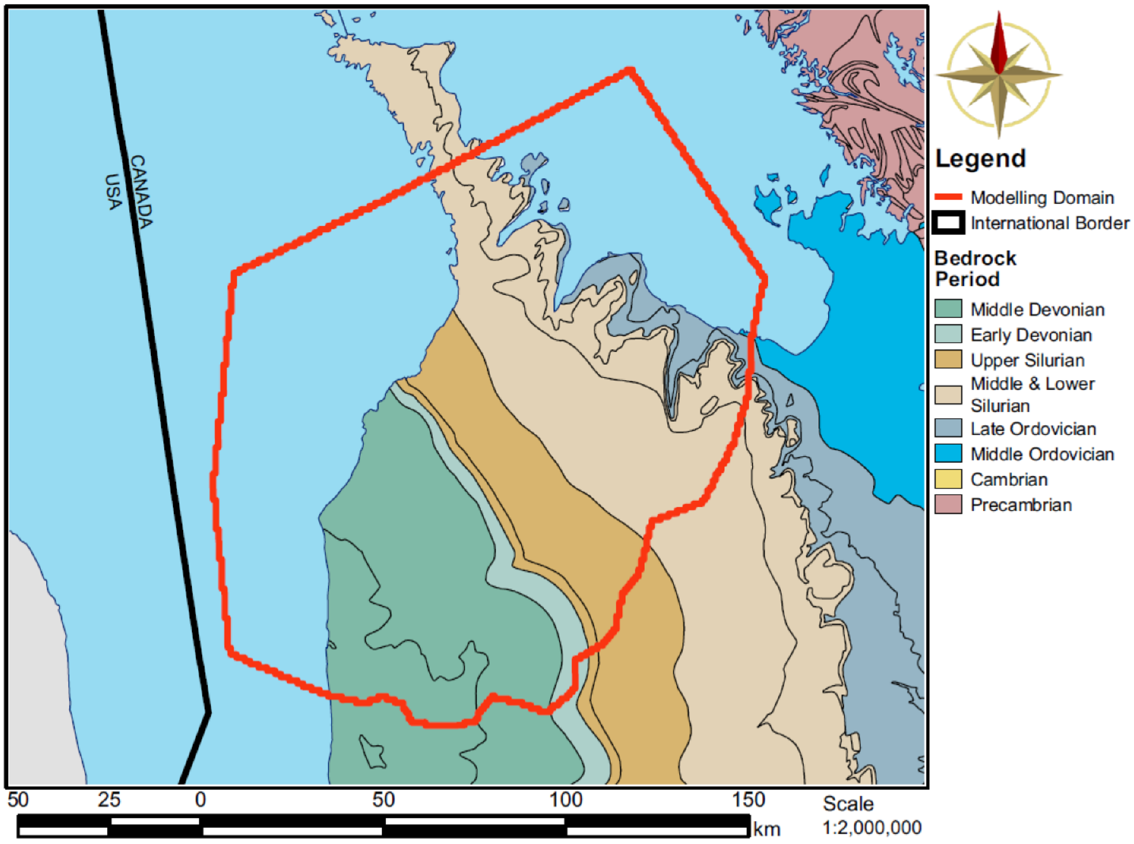

Figure 2.2: Paleozoic bedrock geology map for the Bruce Nuclear Site. Modified from the Ontario Geologic Survey dataset (Armstrong and Dodge, 2007).

mean thicknesses for the basin stratigraphy in southern Ontario were generated from the Oil, Gas and Salt Resources (OGSR) Petroleum Wells Subsurface Database, which were used in the development of the ITASCA Canada and AECOM (2011) geologic framework model. For comparison, the observed formation thicknesses from the DGR-1 and DGR-2 site exploration boreholes, as provided by INTERA (2011), are also included in Tables 2.1-2.3.

Deep Hydrogeologic Zone

The deep zone extends down to the Precambrian basement of the basin and is comprised of the very low permeability shales and carbonates of the Upper and Middle Ordovician

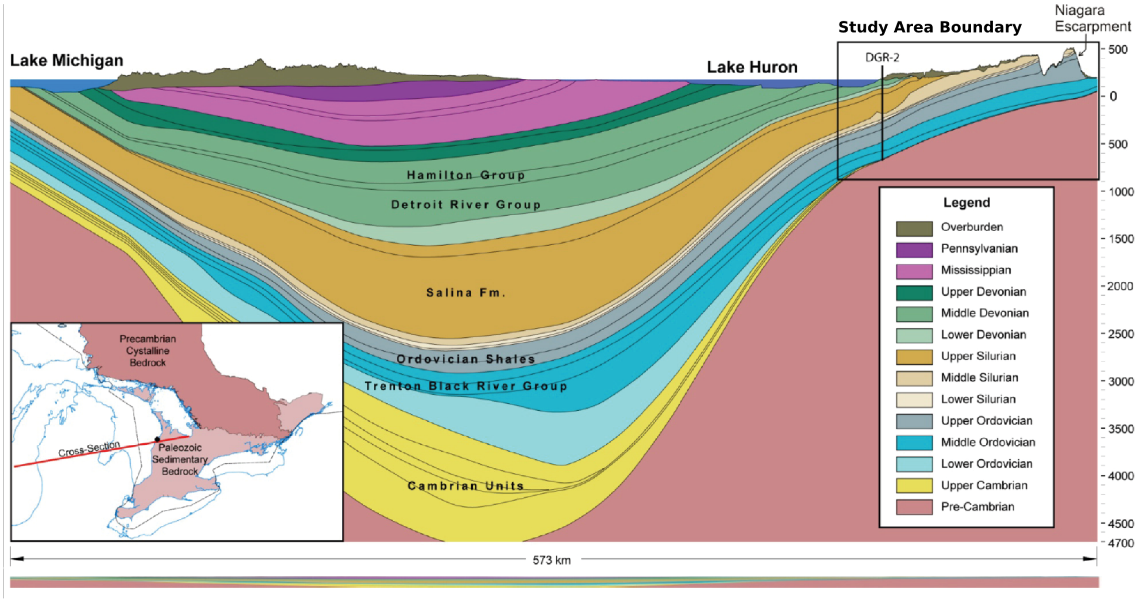

Figure 2.3: Geologic cross-section of Michigan Basin. The approximate limits of the study area are delineated at the upper right corner of the figure along with exploratory borehole DGR-2. The vertical exaggeration is approximately ×45. An unexaggerated cross-section is provided below the main figure. Modified from the Nuclear Waste Management Organization Geosynthesis Report (Al et al., 2011).

units, respectively, and the comparatively high permeability Cambrian sandstones and dolostones. The Precambrian bedrock below the study area is composed of gneiss and metamorphic rocks of the Grenville Province within the Central Gneiss Belt of the Canadian Shield. An alteration zone of several metres in thickness exists atop the Precambrian bedrock (Ziegler and Longstaffe, 2000), which is believed to cause local increases in porosity and permeability along the contact zone with the overlying Cambrian unit (Armstrong and Carter, 2010).

The Cambrian deposits that overlie the Precambrian basement are considered to be a succession of (in ascending order) marine sandstones, sandstones and dolostones and dolostones (Al et al., 2011). These units are present across both the Michigan and Appalachian basins, however post-depositional erosion along the Algonquin Arch has resulted in the gradual pinching out of these units along the edges of the Michigan Basin. Regionally occurring sandstones and sandy dolostone give this unit a significantly higher permeability than its surrounding units (Armstrong and Carter, 2010). However, because this unit pinches out against the Precambrian basement along the Algonquin Arch and due to the

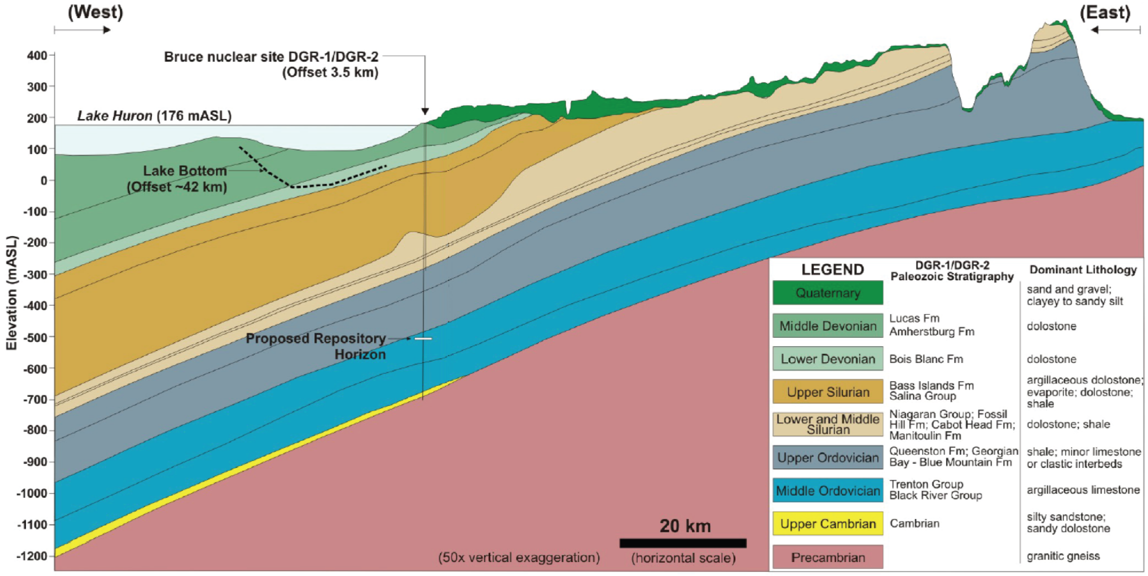

Figure 2.4: Geologic cross-section of Michigan Basin at the Study Site. Modified from the Nuclear Waste Management Organization Geosynthesis Report (Al et al., 2011).

overlying low permeability Ordovician carbonates, this unit is likely hydrologically isolated from its surrounding units.

The Middle Ordovician carbonate-dominated package is divided into the Black River Group and the overlying Trenton Groups. The Black River Group consists of (in ascending order) the Shadow Lake, Gull River and Coboconk Formations and is believe to range in thickness from 10 m along the erosional edge to 150 m toward the basin centre (Armstrong and Carter, 2010). The Shadow Lake Formation is composed of poorly sorted sandy shales, and argillaceous sandstones and dolostones that unconformably overlie the Precambrian basement or (where present) the Cambrian units. The presence of more porous sandstones in the Shadow Lake Formation likely causes local increases in permeability and could allow more communication between this unit and the underlying Cambrian (Armstrong and Carter, 2010). The overlying Gull River Formation is composed primarily of very fine-grained limestone with minor shale and dolostone interbeds. The Coboconk, at the top of the Black River Group, is composed of fine- to medium-grained bioclastic limestone (Al et al., 2011).

The overlying Trenton Group includes (in ascending order) the Kirkfield, Sherman Fall, and the Cobourg Formations and is considered to range to 170 m in thickness (Armstrong and Carter, 2010). The Kirkfield Formation is composed of very fine- to fine-grained fos-

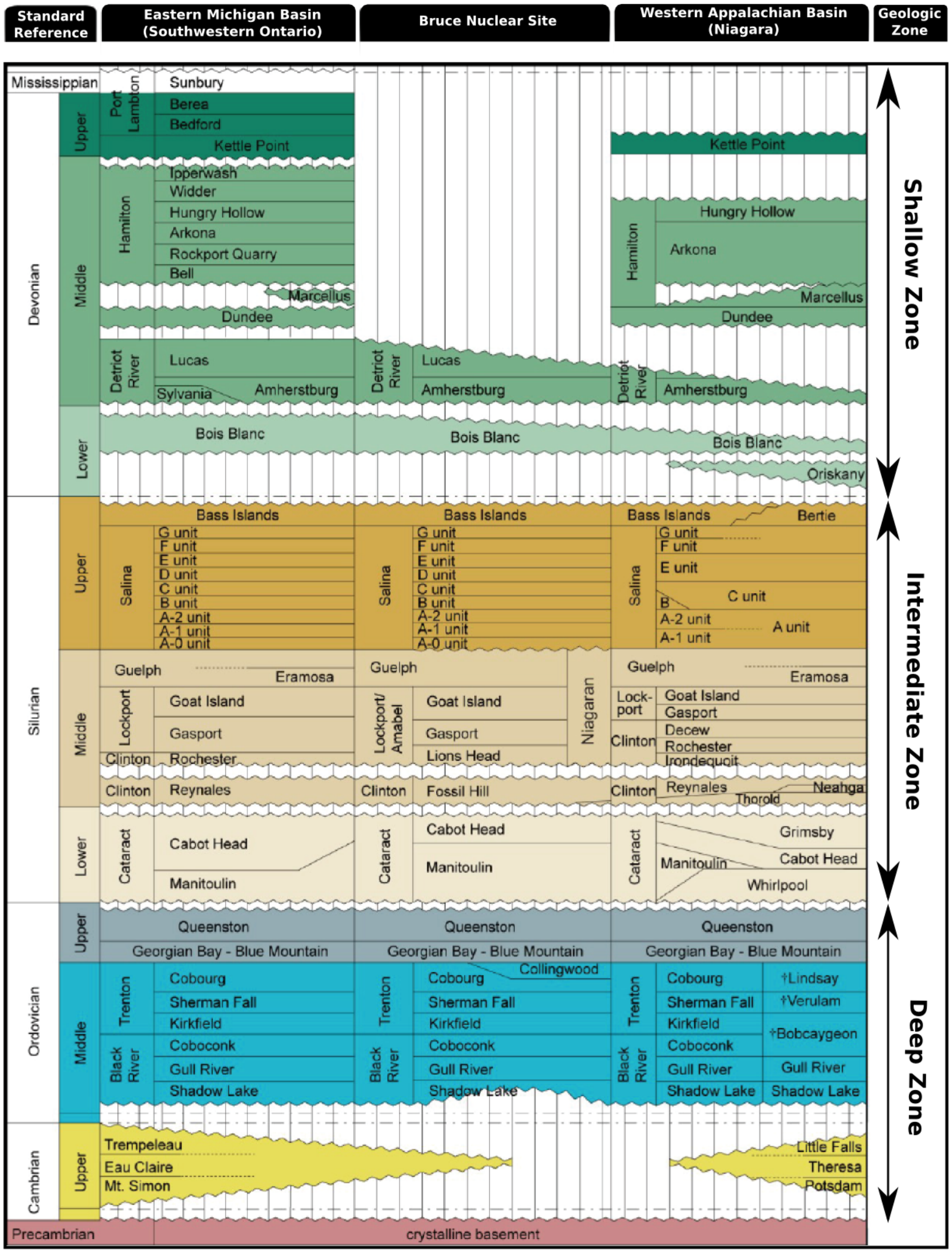

Figure 2.5: Paleozoic stratigraphic nomenclature for the Michigan and Appalachian Basins in southern and eastern Ontario. Modified from the Nuclear Waste Management Organization Geosynthesis Report (Al et al., 2011) based on figure from (Armstrong and Carter, 2006).

siliferous limestone with interbeds of green shale that become more limited shallower in the formation. The Sherman Fall Formation overlies the Kirkfield, and is characterized by an upper "fragmented" region of medium- to coarse-grained tan to light-grey fossiliferous limestone that overlies a lower argillaceous and bioclastic region of fine- to coarse-grained limestone. The Cobourg Formation is the shallowest of the Trenton Group, and is composed of bluish-grey to brown-grey limestone and argillaceous limestone. A dark-grey to black calcareous shale cap - referred to as the Collingwood Member - lies overtop of the Cobourg Formation. Although there is evidence to suggest that this shale-cap becomes quite discontinuous beyond the basin margins, the organic rich nature of this shale unit suggests that natural gas could be present where the Collingwood Member subcrops beneath glacial drift (Armstrong and Carter, 2010).

The extensive Upper Ordovician shale units are composed of the Blue Mountain and Georgian Bay Formations consisting of thick non-calcareous shales with minor limestone, sandstone and siltstone interbeds, overlain by the younger Queenston shale characterized by calcareous to non-calcareous shale with minor limestone and siltstone interbeds. Due to the close similarity between the lower two shale units of the Upper Ordovician package, the Georgian Bay Formation is poorly differentiated from the underlying Blue Mountain Formation (Armstrong and Carter, 2010).

Intermediate Hydrogeologic Zone

The intermediate zone is comprised of the lithological units of Silurian age that overlie the Ordovician sedimentary strata. These Silurian age units are subdivided based on the traditional convention used by Johnson et al. (1992) into Upper, Middle and Lower Silurian packages corresponding to general lithological characteristics: the Lower Silurian is characterized by alternating intervals of sandstone, shale and limestone; the Middle Silurian contains predominantly carbonate-dominated strata; and the Upper Silurian package contains alternating intervals of evaporites, carbonates and shales (Armstrong and Carter, 2010).

The low permeability Lower Silurian package consists of the Manitoulin Formation, overlain by the Cabot Head Formation, which comprise a combined thickness of 37 m at the Bruce Site (Al et al., 2011). The Cabot Head Formation consists of predominantly non-calcareous shales that grade with depth to interbedded shale and limestone. The Manitoulin Formation consists of dolostone, shale, and argillaceous dolostone. The Whirlpool Formation, which typically underlies the Manitoulin Formation, irregularly pinches out towards the eastern margin of the Michigan Basin and is not present at the study site (Al et al., 2011).

Table 2.1: Summary of Formation Details for the Geologic Units within the Deep Hydrogeologic Zone

Formation	**Rock Type**	**Thickness at DGR [m]**	**Depth at DGR [m]**
Upper Ordovician			
Queenston	Shale with some dolostone, limestone and siltstone.	70.3	447.6
Georgian Bay/Blue Mtn.	Shale and limestone interbeds.[a]	133.6	518.0
Middle Ordovician			
Cobourg	Limestone with calcareous shale cap.	28.6	659.5
Sherman Fall	Limestone.	28.0	688.1
Kirkfield	Limestone with shale interbeds.	45.9	716.1
Coboconk	Limestone.	23.0	762.0
Gull River	Limestone with shale interbeds.	53.6	785.0
Shadow Lake	Sandy shale, sandstone and dolostone.	5.2	838.6
Cambrian			
(undifferentiated)	Sandstone and dolostone.	16.9	843.8

[a] Calcareous shale cap called the Collingwood Member.

Note: Unit thicknesses and depths based on DGR-1/2 boreholes, respectively (Al et al., 2011).

The Middle Silurian consists locally of the low permeability dolostones of the Fossil Hill, Lions Head, Gasport and Goat Island Formations underlying the more permeable dolostone of the Guelph Formation. The Lions Head, Gasport, Goat Island and Guelph Formations are sometimes collectively referred to as the Niagaran group (Al et al., 2011). The Guelph Formation is generally characterized by sucrosic dolostone, although various depositional facies - ranging from reefal to inter-reefal - exist that dictate the characteristics of the dolostone (Al et al., 2011). The Fossil Hill Formation is a very fine- to coarse-crystalline, very fossiliferous dolostone unit that overlies the Cabot Head Formation of the Lower Silurian package.

The Upper Silurian package includes the Bass Island Formation and the underlying Salina Group. The Salina Group consists of sequences of a cyclically varying lithological units grading upwards from basal carbonates to anhydrites to halite/evaporites with the tops of each evaporite cycle often being marked by shaley strata (Armstrong and Carter, 2006). At the study site, the sequences of the Salina Group are the A-0 unit, A-1 Evaporite, A-1 Carbonate, A-2 Evaporite, A-2 Carbonate, B Unit, C Unit, D Unit, E Unit, F Unit

Table 2.2: Summary of formation details for the Geologic Units within the Intermediate Hydrogeologic Zone

Formation	**Rock Type**	**Thickness at DGR [m]**	**Depth at DGR [m]**
Upper Silurian			
Bass Islands	Dolostone with shale.	70.3	124.0
G Unit	Dolostone with anhydrite.	9.3	169.3
F Unit	Dolomitic shale with dolomite.	44.4	178.6
F Salt	Anhydrite.	[a]	[a]
E Unit	Dolostone, dolomitic shale and argillaceous dolostone interbeds.	20.0	223.0
D Unit	Dolostone with anhydrite.	1.6	243.0
B and C Units	Dolomitic shale, shale, argillaceous dolostone and dolostone.	46.6	244.6
B Unit	Dolostone and anhydrite interbeds.	1.9	291.2
A-2 Unit	Dolostone with dolomitic shale and shale.	26.6	293.1
A-2 Unit	Dolostone and anhydrite interbeds.	5.8	319.7
A-1 Unit	Dolostone and shale interbeds with anhydrite.	41.5	325.5
A-1 Unit	Dolostone and anhydrite interbeds.	3.5	367.0
Middle Silurian			
Guelph	Dolostone with shale.	4.1[b]	374.5
Goat Island	Dolostone.	18.8[b]	378.6
Gasport	Dolomitic limestone.	6.8[b]	397.4
Lions Head	Dolostone.	4.4[b]	404.2
Reynales/Fossil Hill	Dolostone.	2.3	408.7
Lower Silurian			
Cabot Head	Shale to shale/limestone interbeds.	23.8	411.0
Manitoulin	Dolostone, shale and argillaceous dolostone.	12.8	434.8

[a] Formation not present at site.

[b] Comprises part of Niagaran Group (Mean Thickness = 55 m, DGR Thickness = 34.1 m) (INTERA, 2011).

Note: Unit thicknesses and depths based on DGR-1/2 boreholes, respectively (Al et al., 2011).

and G Unit. A description of each of these lithologies is provided in Table 2.2. The A-0 Unit is a thin limestone/dolostone sequence overlying the Guelph Formation that is poorly mapped in Ontario (Armstrong and Carter, 2010) and was not identified at the study site. The Bass Island Formation represents the youngest of the Silurian age sedimentary sequences at the site and consists of dolostone with minor shale that conformably overlies the Salina Group. The evaporite and shale units of the Salina Group are characterised as low permeability layers and generally act as a major barrier impeding vertical hydraulic connection between the shallow groundwater regime and the deep hydrogeologic zone. It should be noted that the Bass Island and Salina A Upper Carbonate units are notable exceptions, having hydraulic conductivities 5 to 6 orders of magnitude higher than the surrounding Salina units (INTERA, 2011).

Shallow Hydrogeologic Zone

The shallow zone is comprised of the dolomite and limestone units of the Devonian units, which are generally characterized by relatively high permeabilities compared to the units of the intermediate and deep hydrogeologic zones. The Devonian carbonates include the Bois Blanc Formation of the Lower Devonian and the overlying Detroit River Group of the Middle Devonian, which are both composed primarily of limestone toward the basin centre with localized dolomitization along the Algonquin Arch (including at the study site). The Detroit River Group is composed of the Amherstburg and overlying Lucas formation, which form the bedrock surface below the overburden at the study site (Armstrong and Carter, 2006). Toward the southern portion of the regional domain, the limestones and dolostones of the Middle Devonian Dundee and the interbedded shale and limestone of the Hamilton Group overlie the Detroit River Group.

Glacial drift aquifers that overlie the bedrock units of sedimentary and Precambrian metamorphic rocks are also considered to be part of the shallow hydrogeologic zone. These drift aquifer materials are composed of outwash deposits of sand and gravel, although OGSR borehole data indicate that the thickness of this drift is less than 1 metre for much of the study area (Al et al., 2011). Inclusion of the glacial drift layer in the shallow hydrogeologic zone is a logical assignment as modern groundwater regimes at the study site are primarily limited to migration through glacial moraines and shallow Devonian bedrock aquifers (McIntosh and Walter, 2006), with limited circulation of meteoric waters into the deeper sedimentary formations (Sykes et al., 2011).

Table 2.3 provides a description of the rock types that dominate the sedimentary rock lithologies in the shallow hydrogeologic zone (drift is not presented) as well as their respective thicknesses at the study site. Note that although the younger Dundee, Hamilton

Group and Kettle Point Formations pinch out as they approach the Algonquin Arch and were not encountered by exploratory boreholes DGR-1 and DGR-2 (located at the Bruce Site), these formations are present to the southwest of the Bruce nuclear site within the study area.

Table 2.3: Summary of formation details for the Geologic Units within the Shallow Hydrogeologic Zone

Formation	**Rock Type**	**Thickness at DGR [m]**	**Depth at DGR [m]**
Upper Devonian			
Kettle Point	Shale and limestone interbeds.	- [a]	- [a]
Middle Devonian			
Hamilton Group	Shale and limestone interbeds.	- [a]	- [a]
Dundee	Limestone and dolostone.	- [a]	- [a]
Lucas	Dolostone with bituminous shale laminae.	10.4[b]	20.0
Amherstburg	Cherty dolostone with bituminous shale laminae.	44.6[b]	30.4
Lower Devonian			
Bois Blanc	Cherty dolostone with bituminous shale laminae.	49	75.0

[a] Formation not present at site.

[b] Comprises part of Detroit River Group (Mean Thickness = 103 m)(INTERA, 2011). Full thickness not present at site.

Note: Unit thicknesses and depths based on DGR-1/2 boreholes, respectively (Al et al., 2011).

2.2 Hydrogeochemistry

Over the geologic history of the Michigan Basin, a number of overlapping mechanisms of fluid migration and solute transport have contributed to gradual and complex evolution of the groundwater/porewater geochemistry. These processes include basinal disturbances during the Taconic, Acadian and Alleghenian orogenic events, evaporation of sea water and downward migration of the resulting hypersaline brines, penetration of glacial melt water during period of ice sheet advance, and extensive rock-water interactions related to diagenic processes and halite formation/dissociation (Al et al., 2011). In general, the hydrogeochemical profile of the formation waters and sedimentary brines at the Bruce nuclear site can be divided into two regions based on their chemical and isotopic characteristics: (1) a deeper region (generally corresponding to the lithologies of the aforementioned deep and intermediate hydrogeologic zone) with hypersaline brines formed during the evaporation of sea water, and (2) a shallow region subjected to glacial melt water and meteoric water penetration (McIntosh et al., 2010). It is worth noting that the hydrogeochemistry at the study site deviates from the lithology-based distinctions used in this section towards the eastern edge of the Michigan Basin, where many of the older formations subcrop along the Algonquin Arch and show signs of freshening due to meteoric water infiltration (Hobbs et al., 2011). The vertical trends in the salinity (TDS) and stable isotopes (δ^{18}O and δ^{2}H) using data from the study site boreholes are presented in Figure **??**. The steep concentration gradient that appears in both the stable isotope and TDS profiles (Figures 2.7 and 2.6, respectively) suggests that the separation between the shallow and deep hydrogeochemical regions occurs within the Salina A1 Unit at the Bruce nuclear site. Furthermore, the persistence of this steep concentration gradient suggests that a significant hydrogeologic barrier exists around this lithological unit, that has limited the interaction between the shallow and deep hydrogeochemical regions.

Figure 2.8 shows the ratio of δ^{18}O and δ^{2}H, where meteoric water and the more isotopically depleted glacial melt water generally plot along the Global Meteoric Water Line (GMWL) and water hypersalinated by evaporation typically falls below the GMWL. These plots support the conceptual model of a deeper hydrogeochemical regime of hypersaline brines subjected to ongoing dilution by meteoric water infiltration in the modern flow system, as well as historical dilution by glacial melt water intrusion during glacial ice sheet advance (Figure 2.9).

The deep zone hydrogeochemistry can be interpreted as being the product of the modification of the original seawater by gradual diffusion of salts from overlying hypersaline brines and prolonged rock-water interactions. A trend of increasingly depleted δ^{18}O with depth (from -5‰ to -8‰), starting in the Upper Ordovician Queenston and Georgian Bay shales, is attributed to the prolonged water-rock interaction processes between the original seawater and the surrounding sedimentary matrix. The smooth decrease in TDS with depth from approximately 300 g/L in the Upper Ordovician Queenston shale to about 200 g/L in the Shadow Lake carbonate can be attributed to the gradual diffusion of salt down from the hypersaline brines of the overlying Lower Silurian formations (Al et al., 2011). In both cases, these trends terminate at the underlying Cambrian Formation, where the concentrations of the natural tracers rebound. This rebound phenomenon has been observed at other locations within the Michigan Basin, and while no definitive explanation yet exists for this trend, it has been suggested that the higher hydraulic conductivity of this unit may have enabled the relatively rapid spatial propagation of a more recent episode of migration

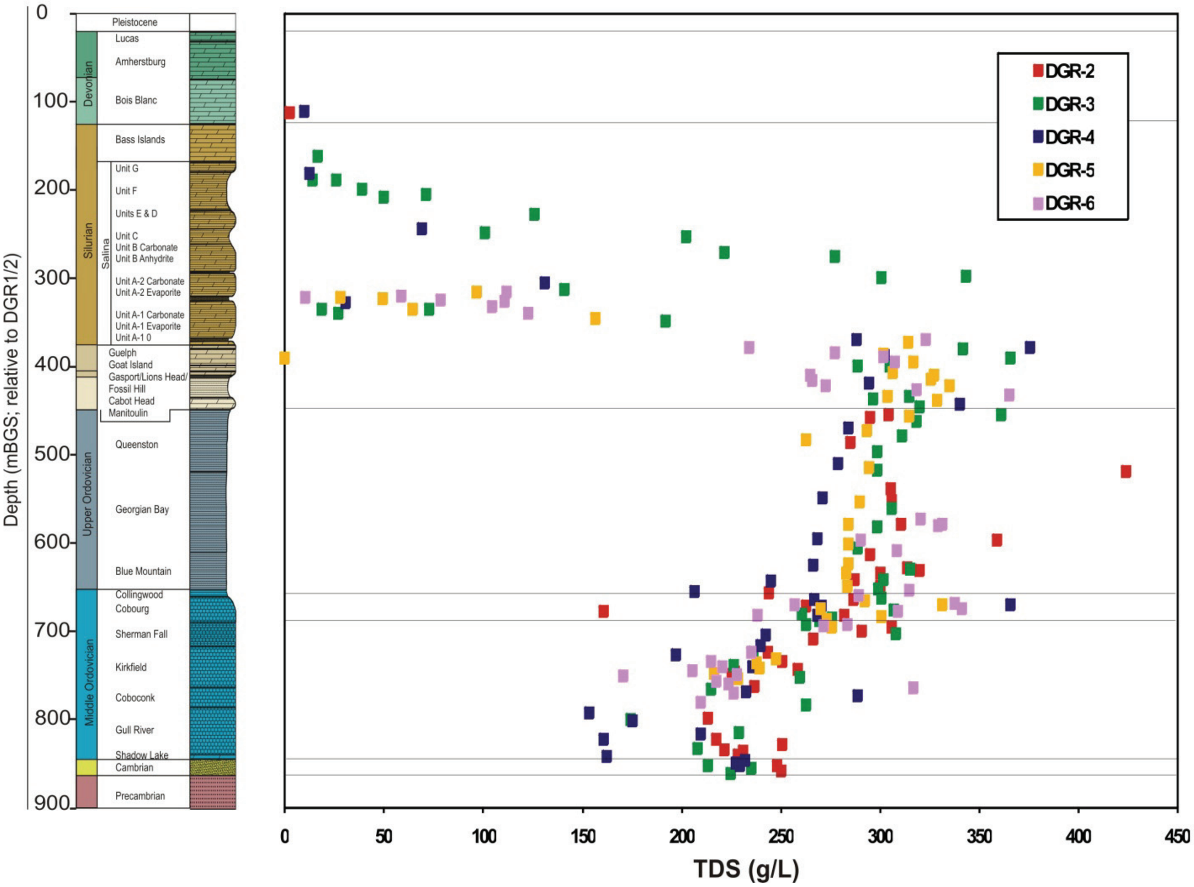

Figure 2.6: Vertical profiles of TDS determined in porewater and groundwater at the Bruce nuclear site. Developed by Al et al. (2011)

of basin brines (Al et al., 2011).

The hydrogeochemistry of the intermediate zone units reflects the onset of more restricted marine conditions during the Silurian period, leading to the formation of hypersaline brines, as well as a variety of post-depositional (and in some cases ongoing) diagenetic processes. The formations of the Middle and Lower Silurian packages at the Bruce Nuclear Site represent locally undiluted regions of concentrated seawater, characterized by high salinities (ranging from approximately 250 g/L to 375 g/L) and enriched δ^{18}O compositions (approximately -6‰ to 1‰), as illustrated in Figure 2.8. In the interval between the top of the intermediate zone and the A1 Carbonate Unit, salinity is generally reduced from the levels present in the underlying hypersaline brines, suggesting subsequent dilution by

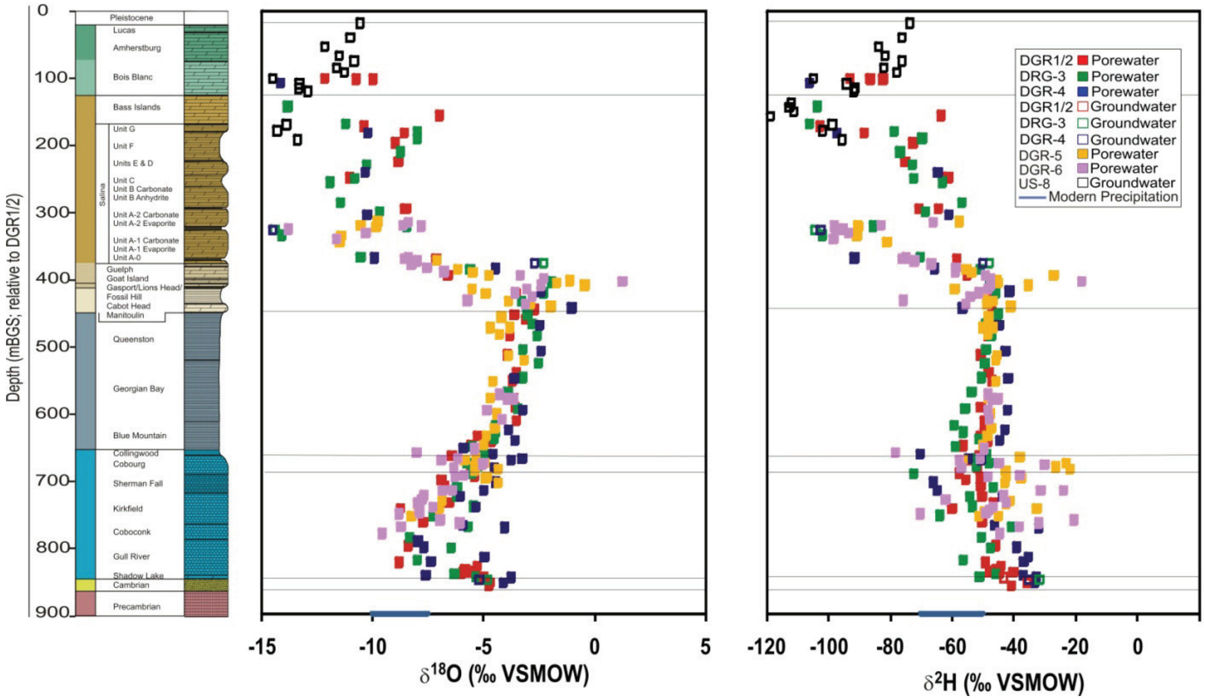

Figure 2.7: Vertical profiles of stable isotopes ($\delta^{18}O$ and $\delta^{2}H$) determined in porewater and groundwater at the Bruce nuclear site. Developed by Al et al. (2011).

meteoric and/or melt water penetration; exceptions can been seen (such as in the B Anhydrite and Carbonate units) throughout this interval, implying that the degree of dilution varies from unit to unit. This interpretation of variable dilution is supported by the stable isotope compositions, which also vary significantly within this interval (ranging from -15‰ to -7‰ for δ^{18}O, and from -120‰ to -60‰ for δ^{2}H). The variability in the stable isotope profiles also eludes to the fact that the sources of the diluting waters have also been inconsistent; where glacial melt water tends to be depleted in ^{18}O and ^{2}H isotopes, meteoric water tends have isotopic compositions closer to present day precipitation (-11‰ to -7.5‰ for δ^{18}O, and -50‰ to -70‰ for δ^{2}H). It is worth noting that the highly depleted stable isotope compositions within the A1 Carbonate Unit at approximately 328.5 metres below ground surface (mBGS) are interpreted to be the extent of glacial melt water penetration at the Bruce nuclear site (Al et al., 2011).

The shallow zone hydrogeochemistry reflects the relatively high exposure of the Devonian sediments to meteoric and glacial melt water dilution. This can been seen from the δ^{18}O (-15‰ to -10‰) and δ^{2}H (-100‰ to -70‰) isotope compositions at the Bruce Nu-

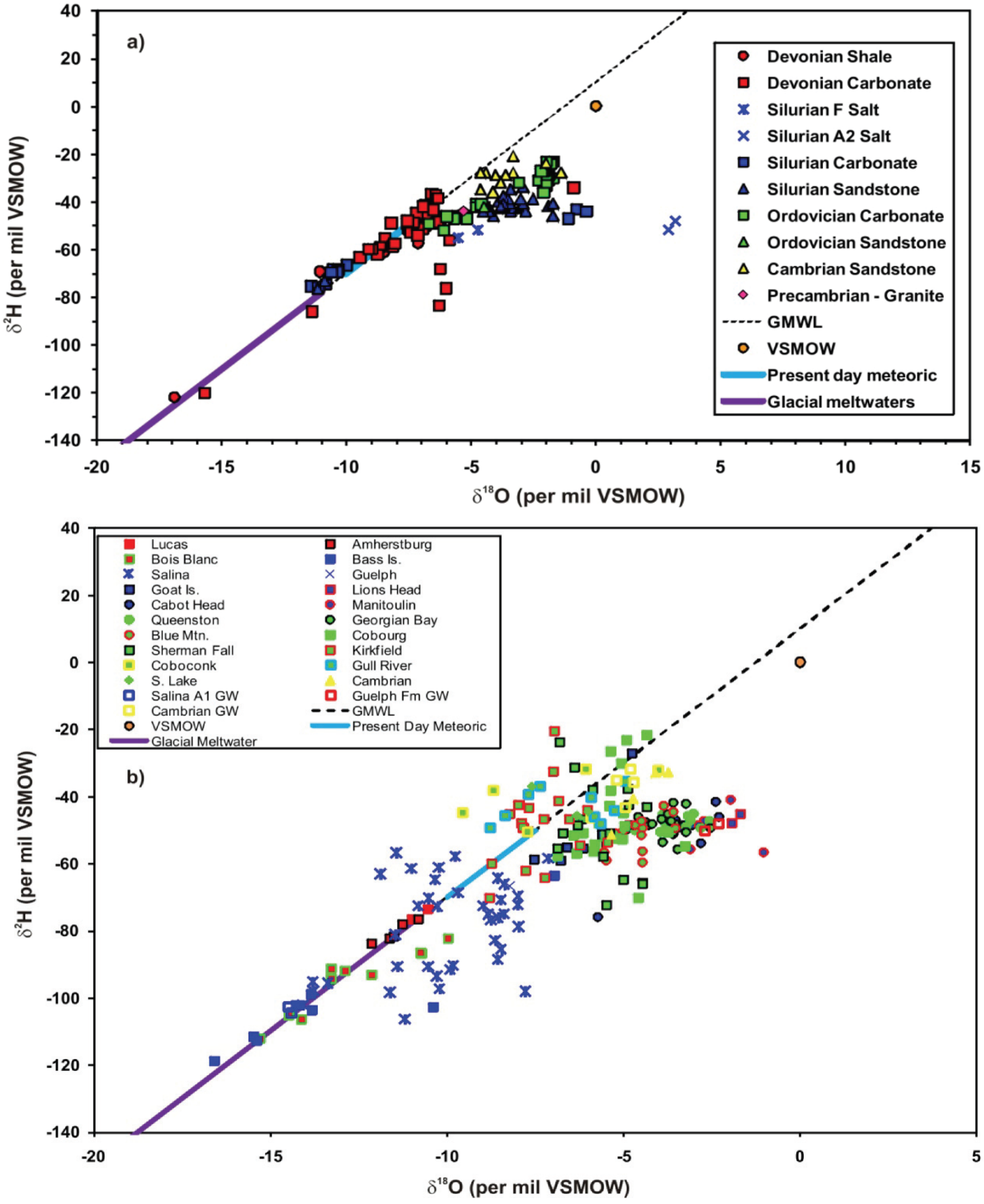

Figure 2.8: Hydrogen versus Oxygen isotopic signatures for porewater and groundwater from a) the UW database and b) collected at the Bruce nuclear site. Developed by Al et al. (2011).

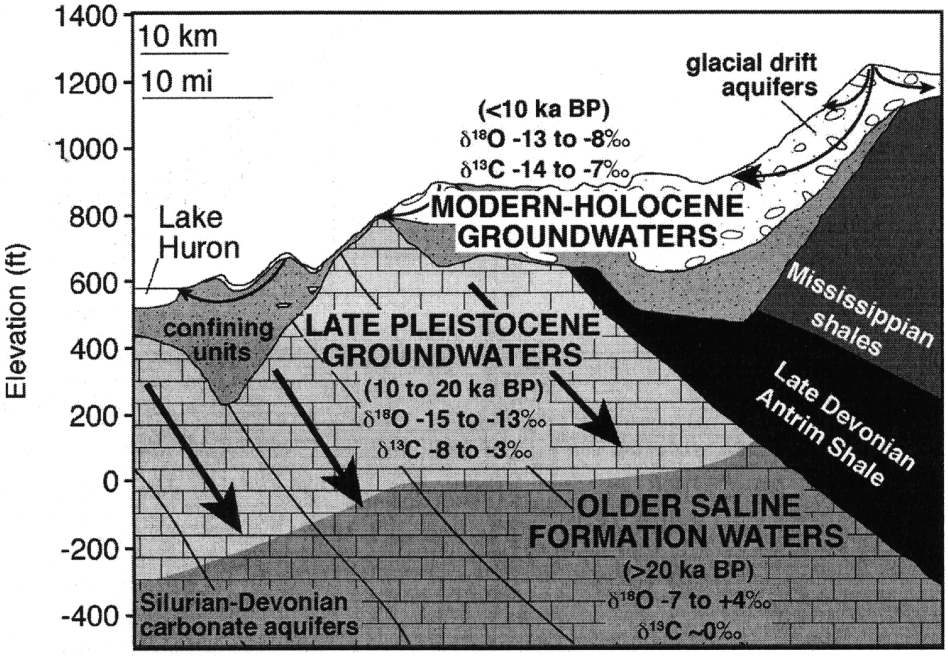

Figure 2.9: Conceptual model showing the dilution of deep ancient brines by glacial melt water penetration during ice sheet advance and the (relatively shallow) infiltration of modern day meteoric waters. Modified from McIntosh and Walter (2006).

clear Site, which are typically at or below the lower limit of the present day precipitation interval in Figure 2.8. Evidence of the significant dilution of the original brines is also apparent in the TDS concentrations for this unit (typically <50 g/L). The infiltration of Pleistocene and younger age waters to the Devonian (and in some cases Upper Silurian) Formations is understandable considering that many of these formations subcrop below shallow, unconsolidated glacial overburden.

2.3 Methane Gas

Methane occurrences are differentiated based upon the nature of their formation: (1) thermogenic decomposition of organics under high temperature and pressure regimes, (2) microbial or biogenic respiration by methanogenic microbes as they break down organic material, and (3) abiogenic methane generation without the presence of organic material, whereby CO_2 in the presence of H_2 is chemically reduced to CH_4, such as in the catalytically driven serpentinization reaction (McCollom and Seewald, 2013). Typically, the composition of the natural gas and the ratio of the δ^{13}C to δ^{2}H isotope compositions are used as indicators to ascribe the appropriate classification (Whiticar, 1999). Thermogenically formed gas results in a low methane (C1) to ethane plus propane (C2 + C3) ratio (<100), and is enriched in δ^{13}C compared to biogenic sources. Conversely, biogenic gas is characterized by relatively depleted δ^{13}C isotope compositions (<60‰), and by a high methane (C1) to ethane plus propane (C2 + C3) ratio (>1000) due to the limited formation of higher hydrocarbons. Abiogenic methane is highly enriched in δ^{13}C relative to the expected biogenic or thermogenic regions (δ^{13}C >-15‰); however, because abiogenic methane is generally limited to the high-temperature (>500°C) hydrothermal systems associated with mid-ocean-ridge environments (Schoell, 1988; Welhan, 1988), it is unlikely to occur in the sedimentary strata of the intracratonic Michigan Basin.

The occurrences of methane at the Bruce nuclear site, based on groundwater and core sampling from the DGR boreholes, are presented in Figure 2.10, along with results of isotopic composition analysis of the extracted gas samples. For ease of discussion, the vertical CH_4 profile can be divided into four distinct regions: (1) a low-occurrence region extending down from the surface to a depth of approximately 300 mBGS in the Silurian A2 unit; (2) a relatively shallow high concentration region in the Guelph Formation and proximal units of the Middle and Lower Silurian packages that extends from approximately 375 to 410 mBGS; (3) an intermediate region characterized by a significant concentration increase corresponding in depth to the Blue Mountain-Collingwood (between 617 and 660 mBGS); and (4) a deep region of intermittent occurrences of elevated concentration that extends down through the carbonate sediments of the Middle Ordovician package (between 700 and 840 mBGS).

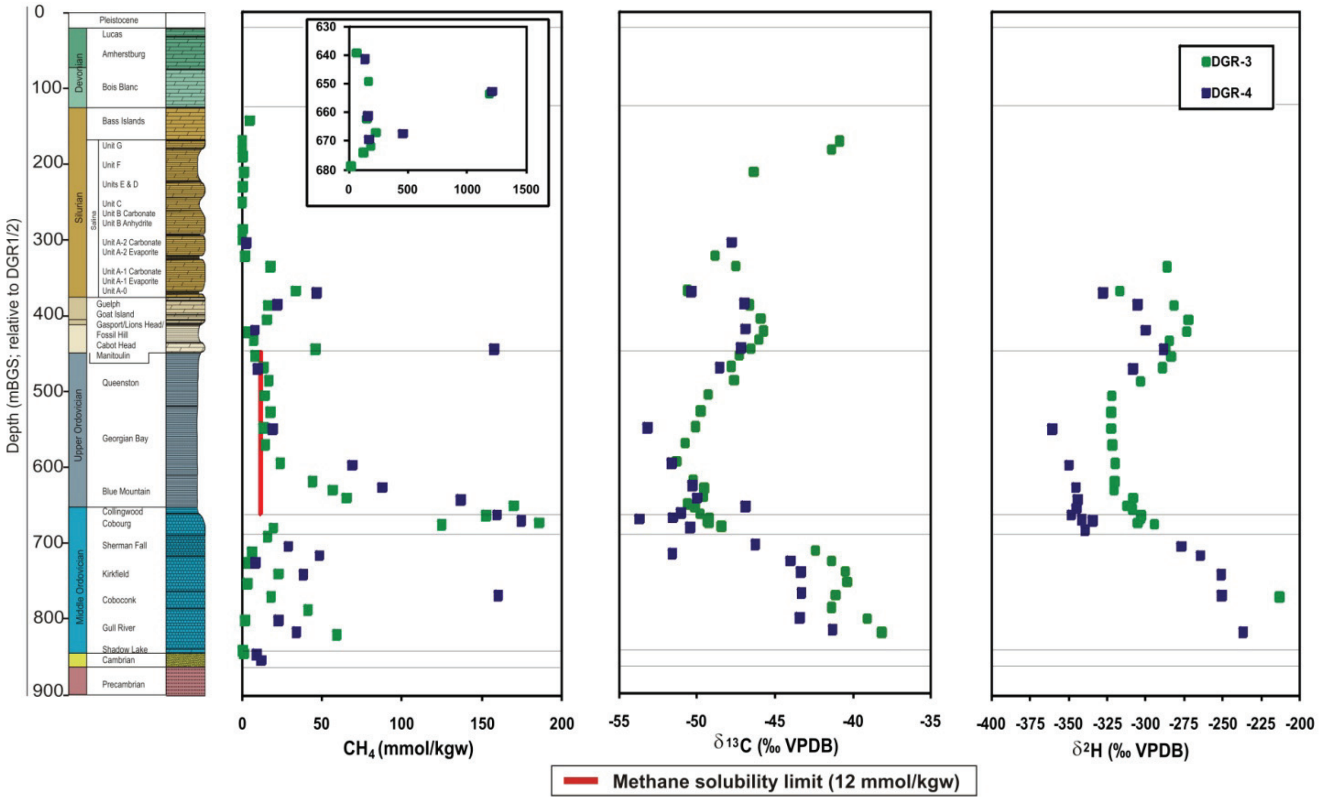

Figure 2.10: Vertical profiles of CH$_4$ (mmol/kgw) and stable isotopes (δ^{13}C and δ^2H) determined in porewater and groundwater (McIntosh and Walter, 2006).

It is worth noting that because the vertical extents of these methane regions within the sedimentary strata are based on the data collection efforts towards the centre of the study area at the Bruce DGR boreholes (INTERA, 2011), their depth of occurrence should not be taken to be laterally constant. Rather, the thinning and sub-/outcropping of the sedimentary strata toward the flank of the Algonquin Arch indicates that, if we adopt a lateral methane occurrence model that favours lithological continuity over specific depth intervals, the aforementioned methane bearing regions of the study area become far more shallow towards the north-east end of the study area. This shift in burial depth would be expected to coincide with a change in subsurface conditions (ie. temperature salinity, and pressure) that could play an important role in the determination of potential methane hydrate forming regions.

Further insight into the methane within the noted regions is provided by comparing the stable isotopic ratios of δ^{13}C and δ^{2}H (Figure 2.11) to determine their biogenic or thermogenic origins (Whiticar, 1999). The relatively δ^{13}C and δ^{2}H enriched nature of the deep intermittent region related to the Middle Ordovician carbonates suggests the methane associated with this formation is of thermogenic origin. Conversely, the isotopic signature of the shallower intermediate region proximal to the Blue Mountain-Collingwood units is depleted in δ^{13}C and δ^{2}H, indicating that this methane is of biogenic origin formed by fermenting bacteria. Though likely younger than the deeper thermogenic methane, the intermediate biogenic methane has been interpreted as being relatively immobile (vertically) based upon the aforementioned high methane saturation within the Ordovician brines, resulting in a lack a of concentration gradient to drive the vertical diffusive transport of methane (Al et al., 2011). This combined with the fact that high salinities (such as those found in these formations) tend to inhibit microbial activity, suggests that the methane within this formation is of a relatively old age, potentially dating back to the Paleozoic. The shallowest region of methane occurrence proximal to the Guelph Formation is also considered to be of biogenic origin based upon the stable isotope signature, although the isotopic signature shows a slight deviation toward the thermogenic region on the discrimination diagram (Figure 2.11). While this could be attributed to mixing of the two methane source types, given that the lower adjacent methane regions of the Ordovician sediments show no sign of this mixing, this scenario is unlikely. A possible explanation for this deviation is the impact of isotope fractionation caused by preferential migration of the lighter isotopes, causing the systematic enrichment of both δ^{13}C and δ^{2}H (Schoell, 1988).

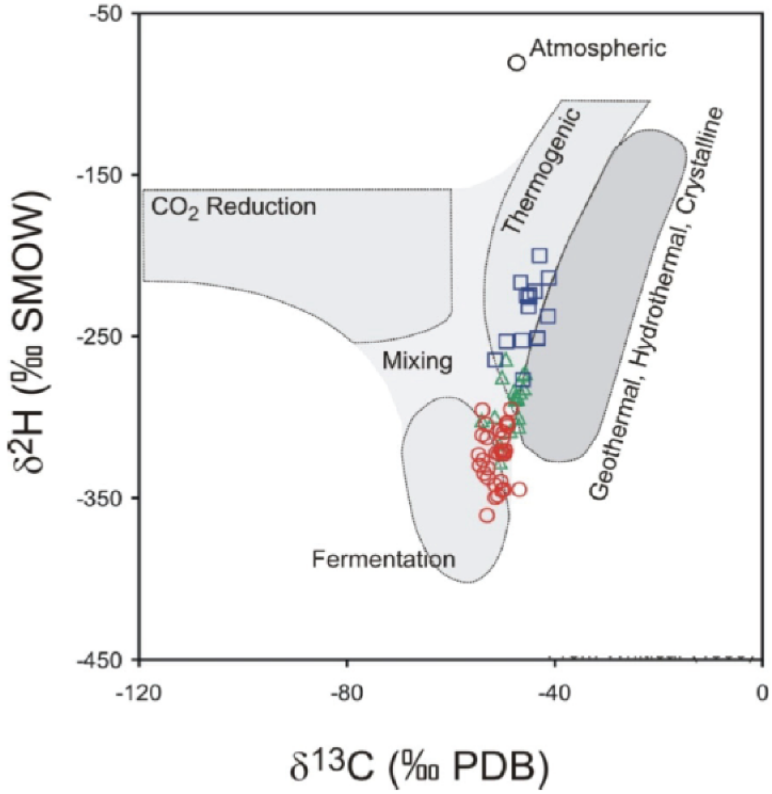

Notes: Source is Whiticar (1999). Green triangles represent data from the Queenston Formation and above, red circles from the Cobourg, Blue Mountain and Georgian Bay formations, and the blue squares from below the Cobourg Formation.

Figure 2.11: Discrimination diagram indicating fields for CH_4 of biogenic (CO_2 reduction and fermentation) and thermogenic origin.

2.4 Geological Occurrence of Gas Hydrates

Methane hydrates are found in vast quantities around the world, deposited in ocean sediments on the continental margins and terrestrial lithologies in permafrost regions. Estimates of the quantity of methane stored in the global hydrate reservoirs are highly varied, although the approximate value of 1×10^{19} g of methane carbon has been proposed by Kvenvolden and Rogers (2005) to represent a ‘consensus estimate’ of the present size of the hydrate-stored methane. Continental margins account for the vast majority of the global methane hydrate reservoir (Table 2.4), with estimates 2 to 4 orders of magnitude larger than the estimated size of methane hydrate reservoirs in Arctic permafrost regions. Based on these estimates, the global gas hydrates are believed to represent more than half of the organic carbon (excluding dispersed organic carbon species such as kerogen and bitumen) in the Earth, and two orders of magnitude larger than the remaining methane reservoirs considered to be conventionally recoverable (Kvenvolden, 1998). The sheer size of these reservoirs necessarily draws the interest of researchers representing both energy sector interests as well as climatologist concerned about both sudden and gradual releases of methane gas into the atmosphere - methane gas being 21 to 23 times more potent as a greenhouse gas than carbon dioxide (Grace et al., 2008). In a more regional-scale geologic context, methane hydrates are known to impact the physical properties of sediments (permeability and porosity)(Winters et al., 2011), as well as the geochemistry of pore fluids, potentially impacting gas extraction and mining activities in northern permafrost regions.

Table 2.4: Estimated Size of Methane Hydrate Reservoir in Ocean Sediments and Arctic Permafrost

Methane Carbon	Reference
Ocean Sediments	
$\sim 2.1 \times 10^{19} g$	Kvenvolden and Claypool (1988)
$\sim 1.0 \times 10^{19} g$	Kvenvolden (1988)
$\sim 1.1 \times 10^{19} g$	MacDonald (1990)
Arctic Permafrost	
$\sim 3.9 \times 10^{17} g$	MacDonald (1990)
$\sim 1.7 \times 10^{16} g$	McIver (1981)
$\sim 7.6 \times 10^{15} g$	Meyer (1981)

Instances of naturally occurring gas hydrates have been identified around the world in both ocean sediments and terrestrial permafrost regions (Figure 2.12), providing researchers with the opportunity to study the properties of gas hydrate reservoirs. Some of the more recent research undertaken on terrestrial hydrates in the Arctic permafrost regions include:

- **Mallik 2002 Gas Hydrate Production Research Well Program**. *Northwest Territories, Canada.* The latest of the Mallik research programs, involving an international collaboration of 5 countries and more than 200 researchers, exploring the sub-permafrost gas hydrate reservoir below the Mackenzie Delta on the coast of the Beaufort Sea. The study involved completion of three deep research wells (approximately 1000 mBGS), with detailed coring geophysical analysis of the hydrate bearing strata below the permafrost. (Dallimore et al., 2005)

- **Mount Elbert Gas Hydrate Stratigraphic Test Well**. *Alaska North Slope,* *United States.* A project conducted since 2001 as a collaborative effort by the US Department of Energy (DOE), the US Geological Survey (USGS), and BP Exploration (Alaska) Inc. to determine the viability of the Alaska North Slope gas hydrates as a gas resource. The project produces a full suite of geophysical wireline logs, core, and formation pressure data along with various modelling studies that improved estimates of gas hydrate bearing reservoir properties. (Hunter et al., 2011)

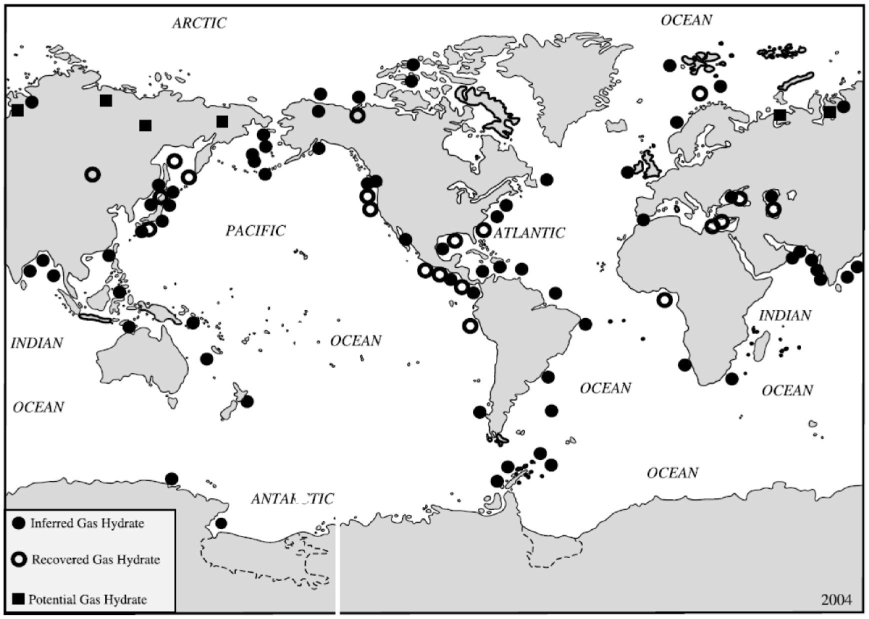

Figure 2.12: Map of known and inferred locations of Gas Hydrates in Ocean Sediments and Arctic Permafrost Regions around the world (Kvenvolden and Rogers, 2005).

Since gas hydrates become unstable when exposed to temperature and pressure conditions at ground surface, both the Mallik and Mount Elbert gas hydrate research programs dedicated considerable attention to the implementation of advanced down-hole geophysical logging techniques to identify and quantify gas hydrates within the subsurface (Collett et al., 2005, 2011). Through comparison of interpreted results with recovered/preserved cores containing hydrates, it was found that these methods could effectively be used to identify existing hydrate accumulations in the subsurface. While such detailed studies have contributed incredibly to the present understanding of the properties of gas hydrates forming in the subsurface of permafrost regions, the use of down-hole geophysical methods showcased in these works are of limited use to the determination of the temporal extent of evanescent gas hydrate accumulations such as those being considered in this study, and face the same limitations in determining spatial hydrate distributions on a regional scale as any subsurface investigation due to the need to make inferences regarding the properties of a study area many orders of magnitude larger than the observation points. Thus, when attempting to identify where gas hydrates have formed in the past, there is a need to consider the lasting impacts left by dissociated subsurface gas hydrates on the physical and geochemical properties of the host lithologies; a topic that has been investigated by a number of gas hydrate researchers (including scientists of the Mallik and Mount Elbert research programs).

The formation and dissociation of gas hydrates is known to influence the geochemistry of groundwater systems – predominantly through the process of solute exclusion and preferential isotope inclusion/exclusion – lending itself to applications in determining the interval of gas hydrate bearing sediments as well as to providing quantitative estimates as to the degree of gas hydrate saturation of the pore volume (Matsumoto and Borowski, 2000; Matsumoto, 2006). Furthermore, if a hydraulic system is sufficiently closed with respect to solute gradient-reducing mechanisms of advective flushing and dispersion, the geochemical signatures left by the presence of gas hydrates may be preserved (or partially preserved) for a period after the dissociation of the gas hydrates. Logically, the residual of these signatures will depend upon the elapsed time since hydrate dissociation and the magnitude of the solute gradient-reducing mechanisms, as well as other rock-water interactions related to diagenetic processes.

The direct influences of gas hydrate formation on groundwater geochemistry are described below (incidental impacts such the limiting of reactant mixing or solute transport caused by changes to the groundwater flow system have been omitted as these are generally site specific):

- *Solute exclusion.* During hydrate formation, solutes within the interstitial water are excluded from the hydrate structure. The result is the apparent freshening of hydrate-associated pore waters and an increase in solute concentrations in hydrate-free pore waters (Ethier et al., 2005). The Chloride (Solute) Anomaly Technique has been used to estimate the degree of gas hydrate saturation (pore filling) using the deviation below an estimated baseline concentration gradient caused by gas hydrate induced freshening (Paull et al., 1996; Matsumoto, 2006).

- *Preferential isotope incorporation in host molecules.* Gas hydrate formation will preferentially incorporate water (host) molecules that are enriched in ^{18}O isotopes compared to the ambient water (Hesse and Harrison, 1981), resulting in a spike in the δ^{18}O ratio where hydrates have formed. The δ^{18}O Anomaly Technique has also been used to estimate the degree of gas hydrate saturation, again by comparing baseline estimates of $\delta^{18}O$ to the regions of ^{18}O enrichment (corresponding to gas hydrate formation) (Matsumoto and Borowski, 2000).

- *Preferential isotope incorporation in guest molecules.* There is evidence to suggest from laboratory studies, that methane and ethane hydrate formation will preferentially exclude guest molecules containing the ^{2}H isotope (Hachikubo et al., 2007); however, this geochemical signature does not represent a significant alteration of gas isotope composition (less than 10‰), and could be explained by a number of other geochemical processes, including the process by which the methane was formed in the first place (Stotler et al., 2010).
- *Gas accumulations and preferential species inclusion.* The formation of gas hydrates represents in an apparent increase in the entrapped hydrocarbon gas concentration as the hydrate structure is able to contain the gas more densely than in the surrounding solution. This results in the local accumulation of the guest gas molecule (Sloan, 2003). Since the structure I hydrates most commonly found in nature accommodate only small diameter molecules such as methane (C_1) and ethane gas (Kvenvolden, 1998), the concentration of other hydrocarbon gas species (C_2-C_5) are preferentially excluded producing an increased carbon wetness ratio (C_1/C_2-C_5) in hydrate-bearing intervals (Lorenson et al., 2005).

The geochemical signatures related to solute exclusion and the preferential incorporation of isotopically heavy water into the lattice structure have been applied to methods of identifying and quantifying methane hydrate occurrences by a number of researchers (Matsumoto and Borowski, 2000; Matsumoto et al., 2005; Tomaru et al., 2005; Winters et al., 2006; Torres et al., 2011). Although the gas hydrates themselves are not present in the cored samples – having dissociated during sample recovery – these geochemical signatures are generally well preserved. In most cases, the qualitative results of comparing the anomalous solute and isotope distributions with the background values to determine the gas hydrate region are in agreement. Comparisons between the results of gas hydrate saturation estimates using various anomalous solute and ^{18}O isotope distributions at a given site are also fairly consistent, the variability being attributed to the uncertainty of estimating an appropriate baseline distribution (Matsumoto and Borowski, 2000). Considering that the scope of this study is to delineate the potential methane hydrate stability region (and not to provide an estimate as to the quantity of methane hydrates), the geochemical signatures could be used to evaluate the predictions provided by the regional-scale model under the assumption that the systems are hydraulically closed to a sufficient degree so as to allow for the preservation of the gas hydrate-imposed geochemical signatures.

Residual gas signatures are less likely to be preserved in cases where gas hydrate dissociation has been complete for a long period of time since the gas hydrate itself is one of the primary inhibitors of gas migration and mixing (Lorenson et al., 2005). This means regions of ^{2}H depleted methane molecules and high carbon wetness caused by gas hydrate formation are therefore of little use for estimating regions subject to gas hydrate dissociation beyond those application where hydrates are presently existing and have dissociated upon sample recovery.

Chapter 3

Methodology

The approach used by this study to evaluate the evolution of methane hydrate stability zones during the advance of glaciers across the study site in Southern Ontario involves the use of regional-scale numerical models to generate temporal temperature, pressure and salinity values. These are subsequently used as input values for thermodynamic predictive modelling to evaluate hydrate stability. An overview of the methodology is presented below:

1. Calculation of pressure, temperature and salinity distributions across the study site for the entirety of the study period:
    (a) The regional-scale model developed by Sykes et al. (2011) was used to estimate the pressure and TDS history for the study site during the 120 ka study period. This model accounts for increases in hydromechanical loading during periods of glacial cover.
    (b) A modified version of the regional-scale model was used to provide the temperature history across the study site, independent of pressure and TDS parameters. The model domain (including node assignments and location) was identical to the regional-model employed for the TDS/pressure history estimations to ensure referencing consistency in the subsequent steps.
2. Aggregation of output datasets from the regional-scale modelling work to allow for visualization and determination of methane solubility and hydrate stability by thermodynamic models.
3. Input of pressure, temperature and TDS histories determined from regional-scale modelling work to thermodynamic models:

   (a) The solubility of methane was determined using the thermodynamic model developed using the theory by Duan and Mao (2006) at each point in the spatial domain of the study site for each of the time steps during the 120 ka study period.
   (b) The stability of methane hydrate was determined using the thermodynamic model developed using the theory by Sun and Duan (2007) for each of the time steps during the 120 ka study period. This was achieved by determining a minimum required pressure based on temperature and salinity that must be exceeded by the "observed" pressure at a given point in order for hydrates to form.

4. Output of thermodynamic models were re-incorporated into the aggregated data set from the regional-scale numerical modelling work to allow for visualization and interpretation.

This Chapter provides a description of the three-dimensional regional-scale numerical model domain and the governing equations employed to determine the transient pressure, temperature and salinity profiles during the study period. The thermodynamic models used for the estimation of methane solubility and hydrate stability are also presented in this Chapter, along with supporting validation work performed used laboratory measurements of solubility and hydrate stability.

3.1 Regional-Scale Numerical Model

The pressure, salinity, and temperature histories used in this study were modelled using the base-case regional-scale model domain developed by Sykes et al. (2011). The modelling domain (Figure 3.1) occupies an aerial extent of approximately 18,775 km^2, and has a vertical elevation range that extends upward from a flat bottom elevation of -1600 mAMSL in the Precambrian basement to 539 mAMSL at the highest point on the Niagara Escarpment. The domain is discretized into slices, each with 27,728 nodes, which were then *stacked* vertically to generate the 32 formation interfaces of the 3D model domain (Table 3.1). In some cases, formation layers have undergone further vertical discretization by breaking them into sublayers with the same geologic/hydrogeologic parameters - for example, the Precambrian layer below the Upper Precambrian has been subdivided into six sublayers, with a seventh serving as the flat base of the model domain.

A detailed description of the methodology by which the model domain was constructed can be found in Sykes et al. (2011). The groundwater flow parameters for the formation

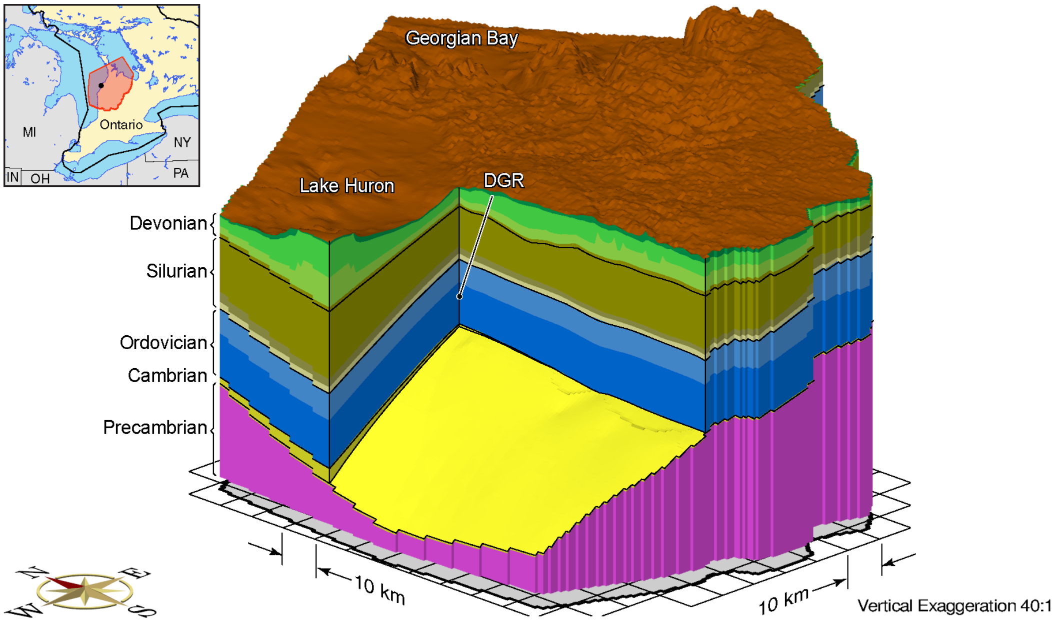

Figure 3.1: Regional model domain of the numerical model.

layers are summarized in Table A.1 in Appendix A. Also included are the one-dimensional loading efficiency ζ values assigned to each of the formations. The solute transport parameters of density ρ, total dissolved solids TDS, and the effective diffusion coefficient D_e for dissolved solids transport are provided in Table A.2. The governing equations for groundwater flow, one-dimensional hydromechanical coupling, solute transport, and constitutive relationships for density and concentration as they are implemented in FRAC3DVS-OPG are provided in the following sections, based on the descriptions provided by Normani (2010). The handling of transient temperature in FRAC3DVS-OPG for this study is also described in this chapter.

In the regional-model, it is assumed that there is no free-gas phase present in the subsurface; since the presence of a gas phase would result in the dissipation of some of the pressure of glacial loading, this assumption could result in the over-estimation of the pore pressures used in the study. While the likelihood of a free-gas phase being somewhere within the domain is high, it is *not* necessarily a requirement for achieving saturation of methane and subsequent formation of gas hydrates (Handa, 1990). This would be the case where a pore water, with dissolved methane concentrations below saturation, undergoes a decrease in temperature such that the conditions shift to those of a hydrate formational zone while simultaneously lowering the local solubility sufficiently to shift the dissolved methane concentration beyond saturation. In this case, the decrease in temperature would

Table 3.1: Geologic formations represented in the regional-scale model domain (Sykes et al., 2011)

Period	**Model Formation**	**Formation**
Quaternary	Drift	Drift
Devonian	Hamilton Group	Hamilton Group
	Dundee	Dundee
	Detroit River Group	Lucas Amherstburg (upper 20 m) Amherstburg (lower 25 m)
	Bois Blanc	Bois Blanc
Silurian	Bass Islands	Bass Islands(upper 20 m) Bass Islands(lower 25 m)
	Unit G	Salina Unit G
	Unit F	Salina Unit F
	Unit F Salt	Salina Unit F
	Unit E	Salina Unit E
	Unit D	Salina Unit D
	Units B and C	Salina Unit C Salina Unit B
	Unit B Anhydrite	Salina Unit B Evaporite
	Unit A2 Carbonate	Salina Unit A2 Carbonate
	Unit A2 Evaporite	Salina Unit A2 Evaporite
	Unit A1 Carbonate	Salina Unit A1 Upper Carbonate Salina Unit A1 Carbonate
	Unit A1 Evaporite	Salina Unit A1 Evaporite Salina Unit A0
	Niagaran Group	Guelph Goat Island Gasport Lions Head
	Reynales / Fossil Hill	Fossil Hill
	Cabot Head	Cabot Head
	Manitoulin	Manitoulin
Ordovician	Queenston	Queenston
	Georgian Bay / Blue Mtn.	Georgian Bay Blue Mountain Collingwood
	Cobourg	Cobourg
	Sherman Fall	Sherman Fall
	Kirkfield	Kirkfield
	Coboconk	Coboconk
	Gull River	Gull River
	Shadow Lake	Shadow Lake
Cambrian	Cambrian	Cambrian
Precambrian	Upper Precambrian	Upper Precambrian
	Precambrian	Precambrian

result in the formation of gas hydrates without the presence of a free-phase gas phase of methane since the methane would move directly from being in solution to the hydrate lattice.

In the regional-scale model, salinity is modelled using a generalized TDS solute in order to simplify the model and avoid the complexity of representing multiple ion species. The species that make up the salt were assumed to be dominated by NaCl in all cases, rather than applying the location/formation specific electrolyte compositions determined from bedrock borehole sampling. The composition of the salt impacts both the gas solubility and the hydrate formation pressure threshold, which makes it an important consideration in identifying the formational zones for gas hydrates. Compared to systems dominated by NaCl (holding total salt concentrations the same), $CaCl_2$ dominated systems have higher methane solubility values and higher hydrate formation pressure thresholds (Kharrat and Dalmazzone, 2003). As a result, using a universal assumption that the TDS from the regional-model is composed entirely of NaCl underestimates the prohibitive impact of salinity on hydrate formation, and contributes to an overall conservative assumption for this study that favours the formation of methane hydrates.

3.1.1 Fluid Flow

The following equation is used to describe mass conservation for flow in a saturated porous medium is defined as (Bear, 1988):

$$-\frac{\partial}{\partial x_i}(\rho q_i) \pm Q = \frac{\partial}{\partial t}(\eta \rho) \tag{3.1}$$

where ρ is the density $[g/cm^3]$, q_i is the Darcy flux vector in direction i $[cm/yr]$, Q is the fluid source/sink term $[g/yr \cdot cm^3]$, t is the time $[yr]$, and η is the total porosity [/]. The Darcy equation relating flux to the energy potential of the fluid is defined as (Bear, 1988; Frind, 1982):

$$q_i = -K_{ij}\left(\frac{\partial h}{\partial x_j} + \rho_r \frac{\partial z}{\partial x_j}\right) \qquad h = \frac{p}{\rho_0 g} + z \qquad i,j = 1,2,3 \tag{3.2}$$

where K_{ij} is the hydraulic conductivity tensor $[cm/yr]$, h is the freshwater head $[cm]$, ρ_r is the relative fluid density [/], p is the fluid pressure $[g/cm \cdot yr^2]$, ρ_0 is the reference fluid density $[g/cm^3]$, g is the gravitational constant $[cm/yr^2]$, and z is the fluid elevation $[cm]$. In Equation 3.2, the relative density ρ_r is defined as:

$$\rho_r = \frac{\rho}{\rho_0} - 1 \tag{3.3}$$

The hydraulic conductivity tensor in Equation 3.2 is defined as:

$$K_{ij} = \frac{k_{ij}\rho g}{\mu} \qquad i,j = 1,2,3 \tag{3.4}$$

where k_{ij} is the porous media permeability tensor $[cm^2]$, and μ is the dynamic viscosity $[g \cdot yr/cm]$. In combining Equation 3.1 and Equation 3.2, the groundwater flow equation can be simplified to (Frind, 1982):

$$\frac{\partial}{\partial x_i}\left[K_{ij}\left(\frac{\partial h}{\partial x_j} + \rho_r \frac{\partial z}{\partial x_j}\right)\right] \pm Q = S_s \frac{\partial h}{\partial t} \qquad i,j = 1,2,3 \tag{3.5}$$

where S_s is the specific storage coefficient $[cm^{-1}]$. The storage coefficient is a measure of the compressibility of the porous media and pore fluid and is defined as the volume of water that a unit volume of aquifer releases from storage under a unit decline of piezometric head (Freeze and Cherry, 1979).

3.1.2 Hydromechanical Coupling

Assuming that the porous media, solid grains, and pore fluid are all compressible, the storage coefficient, S_s, can be re-defined to include one-dimensional vertical loading and unloading. This simplified one-dimensional approach to hydromechanical coupling is commonly used to simulate the impacts of glacial, erosional and depositional mechanisms on groundwater systems (Van der Kamp and Gale, 1983; Neuzil, 2003; Jaeger et al., 2007). The modified expression for S_s is provided below:

$$S_s = \rho g \left[\left(\frac{1}{K} - \frac{1}{K_s}\right)(1-\lambda) + \eta\left(\frac{1}{K_f} - \frac{1}{K_s}\right)\right] \qquad \lambda = \frac{2\alpha(1-2\nu)}{3(1-\nu)} \qquad \alpha = 1 - \frac{K}{K_s} \tag{3.6}$$

where K is the drained bulk modulus of the porous media $[g/cm \cdot yr^2]$, K_s is the bulk modulus of the solids in the porous media $[g/cm \cdot yr^2]$, K_f is the bulk modulus of the pore fluid $[g/cm \cdot yr^2]$, α is the Biot coefficient [/], and ν is the Poisson's ratio [/]. The bulk modulus K is defined as the reciprocal of compressibility (β), therefore $K = 1/\beta$ (Jaeger et al., 2007).

Mechanically loading the surface of a porous media results in the loading of both the porous media and the pore fluid. The amount of stress transferred to each of the components is dependent upon the relative compressibility of the porous media to the pore fluid, as well as the porosity. Due to the somewhat elastic nature of porous media, when a surface load is applied, the porous media will tend to compress. This results in a reduction in the pore size, which in turn compresses the pore fluid. As the pore fluid undergoes compression, the result is increased resistance to the compression of the porous media, and increased pore pressure. Mechanical loading of a porous media and pore pressure within said media are therefore a coupled system. The groundwater flow equation (Equation 3.5) can be modified to account for one-dimensional hydromechanical coupling as follows (Neuzil, 2003):

$$\frac{\partial}{\partial x_j}\left[K_{ij}\left(\frac{\partial h}{\partial x_j}+\rho_r\frac{\partial z}{\partial x_j}\right)\right]\pm Q=S_s\frac{\partial h}{\partial t}-\frac{S_s\zeta}{\rho g}\frac{\partial \sigma_{zz}}{\partial t}\qquad i,j=1,2,3 \tag{3.7}$$

where ζ is the one-dimensional loading efficiency [/], and σ_{zz} is the vertical stress $[g/cm \cdot yr^2]$. It should be noted that no lateral strains are considered in this approach, as a fundamental assumption of one-dimensional hydromechanical coupling is that strains can only occur in a vertical direction. The loading efficiency is further defined as (Van der Kamp and Gale, 1983; Neuzil, 2003):

$$\zeta=\frac{B(1+\nu)}{3(1-\nu)-2\alpha B(1-2\nu)}\qquad B=\frac{\left(\frac{1}{K}-\frac{1}{K_s}\right)}{\left(\frac{1}{K}-\frac{1}{K_s}\right)+\eta\left(\frac{1}{K_f}-\frac{1}{K_s}\right)} \tag{3.8}$$

where B is the Skempton coefficient used to represent the ratio of the change in fluid pressure to a change in mean effective stress under undrained conditions (Neuzil, 2003). A further simplifying assumption is commonly made whereby the solids of the porous media are taken to be incompressible (or rigid), such that $K_s \to \infty$, resulting in:

$$S_s=\rho g\left(\frac{1}{K'}+\eta\frac{1}{K_f}\right)\qquad \zeta=\frac{\frac{1}{K'}}{\frac{1}{K'}+\eta\frac{1}{K_f}} \tag{3.9}$$

where K' is the drained confined vertical modulus of the porous media $[g/cm \cdot yr^2]$. K' can be calculated from properties such as Young's elastic modulus, E, and Poisson's ratio, ν (Neuzil, 2003; Jaeger et al., 2007):

$$K=\frac{E}{3(1-2\nu)}\qquad K'=K\frac{3(1-\nu)}{1+\nu} \tag{3.10}$$

Since the geometric deformation of the model grid is not permitted in FRAC3DVS-OPG, the hydromechanical term $\frac{S_s\zeta}{\rho g}\frac{\partial\sigma_{zz}}{\partial t}$ in Equation 3.7 serves as a fluid source/sink term to effectively increase or decrease the fluid pore pressure - and therefore head h - based on the rate of change of the vertical stress, $\frac{\partial\sigma_{zz}}{\partial t}$, the storage coefficient, S_s, and the one-dimensional loading efficiency, ζ (Normani, 2010). A loading efficiency that approaches zero is representative of a more rigid porous media and/or a highly compressible pore fluid, such that a minimal amount of the load is transferred to the pore fluid. Conversely, a loading efficiency that approaches one is indicative of a more compressible porous media compared to the pore fluid pore fluid, whereby the bulk of the load is supported by the pore fluid instead of the porous media. Both the storage coefficient, S_s, and the one-dimensional loading efficiency, ζ, are specified inputs to FRAC3DVS-OPG.

3.1.3 Solute Transport

The generalized solute transport equation for a saturated porous media is (Bear, 1988):

$$\frac{\partial}{\partial x_i}\left(\eta D_{ij}\frac{\partial C}{\partial x_j}\right) - \frac{\partial}{\partial x_i}(q_i C) \pm \Omega_C = \frac{\partial}{\partial t}(\eta C) \qquad i,j = 1,2,3 \tag{3.11}$$

where D_{ij} is the hydrodynamic dispersion tensor $[cm^2/yr]$, C is the concentration $[g/cm^3]$, and Ω_C is the concentration source/sink term $[g/yr \cdot cm^3]$. D_{ij} is defined by Burnett and Frind (1987) as:

$$\eta D_{11} = \alpha_L \frac{q_1^2}{|q|} + \alpha_{TH}\frac{q_2^2}{|q|} + \alpha_{TV}\frac{q_3^2}{|q|} + \eta\tau D_m \tag{3.12a}$$

$$\eta D_{22} = \alpha_{TH} \frac{q_1^2}{|q|} + \alpha_{L}\frac{q_2^2}{|q|} + \alpha_{TV}\frac{q_3^2}{|q|} + \eta\tau D_m \tag{3.12b}$$

$$\eta D_{33} = \alpha_{TV} \frac{q_1^2}{|q|} + \alpha_{TV}\frac{q_2^2}{|q|} + \alpha_{L}\frac{q_3^2}{|q|} + \eta\tau D_m \tag{3.12c}$$

$$\eta D_{21} = \eta D_{12} = (\alpha_L - \alpha_{TH})\frac{q_1 q_2}{|q|} \tag{3.12d}$$

$$\eta D_{31} = \eta D_{13} = (\alpha_L - \alpha_{TV})\frac{q_1 q_3}{|q|} \tag{3.12e}$$

where α_L is the longitudinal dispersivity $[cm]$; α_{TH} is the horizontal transverse dispersivity $[cm]$, α_{TV} is the vertical transverse dispersivity $[cm]$, $|q|$ is the magnitude of the Darcy flux $[cm/yr]$, τ is the tortuosity of the porous medium $[/]$, and D_m is the molecular diffusion coefficient $[cm^2/yr]$.

In literature, the pore water diffusion coefficient is also referred to as the diffusion coefficient of the porous medium (Bear, 1988). The relationship between fluid density in Equation 3.7 and pore fluid concentration is as follows:

$$\rho_r = \gamma \frac{C}{C_{max}} \qquad \gamma = \frac{\rho_{max}}{\rho_0} - 1 \tag{3.13}$$

where C_{max} is the maximum concentration $[g/cm^3]$, ρ_{max} is the maximum density $[g/cm^3]$, and γ is the maximum relative density $[/]$. Such a relationship is commonly used to model concentrated brines with concentrations of 300 g/L or higher, as described in the following section.

3.1.4 Constitutive Relationships

Constitutive or functional relationships are used to link fluid or porous media properties to the pressure, temperature or concentration of a system. Various state equations similar to those used in FRAC3DVS-OPG are presented by Bear (1988) and Adams and Bachu (2002) along with empirically determined coefficients.

In the groundwater systems of deep geosphere environments, the impact of these constitutive relationships can be very significant, with density and viscosity variations that can exceed 25% and one order-of-magnitude, respectively. These changes in density and viscosity can contribute to either the retardation or enhancement of fluid flow or contaminant transport. The following expressions describe the relationships between concentration (expressed as Total Dissolved Solids or TDS), solution density, and mass fraction in characterizing solutes in water:

$$\rho = \frac{M}{V} \tag{3.14a}$$

$$TDS = \frac{m}{V} \tag{3.14b}$$

$$X = \frac{m}{M} \tag{3.14c}$$

where TDS is the total dissolved solids $[g/cm^3]$, M is the mass of solution $[g]$, V is the volume of solution $[cm^3]$, m is the mass of solute (e.g., NaCl or $CaCl_2$) $[g]$, and X is the mass fraction [/]. The combination of these expressions, provides an alternative relationship for TDS:

$$TDS = m\frac{1}{V} = XM\frac{\rho}{M} = X\rho \tag{3.15}$$

Adams and Bachu (2002) present an empirical relationship between density and brine conecentration based on the analysis of 4,854 samples within the Alberta Basin. Based on the data and analyses presented in this work, a mass fraction of 0.25 corresponds to a density of approximately 1,200 kg/m^3 and a TDS of 300 g/L.

3.1.5 Thermal History

The transient temperature profiles for the study locations were calculated using a numerical solution to the three-dimensional heat equation:

$$\frac{\partial^2 T}{\partial x_i^2} - c_p\rho\frac{\partial T}{\partial t} = -\frac{A}{k} \qquad i = 1, 2, 3 \tag{3.16}$$

where T is the temperature [°C], x_i are components of cartesian coordinates in the i^{th} direction $[m]$, c_p is the bulk specific heat capacity $[J/kg/K]$, A is the heat production $[mW/m^3]$, ρ is density $[g/cm^3]$, k is the thermal conductivity $[W/mK]$, and t is time $[yr]$. It should be noted that Equation 3.16 does not include a term for the convective transport of heat within the regional domain; however, convective transport during glaciation would likely result in lower temperatures than calculated in this study due to the possible penetration of cold glacial melt waters (McIntosh et al., 2010). It should be noted that density effects and the presence of methane hydrates in the pore space would tend to restrict the penetration of subglacial melt waters, lessening the impact of this assumption on the overall conservative (favouring hydrate formation) estimates provided by this study.

The study site's thermal history was modelled using FRAC3DVS-OPG by manipulating the input files of the regional-scale such that the three-dimensional heat equation is solved in place of the transient subsurface flow equation. This approach allowed for the assignment of lithology-dependent geothermal parameters to the various model layers to better represent the heterogeneous composition of the regional domain. Formation specific parameters were identified from a number of sources (Everham and Huntoon, 1999; Waples and Waples, 2004; McIntosh et al., 2010), and assigned to the individual nodes based upon their stratigraphic location. The geothermal properties assigned to the various formations are provided in Appendix A Table A.3.

Across the base of the regional model, a constant heat flux boundary condition of 45 W/m^2 was applied, which is consistent with observed heat flow values at the base of the Michigan Basin (McIntosh et al., 2010). A transient Dirichlet boundary condition was applied at the top of the model, using the sub-glacial base temperatures calculated by Peltier (2011) throughout the Pleistocene ice-sheet history. An initial temperature gradient was established throughout the regional domain by running the model with the fixed thermal heat flux at the base and a fixed boundary condition at the top of the domain equal to the initial sub-glacial temperature provided by Peltier (2011) until apparent steady-state conditions are achieved. It should be noted that this study does not consider the latent heat impacts of the permafrost zone following glacial episodes, which is considered to act as a buffer that preserves the hydrate stability conditions, reducing the rate of dissociation (Taylor et al., 2005).

3.2 Methane Solubility Calculation

In addition to meeting the required pressure and temperature conditions, there must be sufficient methane in the system to allow the formation of hydrates; the solubility of methane defines the minimum methane concentration required for hydrate formation (Sun and Duan, 2007). Although this study does provide the lower limits of the methane required for the generation of gas hydrates, it does not evaluate whether the amount of methane present at the investigation points reaches or exceeds these limits.

The solubility of methane with respect to pressure [P] and temperature [T], is determined using the method proposed by Duan and Mao (2006), which depends upon balancing the energy potentials of the methane gas in vapour, $\mu^{v}_{CH_4}$, and liquid, $\mu^{l}_{CH_4}$, phases, expressed by Equations 3.17 and 3.18, respectively.

$$\mu^{v}_{CH_4} = \mu^{v(0)}_{CH_4} + RT\ln y_{CH_4}P + RT\ln\varphi_{CH_4} \tag{3.17}$$

$$\mu^{l}_{CH_4} = \mu^{l(0)}_{CH_4} + RT\ln m_{CH_4} + RT\ln\gamma_{CH_4} \tag{3.18}$$

where $\mu^{l(0)}_{CH_4}$ is the standard chemical potential of methane gas in an idealized solution, and $\mu^{v(0)}_{CH_4}$ is the standard chemical potential in the vapour. R is the Universal gas constant equal to 83.145 $bar \cdot cm^3 \cdot mol^{-1}K^{-1}$. In this case, the values of $\mu^{v(0)}_{CH_4}$ is taken to be 0 such that the difference between the liquid and vapour potential energies is accounted for in the parametrization of $\mu^{l(0)}_{CH_4}$ (Duan and Mao, 2006). $\ln\varphi_{CH_4}$ is the fugocity coefficient of the methane gas, y_{CH_4} is the mole fraction of methane gas, and $\ln\gamma_{CH_4}$ is the activity coefficient of the aqueous solution, which accounts for the reduction in solubility due to the presence of electrolytes. Combining Equations 3.17 and 3.18 gives the following equation, which is solved to find m_{CH_4}, the solubility of methane gas in the aqueous solution expressed in terms of molality $[mol/kg]$:

$$\ln\frac{y_{CH_4}P}{m_{CH_4}} = \frac{\mu_{CH_4}^{l(0)}}{RT} - \ln\varphi_{CH_4} + \ln\gamma_{CH_4} \tag{3.19}$$

The fugacity coefficient, $\ln\varphi_j$, is calculated using the Equation of State (EOS) proposed by Duan et al. (1992), which is empirically derived for a large range of temperatures and pressures. The EOS of Duan et al. (1992) is performed by solving Equation 3.20 for the molar volume, V_r $[dm^3/mol]$. This value is then used to calculate the fugacity coefficient value using Equations 3.21-3.22. The EOS parameters used to calculate CH_4 are provided in Table 3.2. It should be noted that the calculation of V_r requires the use of a non-linear equation solver, which results in a computational strain on the model.

$$Z = \frac{PV}{RT} = \frac{P_rV_r}{T_r} = 1 + \frac{B}{V_r} + \frac{C}{V_r^2} + \frac{D}{V_r^4} + \frac{E}{V_r^5} + \frac{F}{V_r^2}\left(\beta + \frac{\gamma}{V_r^2}\right)\exp\left(-\frac{\gamma}{V_r^2}\right) \tag{3.20a}$$

$$B = a_1 + \frac{a_2}{T_r^2} + \frac{a_3}{T_r^3} \tag{3.20b}$$

$$C = a_4 + \frac{a_5}{T_r^2} + \frac{a_6}{T_r^3} \tag{3.20c}$$

$$D = a_7 + \frac{a_8}{T_r^2} + \frac{a_9}{T_r^3} \tag{3.20d}$$

$$E = a_{10} + \frac{a_{11}}{T_r^2} + \frac{a_{12}}{T_r^3} \tag{3.20e}$$

$$F = \frac{\alpha}{T_r^3} \tag{3.20f}$$

$$P_r = \frac{P}{P_c} \tag{3.20g}$$

$$T_r = \frac{T}{T_c} \tag{3.20h}$$

$$V_r = \frac{V}{V_c} \tag{3.20i}$$

$$V_c = \frac{RT_c}{P_c} \tag{3.20j}$$

$$G = \frac{F}{2\gamma}\left[\beta + 1 - \left(\beta + 1 + \frac{\gamma}{V_r^2}\right)\exp\left(-\frac{\gamma}{V_r^2}\right)\right] \tag{3.21}$$

$$\varphi = \exp\left(Z - 1 - \ln Z + \frac{B}{V_r} + \frac{C}{2V_r^2} + \frac{D}{4V_r^4} + \frac{E}{5V_r^5} + G\right) \tag{3.22}$$

Table 3.2: Fugocity EOS Parameters for CH_4 (from Duan et al. (1992))

Parameter	CH_4
T_c [°K]	190.6
P_c [bar]	46.41
a_1	8.725539280E-02
a_2	-7.525994760E-01
a_3	3.754198870E-01
a_4	1.072913420E-02
a_5	5.496263600E-03
a_6	-1.847728020E-02
a_7	3.189931830E-04
a_8	2.110793750E-04
a_9	2.016828010E-05
a_{10}	-1.656061890E-05
a_{11}	1.196145460E-04
a_{12}	-1.080872890E-04
α	4.482622950E-02
β	7.539700000E-01
γ	7.716700000E-02

The calculation of the mole fraction of methane gas, y_{CH_4}, is conducted using Equations 3.23 and 3.24.

$$y_{CH_4} = 1 - y_{H_2O} \tag{3.23}$$

$$y_{H_2O} = \frac{x_{H_2O} P_{H_2O}^S}{\varphi_{H_2O} P} \exp\left(\frac{v_{H_2O}^l \left(P - P_{H_2O}^S\right)}{RT}\right) \tag{3.24}$$

where y_{H_2O} is the mole fraction of water in the gas phase, $P_{H_2O}^S$ is the saturation pressure of water, $v_{H_2O}^l$ is the approximation of the saturated liquid-phase molar volume of water, and φ_{H_2O} is the fugacity coefficient of H_2O in the gas phase. The mole fraction of H_2O in the liquid, x_{H_2O}, can be approximated as $1 - 2x_{Salt}$ in an aqueous salt solution.

The molar volume, $v^l_{H_2O}$, is calculated using the following equation of Wagner and Pruss (1993):

$$v^l_{H_2O} = \frac{\rho_{H_2O}}{MW_{H_2O}} \tag{3.25}$$

$$\rho_{H_2O} = \rho_c \left(1 + d_1\tau^{1/3} + d_2\tau^{2/3} + d_3\tau^{5/3} + d_4\tau^{16/3} + d_5\tau^{43/3} + d_6\tau^{110/3}\right) \tag{3.26}$$

where ρ_c is the critical density equal to 322 kg/m^3, MW_{H_2O} is the molecular weight of water, and parameter $\tau = 1 - T/T_c$ where T_c is the critical temperature equal to 647.096 K. The values for the parameters in Equation 3.26 are provided in Table 3.3.

Table 3.3: Parameters for Equation 3.26 (from Wagner and Pruss (1993))

Parameter	Value
d_1	1.99274064
d_2	1.09965342
d_3	-0.510839303
d_4	-1.75493479
d_5	-45.5170352
d_6	-6.74694450E+5

The calculation of the fugacity coefficient of water in the gas phase, $\ln\varphi_{H_2O}$, is accomplished using the following empirical equation, for which the regression parameters g_1-g_6 are presented in Table 3.4, as provided in Duan and Mao (2006):

$$\ln\varphi_{H_2O} = g_1 + g_2P + g_3P^3 + g_4PT + \frac{g_5P}{T} + \frac{g_6P^2}{T} \tag{3.27}$$

Shibue (2003) provides an effective method for calculating the vapour pressure, $P^S_{H_2O}$, for aqueous solutions of NaCl that expands upon the relationships introduced by Wagner and Pruss (1993) to include both temperature and concentration-dependent terms. The approach centres around solving Equations 3.28 and 3.29, which apply to NaCl aqueous solutions. It should be noted that the empirical relationship inherent in this calculation requires that pressure be in units of MPa.

$$\ln\left(\frac{P^S_{H_2O}}{P_c}\right) = \ln P_R + h(X) \tag{3.28}$$

Table 3.4: Parameters for Equation 3.27 (from Duan and Mao (2006))

Parameter	Value
g_1	-1.42006707E-2
g_2	1.08369910E-2
g_3	-1.59213160E-6
g_4	-1.10804676E-5
g_5	-3.14287155E00
g_6	1.06338095E-3

$$\begin{aligned} \ln P_R &= \frac{1}{T_R}\left[-7.85951783(1-T_R)+1.84408259(1-T_R)^{1.5}\right] \\ &+\frac{1}{T_R}\left[-11.7866497(1-T_R)^3+22.6807411(1-T_R)^{(3.5)}\right] \\ &+\frac{1}{T_R}\left[-15.9618719(1-T_R)^4+1.80122502(1-T_R)^{7.5}\right] \end{aligned} \tag{3.29}$$

where $T_R = T/T_c$, and P_c and T_c are the critical pressure and critical temperature calculated using the salt specific empirical equations for NaCl solutions (Equations 3.30 and 3.31).

$$T_c = 647.096 + q_1X^{0.5} + q_2X + q_3X^2 + q_4X^4 \tag{3.30}$$

$$P_c = 22.064 + q_5X + q_6X^2 + q_7X^3 + q_8X^4 + q_9X^5 + q_{10}X^6 \tag{3.31}$$

where X is the mole fraction of salt in solution and the regression parameters q_1-q_{10} for NaCl aqueous solutions are provided in Table 3.5. The empirical correction function for dissolved salt, $h(X)$, is calculated using one of two equations depending upon whether the solutions falls within the dilute solution range (Equation 3.32) or the concentrated solutions range (Equation 3.33); once again, these ranges are specific to the species of salt in solution, and are summarized in Table 3.5.

$$h(X) = \frac{a_2X}{X+a_1^2} + a_3X^2 \tag{3.32}$$

$$\begin{aligned} h(X) &= \left(\frac{a_2a_1^2}{(u+a_1^2)^2}+2a_3u\right)(X-u)+b_1(X-u)^2 \\ &+b_2(X-u)(X^2-u^2)+a_2u/(u+a_1^2)+a_3u^2 \end{aligned} \tag{3.33}$$

Table 3.5: Properties and Parameters for Calculation of Saturation Pressure of NaCl Aqueous Solutions (from Shibue (2003))

Parameter	NaCl Solution
q_1	8.78054E+1
q_2	2.42541E+3
q_3	-6.07779E+3
q_4	1.17033E+6
q_5	9.00404E+2
q_6	-2.92542E+4
q_7	1.39806E+6
q_8	-2.80756E+7
q_9	2.41637E+8
q_{10}	-7.18726E+8
Dilute Region	$0 \leq$ X ≤ 0.024
a_1	1.28746E-1
a_2	-7.31097E-1
a_3	-3.15058E+2
Concentrated Region	$0.024 \leq$ X ≤ 0.117
b_1	3.92767E+2
b_2	-2.46440E+3
u	0.024

The final term in Equation 3.19 to be solved is the activity coefficient, lnγ_{CH_4}, which can be expressed in terms of the excess Gibbs free energy of the solution (Denbigh and Denbigh, 1981) using the virial expansion provided below:

$$\ln\gamma = \sum_c 2\lambda m_c + \sum_a 2\lambda m_a + \sum_c \sum_a \xi m_c m_a \tag{3.34}$$

where λ and ξ are second-order and third-order interaction parameters, respectively, and c and a refer to the cation and anion concentrations in the solution (expressed as molality). The calculation of these interaction parameters, along with the value of $\mu_{CH_4}^{l(0)}/RT$, is accomplished using the pressure-temperature dependent relationship initially introduced by Busey (1984), provided in Equation 3.35 and regression coefficients in Table 3.6.

$$Parameter = c_1 + c_2T + c_3/T + c_4T^2 + c_5/T^2 + c_6P + c_7PT + c_8P/T + c_9P/T^2 + c_{10}TP^2 \tag{3.35}$$

Table 3.6: Interaction Parameters for Calculating $\mu^{l(0)}_{CH_4}/RT$, λ and ξ (from Duan and Mao (2006))

Parameter	$\mu^{l(0)}_{CH_4}/RT$	λ_{CH_4}	ξ_{CH_4}
c_1	0.83143711E+1	-0.81222036	-0.29903571E-2
c_2	-0.72772168E-3	0.10635172E-2	0
c_3	0.21489858E+4	0.18894036E+3	0
c_4	-0.14019672E-4	0	0
c_5	-0.66743449E+6	0	0
c_6	0.76985890E-2	0.44105635E-4	0
c_7	-0.50253331E-5	0	0
c_8	-0.30092013E+1	0	0
c_9	0.48468502E+3	0	0
c_{10}	0	-0.46797718E-10	0

Unlike in the determination of the three-phase equilibrium point for hydrate stability, finding the solubility of the guest gas does not require an iterative solution method, making this calculation far less computationally demanding than the former.

3.2.1 Validation of Thermodynamic Solubility Model

The saturation point of methane gas in both pure water and aqueous solutions has been investigated by a number of researchers, providing experimental results with which to evaluate the accuracy of the thermodynamic model used by this study. Culberson et al. (1950) provides experimentally determined methane solubility values for pure water systems at 298.15°K from 36 to 670 bar. These experimental values are in strong agreement with those later determined by Chapoy et al. (2004), which also provides experimental solubility data for pure water systems at temperatures of 275.11°K, 283.12°K, and 313.11°K. The impact of sodium chloride solutions on the solubility of methane gas was investigated by O'Sullivan and Smith (1970), providing data for pressures ranging from 100 atm to 600 atm, and solutions ranging in molality from 1 mNaCl and 4 mNaCl.

A comparison of the results provided by the thermodynamic predictive model used in this study and the experimental datasets is presented in Figures 3.2(a) to 3.2(d). From inspection of these figures, the thermodynamic model closely matches the experimental data for a variety of temperature, pressure, and salinity conditions. The average deviation between the thermodynamic model and the data provided by Chapoy et al. (2004) and the data of Culberson et al. (1950) are 0.94% and 9.9%, respectively; the higher deviation in the latter is understandable due to the larger degree of spread in the Culberson et al. (1950) dataset. The average deviation between the predictive model and the data provided by O'Sullivan and Smith (1970) is approximately 5% - with a higher deviation observed for the more saline solution. In general, these results suggest that the thermodynamic model used by this study can accurately predict the solubility of methane in both pure water and aqueous solutions of NaCl for a range of temperatures and pressures.

3.3 Methane Hydrate Stability Calculation

The model proposed by Sun and Duan (2007) is used to predict the stability of hydrates under three-phase equilibrium, taking into account the effects of temperature, pressure, and salinity. In this study, the stability of methane hydrates is expressed in terms of the pressure threshold for a given temperature and aqueous salt solution (ie. minimum pressure required for the formation of gas hydrates). The pressure threshold (or three-phase equilibrium point) of a gas hydrate is established at the point of equality between the chemical potentials of the various phases, such that:

$$\Delta\mu_w^H = \mu_w^\beta - \mu_w^H = \mu_w^\beta - \mu_w^L = \Delta\mu_w^L \tag{3.36}$$

where μ_w^H is the chemical potential of water in the hydrate lattice, μ_w^L is the chemical potential of water in the liquid phase, and μ_w^β is the chemical potential of water in the hypothetical empty hydrate lattice.

The statistical mechanics model proposed by Waals and Platteeuw (1959) is used to calculate $\Delta\mu_w^H$, as provided in Equation 3.37.

$$\Delta\mu_w^H = -RT\sum_{i=1}^{2} v_i \ln\left(1 - \sum_{j=1}^{N_C}\theta_{ij}\right) \tag{3.37}$$

where v_i is the number of i-type cages per water molecule (equal to 1/23 and 3/23 for the small and large cages of sI hydrate, respectively). θ_{ij} is the fractional occupancy of i-type cages with j-type guest molecules (CH_4 in this study), which is dependent upon the type of gas (guest) molecule as well as the size of the host cage. The expression for θ_{ij} is provided in Equation 3.38.

$$\theta_{ij} = \frac{C_{ij}f_j}{1 + \sum_{j=1}^{N_C} C_{ij}f_j} \tag{3.38}$$

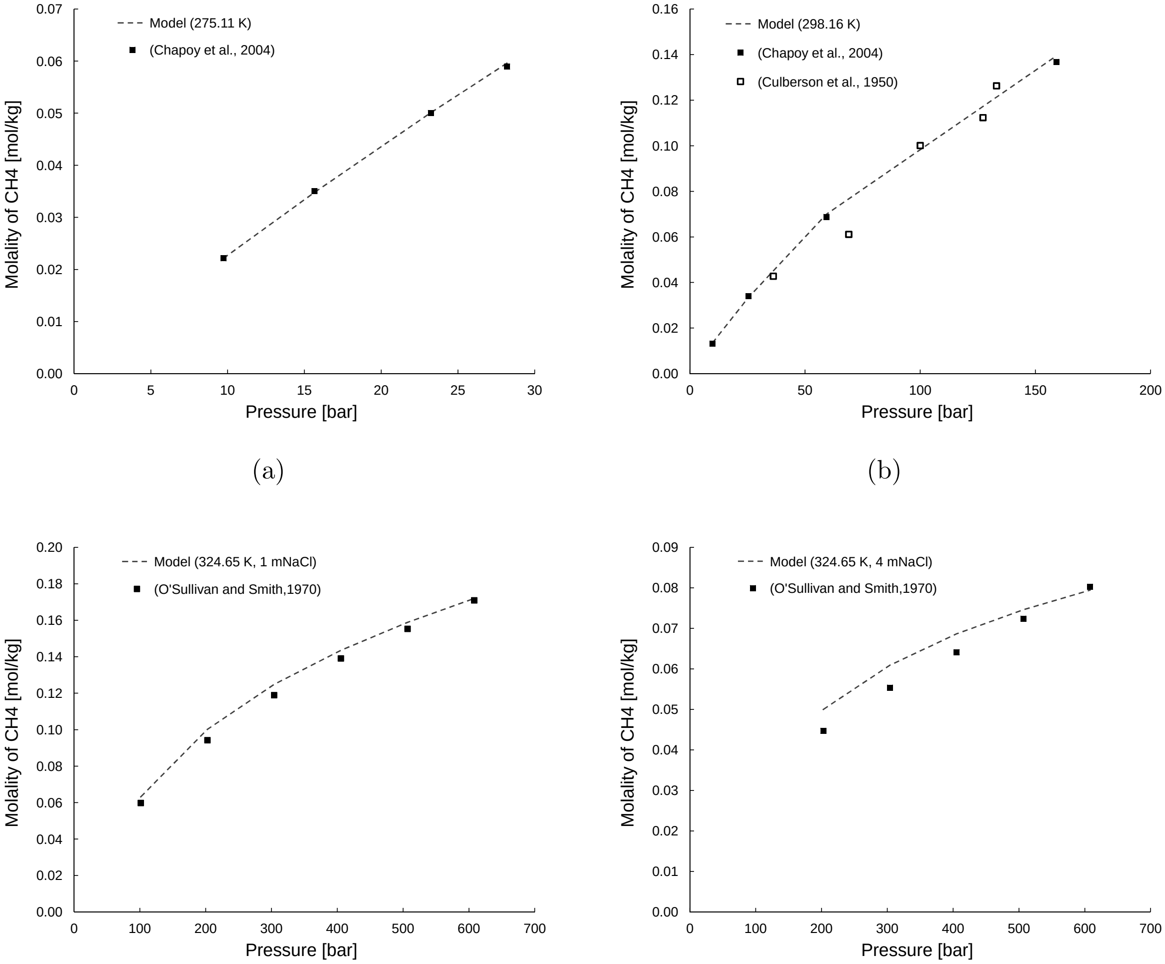

(a)

(b)

(c)

(d)

Figure 3.2: Calculated methane gas solubility using predictive thermodynamic model with experimental data for a) pure water at 275.11 K (Chapoy et al., 2004), b) pure water at 298.16 K (Chapoy et al., 2004; Culberson et al., 1950), c) aqueous solution of 1 mNaCl at 324.65 K (O'Sullivan and Smith, 1970), and d) aqueous solution of 4 mNaCl at 324.65 K (O'Sullivan and Smith, 1970).

C_{ij} is the Langmuir constant of gas component j in the i-type cages, R is the universal gas constant, and f_j is the fugacity of gas component j in hydrate phase solved using the same EOS method of Duan et al. (1992) introduced previously for the determination of gas solubility conditions where:

$$f = P\varphi \tag{3.39}$$

The Langmuir constant is specific to the guest molecule cage occupancy and a function of pressure and temperature. In the approach utilised by this study, the calculation of the Langmuir constant is undertaken using the Kihara potential model, in which the empirical parameters are based on experimental phase equilibrium data. This takes the form of the following equation:

$$C_j = \frac{4\pi}{kT} \int \exp\left(\frac{-\omega_{ji}(r)}{kT}\right) r^2 dr \tag{3.40}$$

where k is the Boltzmann constant, and $\omega_{ji}(r)$ is the cell Kihara potential of gas j in the i-type cage, solved using Equation 3.41.

$$\omega_{ji}(r) = 2z\epsilon \left(\frac{\sigma^{12}}{R_c^{11} r} \left(\delta^{\underline{10}} + \frac{a}{[R_c \delta^{\underline{11}}]} \right) - \frac{\sigma^6}{R_c^5 r} \left(\delta^{\underline{4}} + \frac{a}{[R_c \delta^{\underline{5}}]} \right) \right) \tag{3.41}$$

$$\delta^{\underline{N}} = \left(\left(1 - \frac{r}{R_c} - \frac{a}{R_c} \right)^{-N} - \left(1 + \frac{r}{R_c} - \frac{a}{R_c} \right)^{-N} \right) \frac{1}{N} \tag{3.42}$$

where z is the coordination number for the cages, R_c is the cage diameter, and a, ϵ and σ are regression parameters of the Kihara potential. The values of the Kihara parameters used in the calculation of the Langmuir constants for CH_4 vary slightly depending upon the source. For this study, the values provided by Sloan Jr and Koh (2007) were used and are presented in Table 3.7.

Table 3.7: Kihara Parameters for Langmuir Constant Calculation

Guest	Cage Size	z	R_c (pm)	a (pm)	ϵ/k (K)	σ (pm)
CH4	Large	20	432.6	38.34	154.54	316.50
	Small	24	390.5	38.34	154.54	316.50

Different approaches have been suggested by a number of sources including empirical approximations of Equation 3.40 (Sun and Duan, 2007; Dubessy et al., 1992a; Parrish and Prausnitz, 1972; Munck et al., 1988) and more complex ab initio quantum chemical methods (Sun and Duan, 2005), however, the use of Kihara potentials in this model seems to predict hydrate formation with sufficient accuracy compared to experimental data (see validation results in section 3.3.1). A notable limitation of this method of calculating the Langmuir constant is the need for Simpson's (or similar) numerical integration methods, which contributes to the computational runtime when applied to the regional model data.

The calculation of the $\Delta\mu_w^L$ term is performed using the following expression, introduced by Holder et al. (1980)

$$\frac{\Delta\mu_w^L}{RT} = \frac{\Delta\mu_w^0}{RT_0} - \int\limits_{T_0}^{T} \left(\frac{\Delta h_w^{\beta-L}}{RT^2}\right) dT + \int\limits_{0}^{P} \left(\frac{\Delta V_w^{\beta-L}}{RT}\right) dP - \ln a_w \tag{3.43}$$

$$\Delta h_w^{\beta-L} = \Delta h_w^0 + \Delta h_w^{\alpha-L} + \int\limits_{T_0}^{T} \Delta C_p dT \tag{3.44}$$

where $\Delta\mu_w^0$ is the reference chemical potential difference of water between the empty hydrate lattice and ice at the reference temperature, $T_0 = 273.15°K$, and zero pressure. $\Delta h_w^{\beta-L}$ is the enthalpy difference between water as a hydrate and in the liquid state, and Δh_w^0 is the enthalpy difference between the hydrate phase and ice at the reference temperature, T_0. ΔC_p is the difference in isobaric thermal capacity, which is dependent upon whether the temperature of the system is above or below the reference temperature, as presented in Table 3.8. Once again, due to the experimental determination of the thermodynamic reference properties used in the Holder et al. (1980) expression, there is considerable variation between the values provided by different sources; Tester et al. (2002) provides a thorough summary of the range in these parameters, however, for this study the values selected by Sun and Duan (2007) are used.

The difference in molar volume between hydrate and liquid water, $\Delta V_w^{\beta-L}$, can be calculated by taking the sum of the molar volume of water in the empty hydrate phase, V_w^β, and the molar volume of ice, V_w^{Ice}. Sun and Duan (2005) present expressions for V_w^β and V_w^{Ice}, which are presented below in Equations 3.45 and 3.46, respectively.

$$\begin{aligned} V_w^\beta &= 0.1 \times (11.820 + 2.217 \times 10^{-5} T + 2.242 \times 10^{-6} T^2)^3 \times \\ &\quad \frac{10^{-30} N_A}{N_w^\beta} \exp(-3.5 \times 10^{-4}(P-0.1) + 7.07 \times 10^{-6}(P-0.1)^{1.5}) \end{aligned} \tag{3.45}$$

$$V_w^{Ice} = 0.1 \times (1.912 \times 10^{-5} + 8.387 \times 10^{-10} T + 4.016 \times 10^{-12} T^2) \tag{3.46}$$

where N_w^β is the number of water molecules per hydrate cell (equal to 46 for sI hydrates of CH_4) and N_A is Avogadro's number. It should be noted that Equations 3.45 and 3.46 require the units of pressure to be MPa.

Table 3.8: Thermodynamic Properties for $\Delta\mu_w^L$ (from Sun and Duan (2007))

$\Delta\mu_w^0$	(J/mol)	1202
Δh_w^0	(J/mol)	1300
$\Delta h_w^{\alpha-L}$	(J/mol)	-6009.5
	where $T > T_0$	
$\Delta C_p^{\beta-L}$	(J/mol/K)	$-38.12 + 0.141(T - T_0)$
	where $T < T_0$	
$\Delta C_p^{\beta-\alpha}$	(J/mol/K)	$0.565 + 0.002(T - T_0)$

Although ions present in aqueous solution are not able to enter the hydrate lattice, and thus do not impact the chemical potential of the hydrate lattice, they do change the activity of the solution, impacting both the three-phase equilibrium conditions, as well as the solubility of methane in the solution (Sun and Duan, 2007); the activity, a_w, term is used to account for this effect in Equation 3.43. The scope of this study specifically focuses on the consideration of NaCl solutions involved in hydrate formation; however, the method can be expanded to consider other electrolyte solutions.

The approach for calculating the activity of the solution is based upon the Pitzer (1991) model, modified to include temperature-dependent parameter as determined by Spencer et al. (1990). Equation 3.47 is used to calculate the activity of the solution:

$$\ln a_w = -\frac{MW_{water} v m}{1000}\phi \tag{3.47}$$

where v is the stoichiometry of salt in solution (equal to the moles of cations and anions in a mole of salt), m is the molality of the salt solution, and ϕ is the osmotic coefficient. The value of ϕ is calculated using the following equation presented in Pitzer and Mayorga (1973):

$$\phi - 1 = -\frac{z^+ z^- A^\phi I^{0.5}}{1 + 1.2I^{0.5}} + \frac{2mv^+v^-B}{v^+ + v^-} + C^\phi m^2 \frac{2(v^+v^-)^{3/2}}{v^+ + v^-} \tag{3.48}$$

where z^+/z^- are the respective charges of the salt cations and anions, A^ϕ is the Debye-Hückel parameter for the osmotic coefficient, and I is the ionic strength of the salt solution. B and C^ϕ are the second and third virial coefficients, respectively; B is a function of the ionic strength, calculated using Equation 3.49, while C^ϕ (like A^ϕ) is considered to be independent of ionic strength, and calculated using the temperature-dependent empirical formula proposed by Spencer et al. (1990):

$$B = \beta^{(0)} + \beta^{(1)} \exp(-2I^{0.5}) \tag{3.49}$$

The second virial coefficient parameters $\beta^{(0)}$ and $\beta^{(1)}$, along with A^{ϕ} and C^{ϕ}, are calculated using Equation 3.50 along with the values provided in Table 3.9.

$$Par = c_1 + c_2T + c_3/T + c_4\ln T + c_5T^2 + c_6T^3 \tag{3.50}$$

Table 3.9: Temperature Adjustment Constants for NaCl Solution Parameters of the Pitzer Model (from Spencer et al. (1990))

Parameter	A^{ϕ}	$\beta^{(0)}_{Na,Cl}$	$\beta^{(1)}_{Na,Cl}$	$C^{\phi}_{Na,Cl}$
c_1	86.6836498	7.87239712	8.66915291E+2	1.70761824
c_2	8.48795942E-2	-8.3864096E-3	0.606166931	2.32970177E-3
c_3	-1.32731477E+3	-4.96920671E+2	-1.70460145E+4	-1.35583596
c_4	-17.6460172	-0.82097256	-1.671717296E+2	-0.387767714
c_5	-8.88785150E-5	1.4413774E-5	-4.8048921E-4	-2.46665619E-6
c_6	4.88096393E-8	-8.7820301E-9	1.88503857E-7	1.21543380E-9

The determination of the pressure threshold is achieved by providing the system temperature and salinity, and then iteratively solving for the value of pressure that satisfies the equality between Equations 3.37 and 3.43. Based on these three inputs, $\Delta\mu_w^0$, $\Delta h_w^{\beta-L}$, $\Delta V_w^{\beta-L}$, θ_{ij}, and $\ln a_w$ are calculated and used to determine values of $\Delta\mu_w^H$ and $\Delta\mu_w^L$ using Equations 3.37 and 3.43, respectively. This process is repeated for iterations of pressure until the equality, $\Delta\mu_w^H = \Delta\mu_w^L$, is met. The tolerance used for this study was a difference of 0.01%, which seemed to yield good results, although there is an inherent trade-off for solution precision and computational run-time.

Because of the highly non-linear nature of this solution, and need for iterative approaches to determine hydrate pressure thresholds, this approach is computationally demanding. To reduce the computation time associated with calculating the pressure threshold for hydrate formation associated with the exact salinity, temperature and pressure of each location and time, characteristic curves were generated for the range of salinities (NaCl concentrations) across the observed ranges in temperature and pressure. Hydrate pressure thresholds were then determined at each point by interpolating between the characteristic curves using the temperature and salinity values extracted from the regional-scale model results.

3.3.1 Validation of Thermodynamic Hydrate Stability Model

A number of researchers provide experimentally determined three-phase equilibrium points for both pure water and aqueous solutions, which can be used to evaluate the accuracy of the thermodynamic model used in this study. De Roo et al. (1983) provides a quality data set of methane hydrate stability limits for pure water and aqueous NaCl solutions for pressures up to 110 bar and concentrations up to 5.5 mNaCl. Jager and Sloan (2001) later provided a data set with a greater pressure range, extending up to 700 bar and concentrations of 4.8 mNaCl. Kharrat and Dalmazzone (2003) provides limited data for the three-phase equilibrium point of methane hydrate in pure water and NaCl solutions; however, this data *does* overlap with measurements conducted by Jager and Sloan (2001) and De Roo et al. (1983), which allows for a comparison of the different datasets. From inspection of Figures 3.3(a) to 3.3(d), the experimental datasets provide consistent determinations of the methane hydrate three-phase equilibrium point.

The ability of this model to predict the three-phase equilibrium point for methane hydrate in pure water is very high, with an average deviation of about 3.1% from the experimentally determined values of hydrate stability pressure. The model predicts the three-phase equilibrium point in aqueous solutions of NaCl, with average deviations of 2.7%, 4.3% and 6.1% for the NaCl solutions of 1.1m, 2.1m and 5.9m, respectively. As with the solubility model, the accuracy seems to decrease as the molality of NaCl increases; however, the deviation remains within an acceptable limit, suggesting that this thermodynamic model is capable of accurately predicting the three-phase equilibrium point of methane in pure water and NaCl solutions.

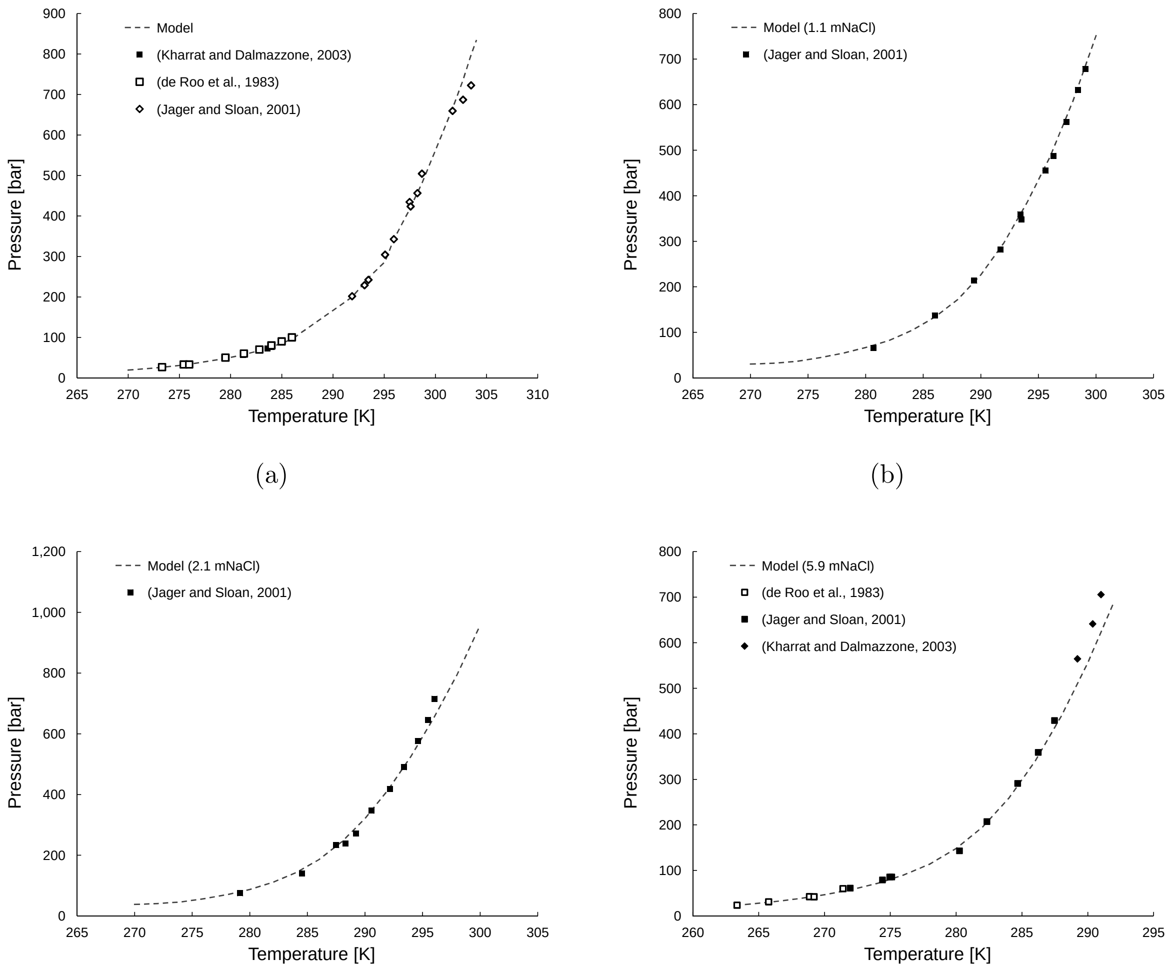

(a) (b)

(c) (d)

Figure 3.3: Calculated methane hydrate stability using predictive thermodynamic model with experimental data for a) pure water (De Roo et al., 1983; Jager and Sloan, 2001; Kharrat and Dalmazzone, 2003), b) aqueous solution of 1.1 mNaCl (Jager and Sloan, 2001), c) aqueous solution of 2.1 mNaCl (Jager and Sloan, 2001), and d) aqueous solution of 5.9 mNaCl (De Roo et al., 1983; Jager and Sloan, 2001; Kharrat and Dalmazzone, 2003).

Chapter 4

Results of Paleo-Simulation

A primary goal of the analyses of this study is to determine whether the conditions for methane hydrates to form in the subsurface have arisen at the Bruce nuclear site during periods of glaciation in southern Ontario. This study was undertaken to provide a first assessment of whether the potential impacts of these paleo- methane hydrates should be considered in the design of the proposed DGR. Upon confirming the potential for hydrates to form, this study provides a first attempt at estimating the potential duration and spatial extent of these hydrate stability zones. The output files generated from the transient modelling of temperature, pressure and salinity across the regional domain were combined and processed using the thermodynamic methane hydrate stability and methane solubility models.

Based on the methodology employed by this study, conditions conducive to the formation of methane hydrates are achieved within portions of the study site during the 120 thousand year modelling period. A detailed discussion of the evolution of pressure and salinity profiles in the model domain is provided by Sykes et al. (2011). This chapter will therefore focus on the more novel results pertaining to the temperature profile, hydrate stability zones and methane saturation across the study site. In addition to the figures and results presented in this chapter, block-cut figures and fence diagrams of the regional-scale model are provided in Appendix B showing the initial conditions at the start of the simulation, and at the points of maximum potential hydrate extent.

4.1 Temperature Model

In order to estimate the extent of a hydrate stability zone and methane solubility in the subsurface, it was necessary to have site-wide estimates of the temperature for the duration of the study period. Since these values were not provided in the regional-scale model previously developed by Sykes et al. (2011), a simplified approach to numerically model temperature was undertaken by this study. The simplified modelling approach was undertaken using FRAC3DVS-OPG with lithology-dependent geothermal parameters applied to the various model layers. A constant heat flux equal to 45 W/m^2 was applied to the base of the model, while sub-glacial temperatures calculated by Peltier (2011) were applied as a distributed transient Dirichlet boundary condition along the top of the model. Figure 4.1 presents the temperature histories for points within various formations at two locations within the study domain: a) at the Bruce nuclear site, and b) approximately 45 km to the east of the Bruce nuclear site, closer to the eastern edge of the Michigan basin.

Temperatures near the surface of the regional domain fluctuate over time, while generally demonstrating a decreasing trend until they undergo an eventual recovery at approximately 12 ka before present. As expected, deeper locations within the study domain experience less of this temperature fluctuation as the overlying materials act as a thermal buffer from atmospheric variations. However, as formations pinch out towards the basin margins, the older formations become more exposed to the atmospheric conditions. This can be seen by comparing the temperature profiles of the Niagaran, Cobourg and Shadow Lake formations presented in Figures 4.1(a) and 4.1(b).

It is understood that the method employed by this study to model the transient temperature distribution in the subsurface is overly simplified by not including such potentially important processes as convective heat transport by flowing waters or the effect of latent heat storage. However, these results are meant to represent a first approximation of temperatures across the model domain to permit the estimation of methane hydrate stability, which is the focus of this study. Because temperature, pressure and salinity modelling is undertaken independent of the thermodynamic models, the framework used by this study allows for future improvement on how temperature is modelled at the study site. In addition, the sensitivity of the results of this study are examined with respect to temperature in the following section (Section 4.2).

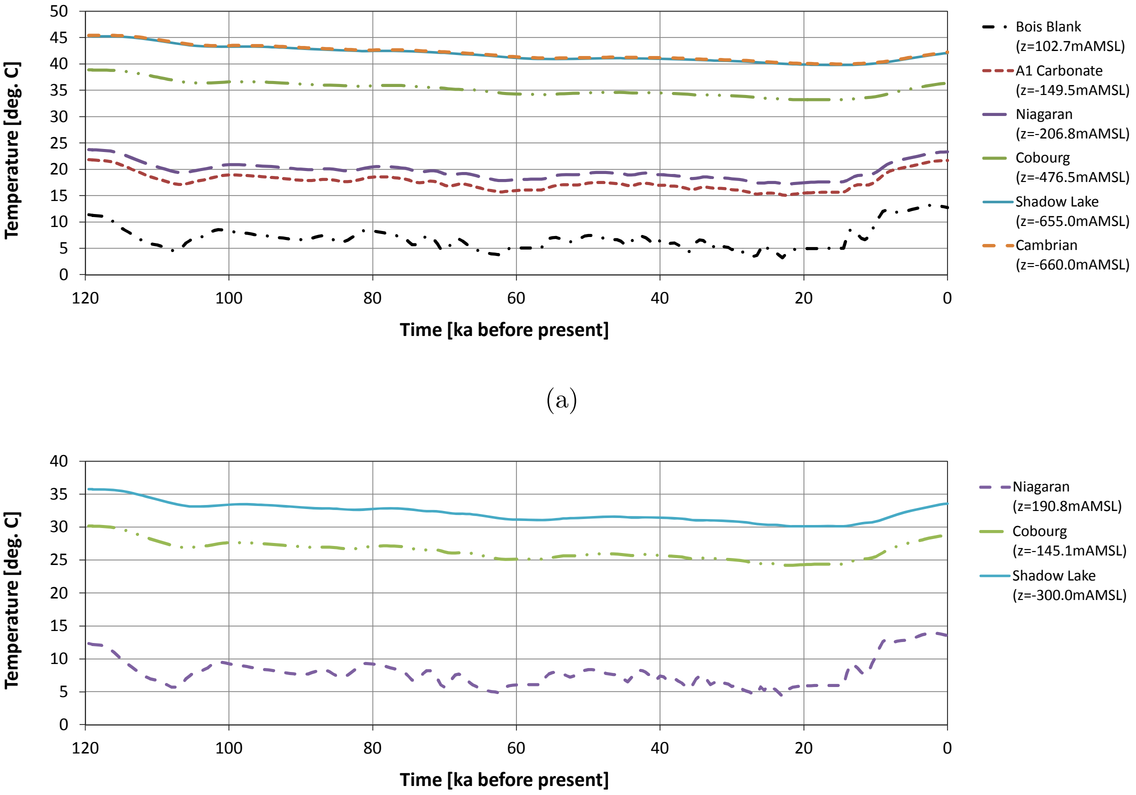

(a)

(b)

Figure 4.1: Temperature histories for various formations at a) the Bruce nuclear site (NAD83 UTM 17N 4.54139x10^5E 4.90778x10^6N) and b) 45 km to the east toward the basin edge (NAD83 UTM 17N 4.99040x10^5E 4.90778x10^6N).

4.2 Methane Hydrate Stability Results

The results of thermodynamic modelling of methane hydrate stability at the Bruce nuclear site have shown that there are periods in which potential hydrate formational zones are present based on the pressure, temperature and salinity profiles. Figure 4.2 shows that there are in fact two separate periods during which hydrate stability conditions arise in the study domain, the details of which are presented in Table 4.1. The second of the two hydrate stability periods was found to be the larger of the two, both in spatial extent (occupying 11.3% of the study domain volume) and duration (lasting 9,500 years). The timing of these two hydrate stability periods correspond to the two periods of ice sheet cover identified by the UoT Glacial Systems Model (Peltier, 2011).

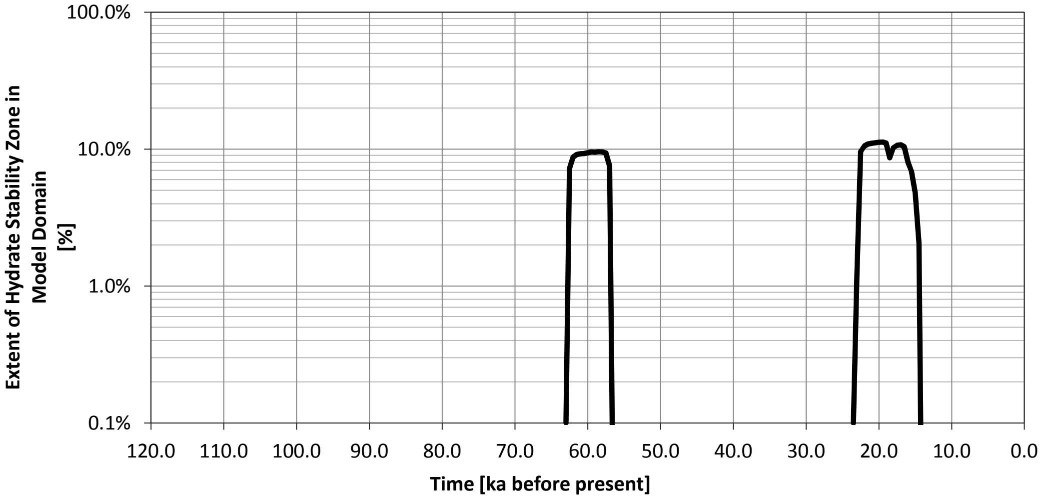

Figure 4.2: Percentage of model domain volume where pressure, temperature and salinity conditions are conducive to methane hydrate stability during the study period.

Table 4.1: Summary of Potential Methane Hydrate Stability Periods

Duration	**Max. Extent**	**Max. Depth (Elevation)**
Period 1		
6.5 ka	9.51% Domain Volume	-417.0 mAMSL
(62.5 kaBP to 56.0 kaBP)	(58.5 kaBP)	(57.5 kaBP)
Period 2		
9.5 ka	11.28% Domain Volume	-437.8 mAMSL
(23.0 kaBP to 13.5 kaBP)	(19.5 kaBP)	(16.5 kaBP)

Note: Percent volume of model domain calculated using volumetric integration feature in Tecplot 360™.

The evolution of the temperature, pressure, and salinity at discrete points within the Niagaran (Figure 4.3(a)) and Salina E (Figure 4.3(b)) formations are presented to demonstrate the application of the predictive hydrate stability and methane saturation models - although the latter is considerably more straightforward since the thermodynamic model generates a direct estimation of the saturation limit. The conditions required for the stability of gas hydrates can be conceptualized as a *hydrate stability threshold* (pressure) that is a function of temperature and salinity, and must be exceeded by formation pressures in order for hydrates to form.

Further evidence that the two periods of hydrate stability are separate and distinct can be seen by reviewing the pressure, temperature and salinity histories at specific observation points within the study domain (Figure 4.3). As can be seen in Figure 4.3, the shallower Salina E observation point undergoes two periods during which the formation pressures exceed the hydrate stability threshold, while there is only one period of hydrate stability at the observation point within the Niagara formation. From these results it can be seen that the later of the two hydrate stability periods extends deeper into the subsurface as a result of a higher pressure peak and lower salinities and temperatures than in the previous stability period.

For consideration of the spatial extent of the two periods of hydrate stability, the fence diagram montages in Figures 4.4(a) and 4.4(b) illustrate the evolution of the potential hydrate formational zones across the site during the two periods of anticipated hydrate stability. At the first instance of hydrate stability conditions (62.5 kaBP), the region of potential hydrate formation evolves quickly to include the majority of the Devonian lithologic units and many of the Silurian units where they become shallow toward the north east end of the site (Figure 4.4(a)). The extent of the potential hydrate formational zone gradually expands during this period to include nearly all of the Silurian units where they pinch out against the basin limits (Algonquin Arch). Toward the basin centre, the hydrate stability zone does not extend past the shallowest units of the Upper Silurian. After the maximum extent of the hydrate stability zone at approximately 58.5 kaBP, the stability region begins to recede as excess pressure (above the hydrate stability threshold) begins to dissipate across the site.

The onset of the second occurrence of hydrate stability (Figure 4.4(b)) begins at 23 kaBP in the shallow Devonian layers. The stability zone quickly expands to include all of the Devonian and the shallow units of the Upper Silurian. As was the case in the earlier stability period, the region of potential hydrate formation extends down to include all of the Silurian units toward the north east corner of the study domain where these lithological units pinch out against the edge of the basin, while the limit of the stability zone is restricted to the shallowest units of the Upper Silurian toward the basin centre. Although there is a slight drop-off in the formation pressure (and therefore the excess pressure for hydrate stability) after the maximum hydrate extent at 19.5 kaBP, conditions conducive to hydrate stability are sustained across much of the surface of the site despite this pressure lull until the end of the second stability period at 14.5 kaBP.

Cross-sections of the site showing the extent of hydrate stability superimposed on lithologic layers and key parameters (pressure, salinity and temperature) are provided at the maximum spatial extent of hydrate stability for the first (Figure 4.5) and second (Figure 4.6) periods of potential hydrate formation. Comparison of the hydrate stability extent

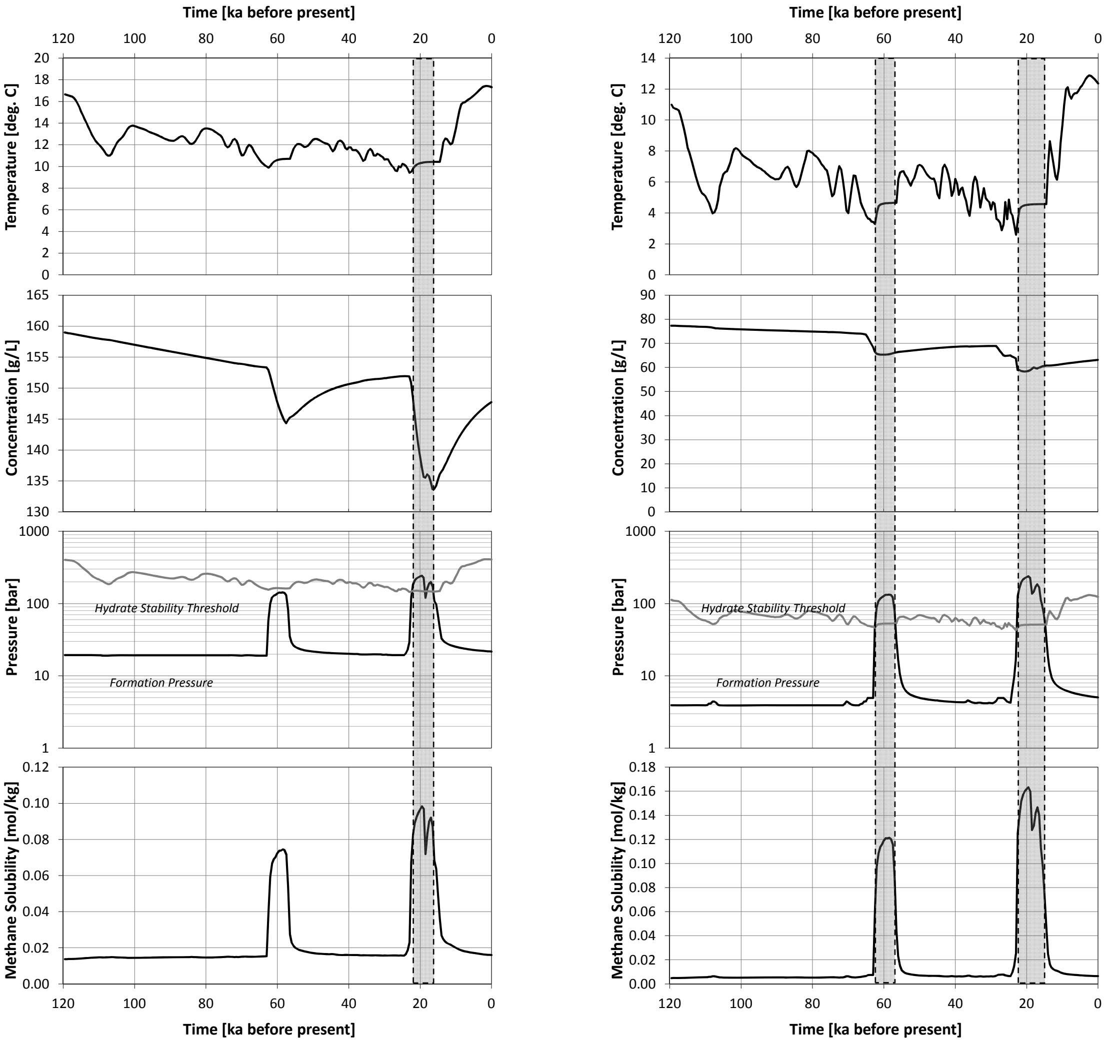

(a)

(b)

Figure 4.3: Evolution of temperature, salinity, pressure, hydrate stability, and methane solubility during the study period for discrete observation points in the a) Niagaran (NAD83 UTM 17N 4.95607x10^5E 4.88316x10^6N, Z=107 mAMSL), and b) Salina E (NAD83 UTM 17N 4.95607x10^5E 4.88316x10^6N, Z=250 mAMSL) Formations. Note that periods of hydrate stability are delineated by the shaded regions.

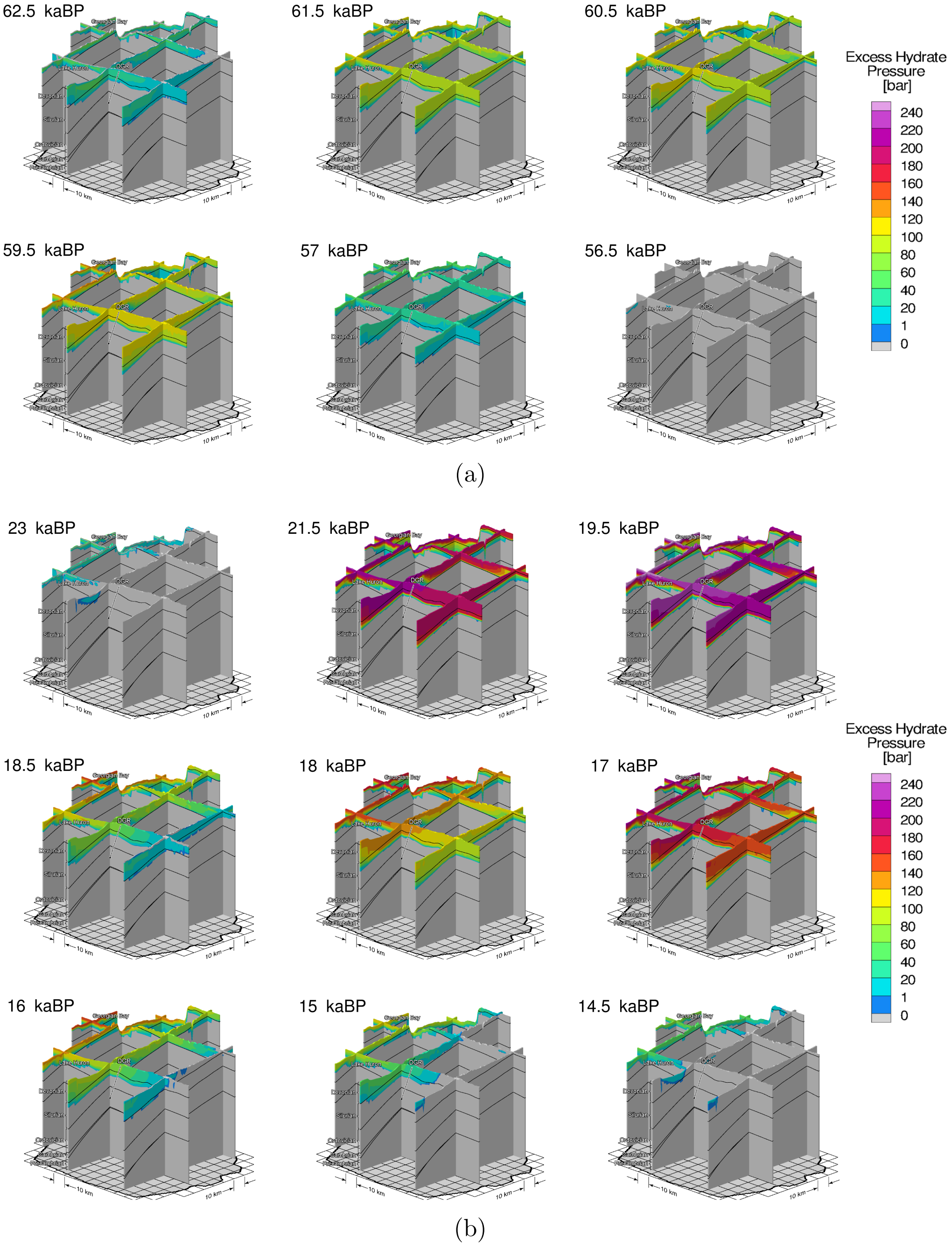

(a)

(b)

Figure 4.4: Fence diagrams illustrating evolution of potential hydrate formational zones (in units of bars above stability threshold) during a) first (62.5 to 56.0 kaBP) and b) second (23.0 to 13.5 kaBP) periods of hydrate stability.

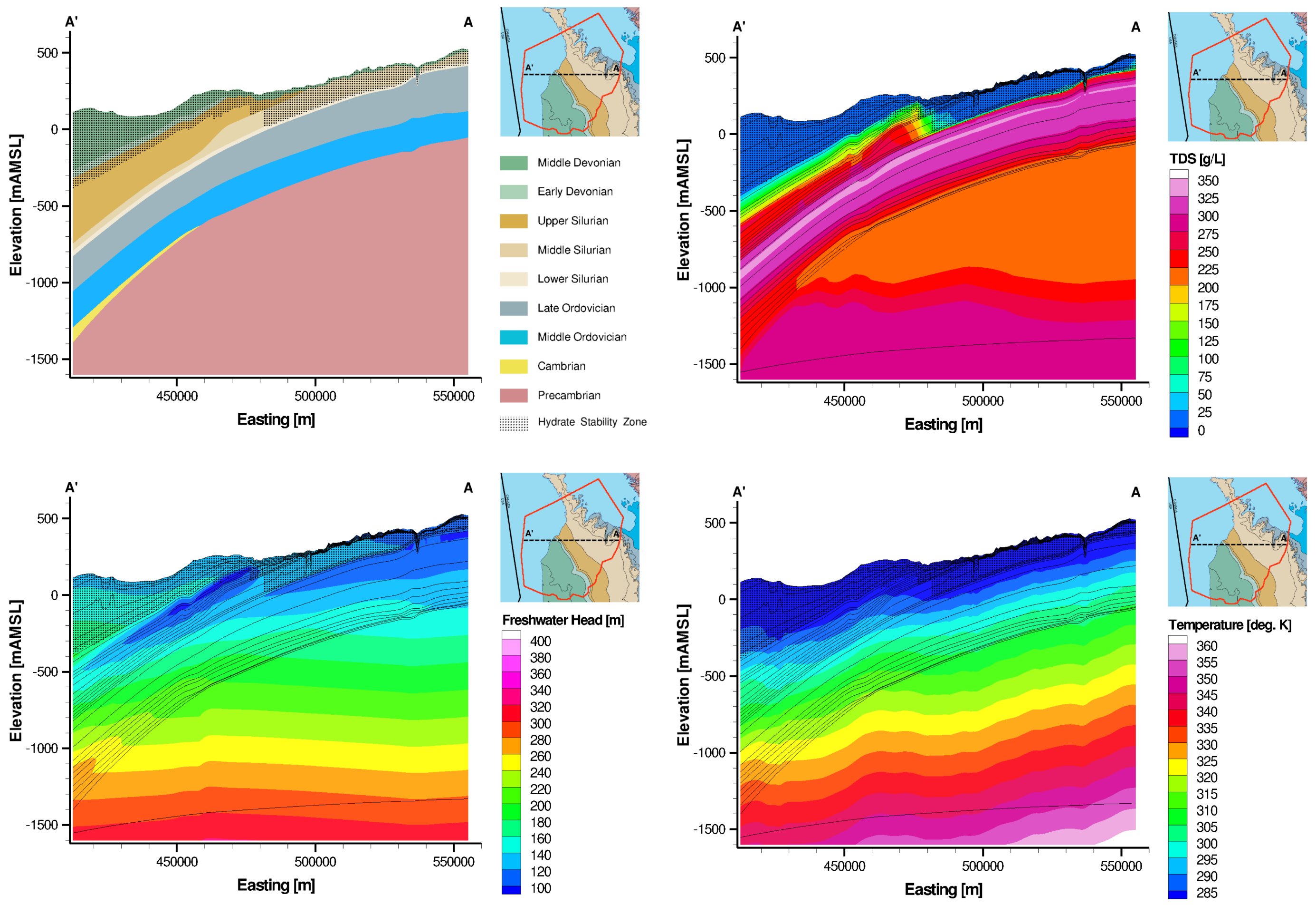

Figure 4.5: Cross-sectional view of spatial distribution of methane hydrate stability (delineated by shaded region) and key parameters at 58.5 kaBP (first glacial period).

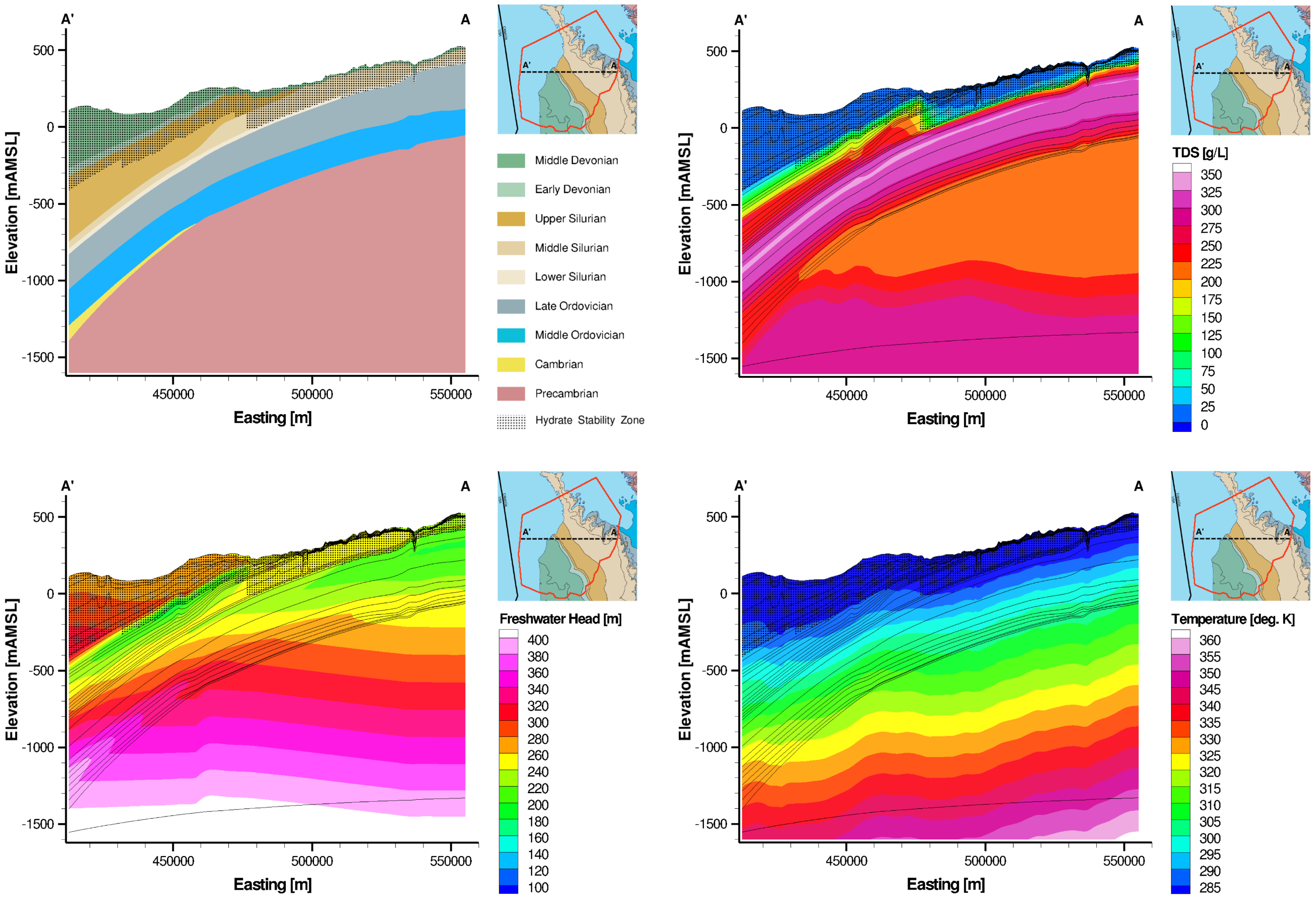

Figure 4.6: Cross-sectional view of spatial distribution of methane hydrate stability (delineated by shaded region) and key parameters at 19.5 kaBP (second glacial advance).

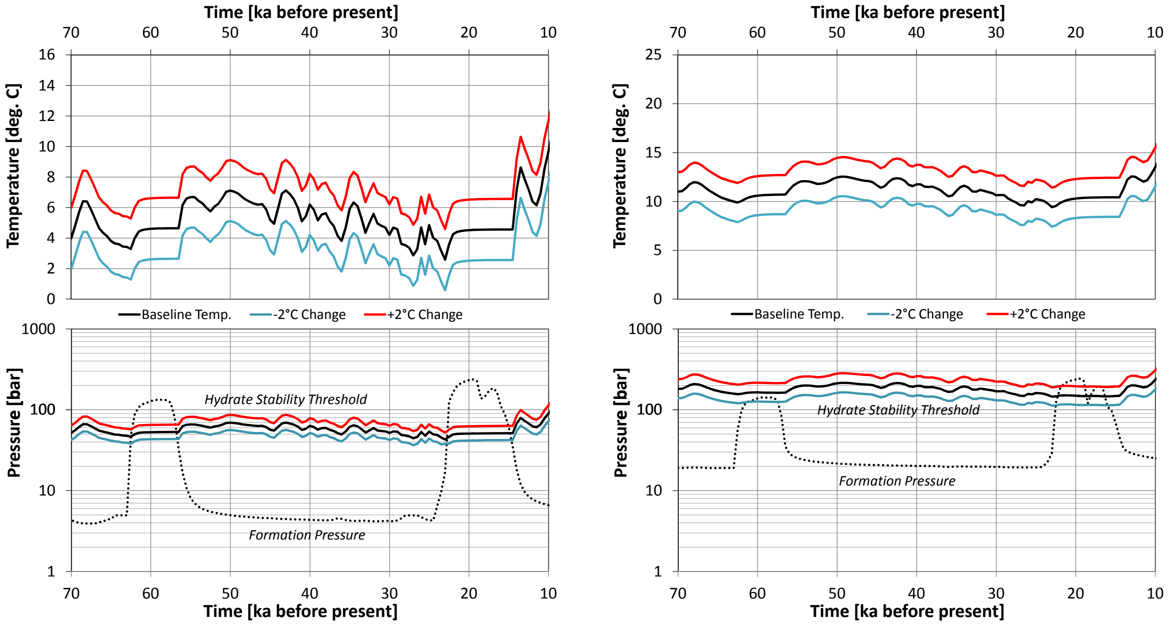

(a) (b)

Figure 4.7: Sensitivity of methane hydrate stability results to modelled temperature profile, presented at discrete points within the a) Niagaran (NAD83 UTM 17N 4.95607x10^{5}E 4.88316x10^{6}N, Z=107 mAMSL), and b) Salina E (NAD83 UTM 17N 4.95607x10^{5}E 4.88316x10^{6}N, Z=250 mAMSL) Formations.

with lithologic layers once again demonstrates how the potential formational zone extends into the older Late Ordovician units towards the east end of the site, while being restricted to only the Upper Silurian units towards the basin centre. By investigating the distribution of key parameters along the same cross-section, it can be seen that pressure and salinity are largely responsible for this trend: a region of low pressure appears in the Upper Silurian units extending west from an easting of approximately 4.8x10^{5}m. This location also marks a dramatic shift in TDS from the fresher waters near the surface to hypersaline brines in the intermediate geologic zone, which raise the threshold pressure required for hydrate stability.

Due to the simplified approach used in this study to estimate the subsurface temperature profile during the study period, a sensitivity analysis was undertaken by adjusting the modelled temperatures by +/-2°C and re-evaluating the methane hydrate stability threshold for the discrete points presented in Figure 4.3. In general, the results of this sensitivity analysis (Figure 4.7) show that increasing the temperature by 2°C will reduce the extent of potential hydrate stability conditions. This can be seen in the deeper Niagaran location (Figure 4.7(a)), where the second hydrate formational period (corresponding to the second period of glacial advance) only exceeded the stability threshold for a period of approximately 3ka (compared to original estimates of approximately 9.5 ka). The estimates of hydrate stability in the shallower units (such as the Salina A formation, presented in Figure 4.7(b)) are less sensitive to modelled temperature results, with subsurface pressures during both of the two glacial episodes being sufficient to exceed the hydrate stability threshold calculated with increased temperature inputs. These results suggest that the extent and duration of the potential methane hydrate stability zone is sensitive to underestimates of temperature, particularly in the deeper units due to formation pressures that exceeded the hydrate stability threshold by only a small margin. The shallower units, however, experienced formation pressures that far exceeded the local hydrate stability threshold, making them considerably less sensitive to error in the estimated temperature profile.

4.3 Methane Solubility Results

In order for methane hydrates to form, there must be sufficient methane present to exceed the local solubility limits of the aqueous (groundwater) solution. To this end, the methane solubility across the site was determined by using the temperature, pressure and salinity outputs of the regional-scale numerical model as input parameters for the predictive thermodynamic model based on the theory proposed by Sun and Duan (2007), as described in Section 3.2. In general, the results of the methane solubility modelling show that the saturation limit remains relatively low and stable for the periods without ice sheet cover, and undergoes drastic increases during the two periods of glacial advance (Figure 4.8).

During the periods without glacial cover, the methane solubility in the groundwater remains relatively low, and does not exceed 0.09 mol/kg at any point within the study domain. When ice sheets advance across the site, the methane solubility increase drastically across the site, with a maximum solubility of 0.26 mol/kg achieved during the second period of glacial advance; this response is predicted by Henry's Law, according to which an increase in (formation) pressure will result in an increase in the solubility of a gas in solution. The extent of the mechanical loading impact by glaciers can be inferred from Figure 4.8, where all three curves undergo an appreciable increase during these periods. These increases are presented quantitatively in Table 4.2.

The irregular spatial distribution of methane solubility across the site is understandable considering the complex relationship with temperature, pressure and salinity, and the irregular distribution of these parameters across the study area. While temperature and

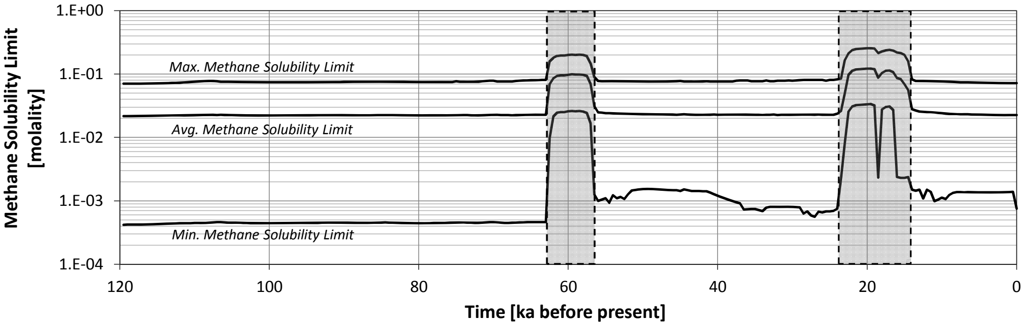

Figure 4.8: Methane solubility (maximum, minimum, average) across the domain for the 120 ka study period. Shaded regions delineate the timing of the two episodes of glacial advance across the study site.

Table 4.2: Summary of increases in methane solubility (molality = mol/kg) during periods of ice sheet loading at the site.

Methane Solubility:	**Maximum**	**Minimum**	**Average**
Interglacial Period	0.0889	0.0004	0.0228
First Glacial Period	0.2026	0.0097	0.0912
(% increase from interglacial)	*128.0%*	*2212.8%*	*299.4%*
Second Glacial Period	0.2563	0.0023	0.1000
(% increase from interglacial)	*188.4%*	*447.5%*	*338.1%*

pressure both generally follow an increasing trend with depth, their respective impacts on the solubility of methane are opposite to one another (ie. increasing temperature reduces solubility - increasing pressure increases solubility). Salinity also has an inverse relation to solubility, however, this parameter is governed largely by lithology and does not strictly adhere to a depth-dependent generalization on a site-wide scale due to the sloping and pinching-out of formations.

Figure 4.9 presents the distribution of methane solubility along with the key parameters (pressure, salinity and temperature) at a cross-section of the site at the end of the study period. In interpreting these figures, recall that methane solubility during interglacial periods remains fairly constant such that the solubility at the last time step of the analysis is fairly representative of prior interglacial times. From inspection, it can be seen that solubility generally increases with depth during interglacial periods with an exception being at the western side of the study area. This region of increased solubility can be attributed to the low salinity in the deeper formations at this location, combined with increased formation pressures associated with depth. During these interglacial periods, the high pressures deep in the sedimentary basin overcome the inverse impacts of salinity and temperature, resulting in the generally increasing trend in solubility across the depth of the model domain.

The distribution of methane solubility and the key parameters are presented for the two periods of glacial advance in Figures 4.10 and 4.11 for the same cross-section. In contrast to the interglacial periods, during the periods of glacial advance the highest solubility values occur at the top of the model domain during glacial loading, and tend to decrease with depth into the older geological units. This shift in the methane solubility regime occurs in response to the high pressure loads imparted by the overlying glaciers to the shallower formations. From inspection of Figures 4.10 and 4.11, it can be seen that solubility decreases sharply around the Middle Silurian Units, where the groundwater geochemistry shifts from fresh to hypersaline. Expectedly, the higher pressures present during the second glacial advance result in larger solubility values at the site, although the solubility spike in the shallow units sharply decreases along similar boundaries as in the first glacial advance - around the Niagaran/Fossil Hill to the east, and the upper Salina units to the west. Beyond the Ordovician sedimentary units, the interglacial trend of increasing solubility with depth is restored, although solubility remains lower than the values at the top of the domain.

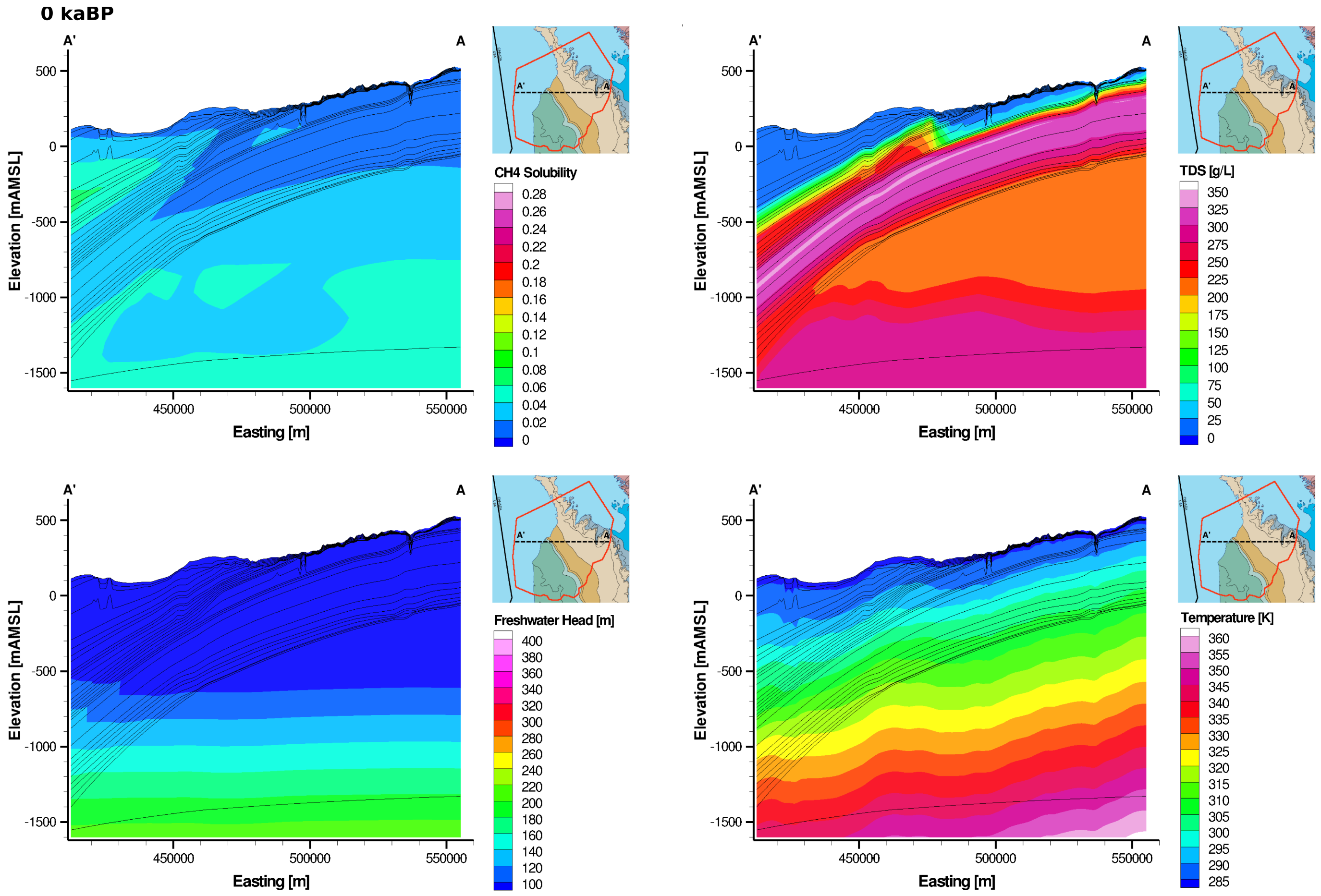

Figure 4.9: Cross-sectional view of spatial distribution of methane solubility [mol/kg] and key parameters at the end of the study period.

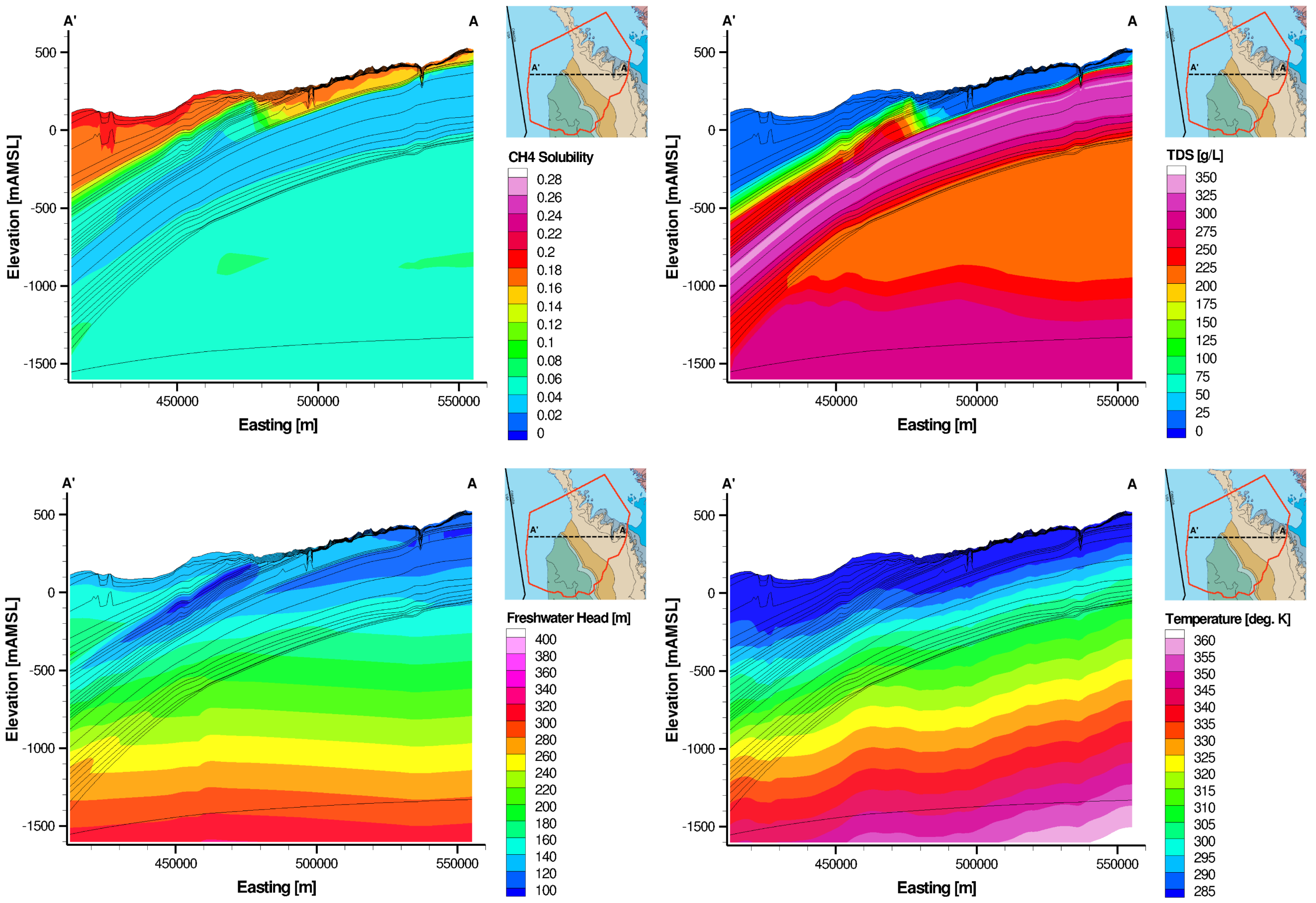

Figure 4.10: Cross-sectional view of spatial distribution of methane solubility [mol/kg] and key parameters at 58.5 kaBP (first glacial period).

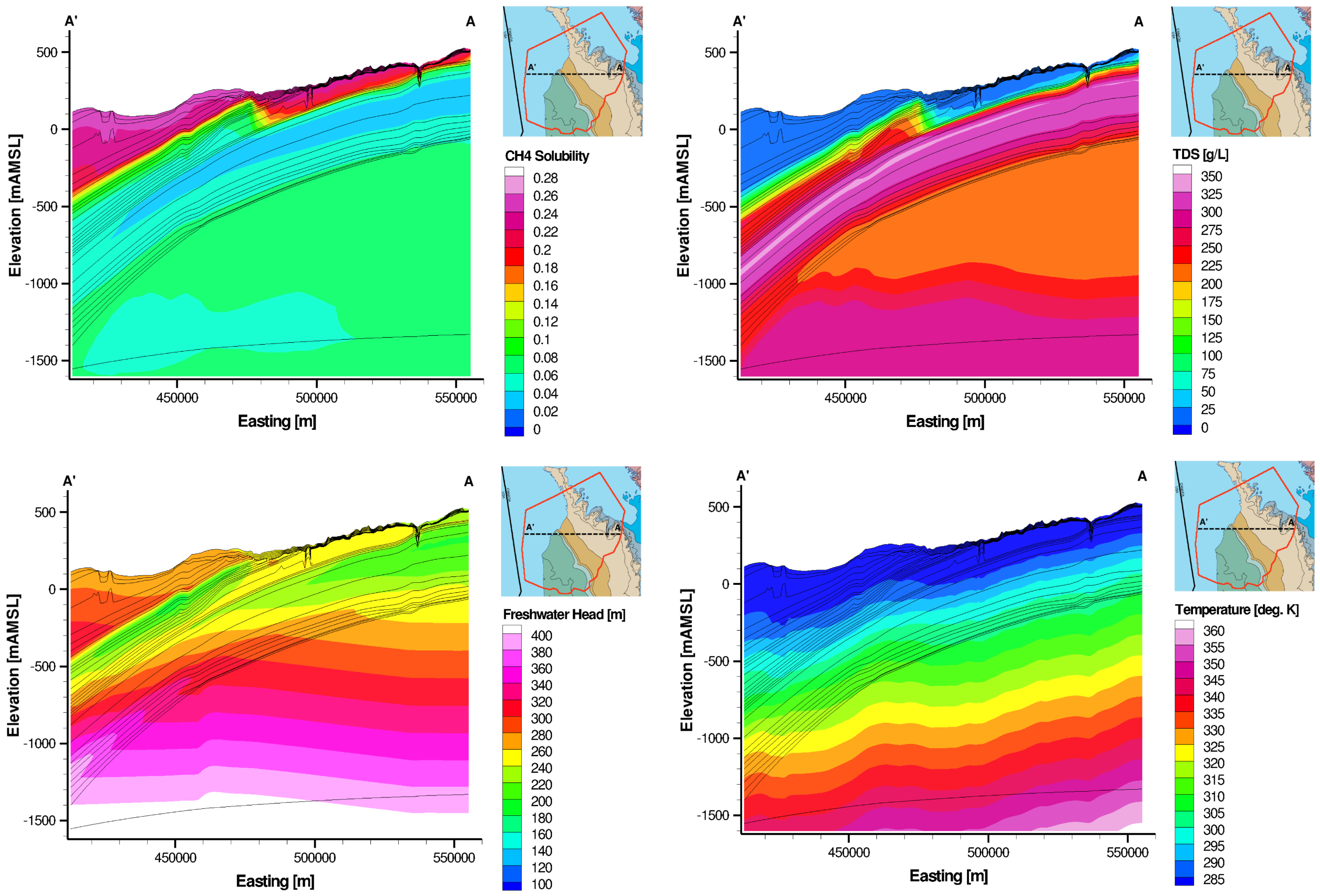

Figure 4.11: Cross-sectional view of spatial distribution of methane solubility [mol/kg] and key parameters at 19.5 kaBP (second glacial advance).

Chapter 5

Discussion

The modelling results presented in the previous chapter show that the pressure, temperature and salinity conditions conducive to the formation of methane hydrates in the subsurface were achieved within the study area during two separate periods corresponding to glacial advances across the region. These results represent a first attempt at evaluating the presence of paleo-methane hydrates in the region, and therefore provide a spatial and temporal context for discussing their specific impacts on the evolution of groundwater and hydrogeochemistry within the region.

5.1 Methane Hydrates as a Barrier to Meltwater Penetration

During the periods of glacial advance, mechanical loading from the ice sheets imposed significant increases in hydraulic head upon the underlying groundwater systems. The result is the generation of large lateral (basin-ward) hydraulic gradients as the ice sheets override the recharge areas where the sedimentary units outcrop at the ground surface (Bense and Person, 2008; McIntosh et al., 2010). Because the extent of meltwater penetration is strongly dependent upon the permeability of the sedimentary rocks, and the presence of fractures and conductive faults (Lemieux and Sudicky, 2010), the formation of methane hydrates within the more hydraulically conductive formations where they subcrop would reduce the effective permeability and limit the degree of subglacial recharge or pore fluid efflux. The Salina A1 Carbonate and Guelph (included in the Niagaran Group) regional aquifer units are considered to be likely conduits for meltwater penetration for these reasons. The coverage of these two units by the potential hydrate formational zone estimated by this study is presented in Figures 5.1 and Figure 5.2, respectively.

The pressure-temperature-salinity conditions conducive to the stability of methane hydrates within the subcrop areas (and extending farther basin-ward) in both the Guelph (Niagaran) and Salina A1 Carbonate units suggests that the impact of paleo-methane hydrates within the sedimentary aquifer units in conceptual models of Pleistocene glaciation and recharge should be considered. Supporting modelling work could be conducted to explore the case where the presence of hydrates results in reduced permeability in these key subcrop areas, and the influence on glacial, inter-glacial and post-glacial hydraulic head distributions across the study area.

The interpretation of basin hydrogeochemistry in the context of paleo- methane hydrates is fraught with considerable challenges: firstly, the indicators of methane hydrate dissociation are not necessarily differentiable from a number of other antecedent, concurrent and subsequent diagenic or hydrogeologic processes. Secondly, the understood signatures of methane hydrates are not necessarily preserved in the subsurface over the period of approximately 10,000 years since their dissociation at the end of the last glacial cycle - particularly in the shallower subcrop regions where there is more flux of meteoric water. Furthermore, the presence of methane hydrates would simultaneously limit the extent of freshening by meltwater penetration (due to the constriction of permeability in the recharge areas), and result in local freshening of the groundwater, driven by the salt excluding nature of hydrate structures and the freshening that ensues during dissociation (Dallimore et al., 2005).

These factors are compounded in this study by the difficulty in attaining hydrogeochemical data for the region of the study area corresponding to the potential hydrate formational zone; the geotechnical boreholes at the Bruce nuclear site are approximately 15 km from the edge of the estimated hydrate stability zone in the Upper Silurian formations. The data that is available for the Devonian stratigraphy that falls within the paleo- hydrate stability region show patterns of reduced freshening (TDS <500 mg/L) and increased heavy isotope ratios in the groundwater ($\delta^{18}O \cong -10‰$ and $\delta^{2}H \cong -80‰$) that could be indicative of hydrate dissociation (Figure **??**). However, these are much more likely reflecting the exposure of these systems to far more recent meteoric water recharge (Al et al., 2011). It is interesting to note that some of the isotope data collected from the Devonian carbonates and shales show an enrichment in $\delta^{18}O$ compared to the VSMOW meteoric water line (Figure 2.8b), which could be caused by selective incorporation of these heavier isotopic molecules into the hydrate structures (Hesse and Harrison, 1981).

The impact of these hydrates on the subsurface flow system should be examined in future work to determine whether they can account for the salinity profiles and environmental

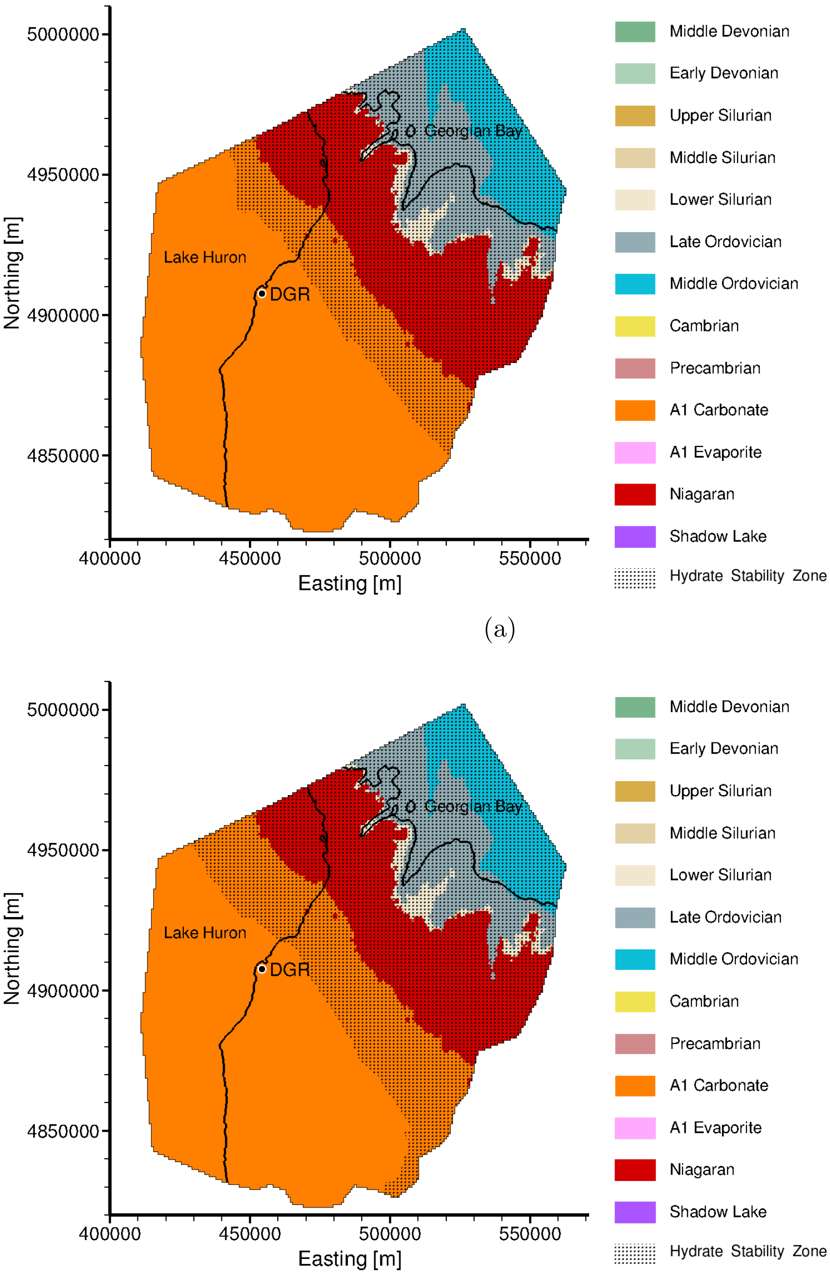

(a)

(b)

Figure 5.1: Plan view showing the extent of the potential hydrate formational zone within the Salina A1 Carbonate formation at the a) first (58.5 kaBP) and b) second (19.5 kaBP) maximum formational zone extents. Note that the potential hydrate zone (indicated by dotted area) applies only to the Salina A1 Carbonate unit and the underlying units as they subcrop to the northeast.

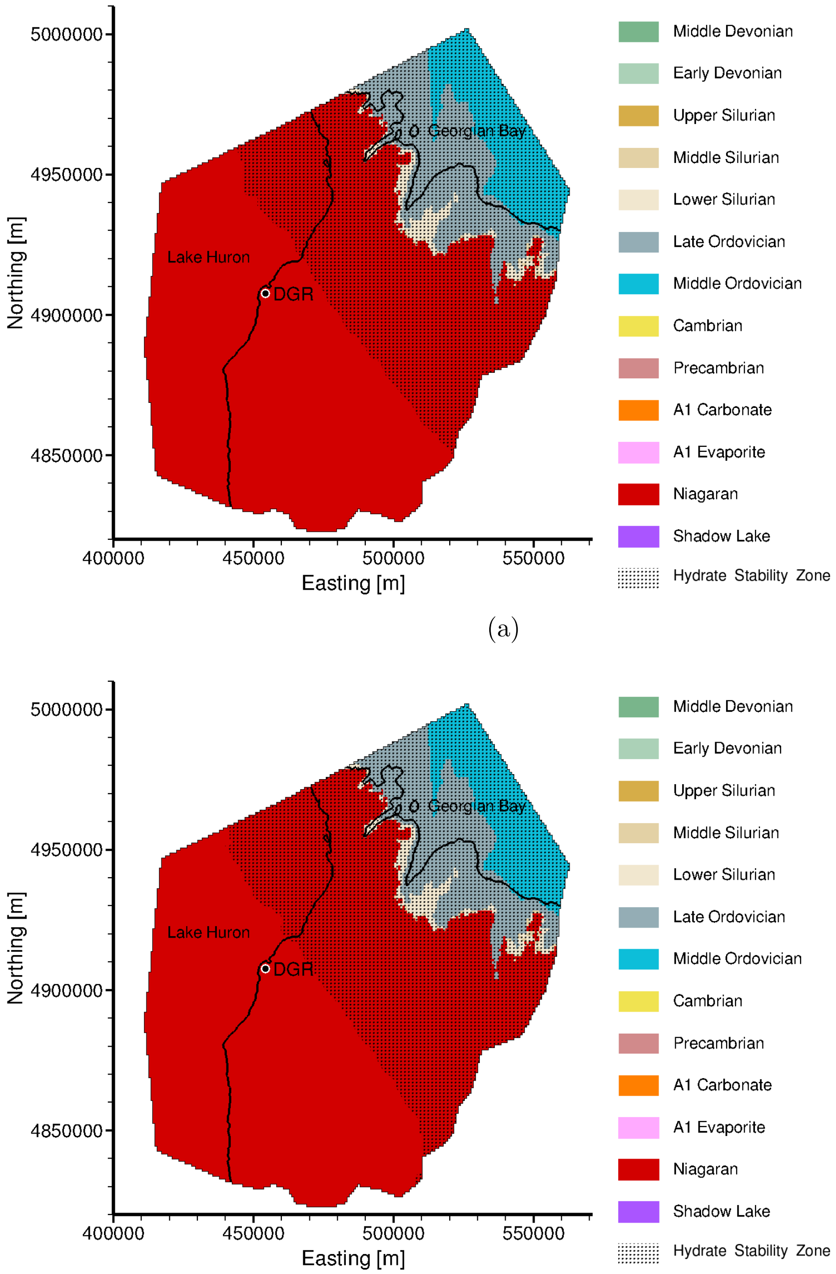

(a)

(b)

Figure 5.2: Plan view showing the extent of the potential hydrate formational zone within the Niagaran group at the a) first (58.5 kaBP) and b) second (19.5 kaBP) maximum formational zone extents. Note that the potential hydrate zone (indicated by dotted area) applies only to the Niagaran group and the underlying units as they subcrop to the northeast.

tracer distributions that are present at the study site (Section 2.2). Of particular interest would be the anomalous salinity and δ^{18}O profiles found in the Middle and Upper Silurian units. In addition, the localized freshening of the Guelph formation should be analysed in the context of hydrate-related salt exclusion in order to further support modelling work to delineate the hydrate stability zone in the study area.

5.2 Consideration of Methane Gas Availability

Since methane must be present at concentrations exceeding local saturation to facilitate hydrate growth, the delineation and quantification of methane in the subsurface is critical to accurately predict the occurrence of methane hydrates. Given the scale of the site, the period of interest, and the complexity of modelling the evolution and migration of a methane gas phase, the scope of this study was limited to identifying the solubility of methane in the sedimentary units, in order to determine the amount of methane necessary for hydrate formation. Many of the Devonian and Silurian aged units are utilized as major sources of natural oil and gas in southwestern Ontario, with the Upper Silurian pinnacle and incipient reef complexes of the Upper Silurian representing the majority of the methane gas plays in Ontario (Barker and Pollock, 1984). Northward from the major oil and gas plays of southwestern Ontario, the resources of natural gas are regarded as being limited due to the cementing of reefal pores by halite salt (Barker and Pollock, 1984). However, laboratory testing of preserved cores from DGR exploration wells at the Bruce nuclear site by Clarke et al. (2010a,b) did capture notable increases in methane concentration in the Guelph and Salina A1 carbonate units.

The same analyses by Clarke et al. (2010a,b) identified a significant presence of methane at the contact between the Middle and Upper Ordovician sequences (Figure 2.10) in excess of 0.18 mol/kg. The organic-rich shales at the base of the Blue Mountain formation are the subject of considerable natural gas resource exploration in the United States (where it is known as the Utica shale formation) (Lehmann et al., 1995) and wells within the contact aquifer where the Blue Mountain subcrops in Ontario are known to have methane gas present (Armstrong and Carter, 2010). Figure 5.3 illustrates the extent of the potential hydrate stability zone within the Late Ordovician predicted by this study; considering the observed presence of considerable quantities of methane within this unit, there is promising evidence to support the formation of hydrates towards the subcrops of the Blue Mountain formation of the Late Ordovician. Contemporary values could be used to infer concentrations during the paleo-simulations in place of modelling the multi-phase evolution of methane gas over the study period, however, such an attempt should be approached carefully, as the distribution of methane is not continuous within lithologies across the site.

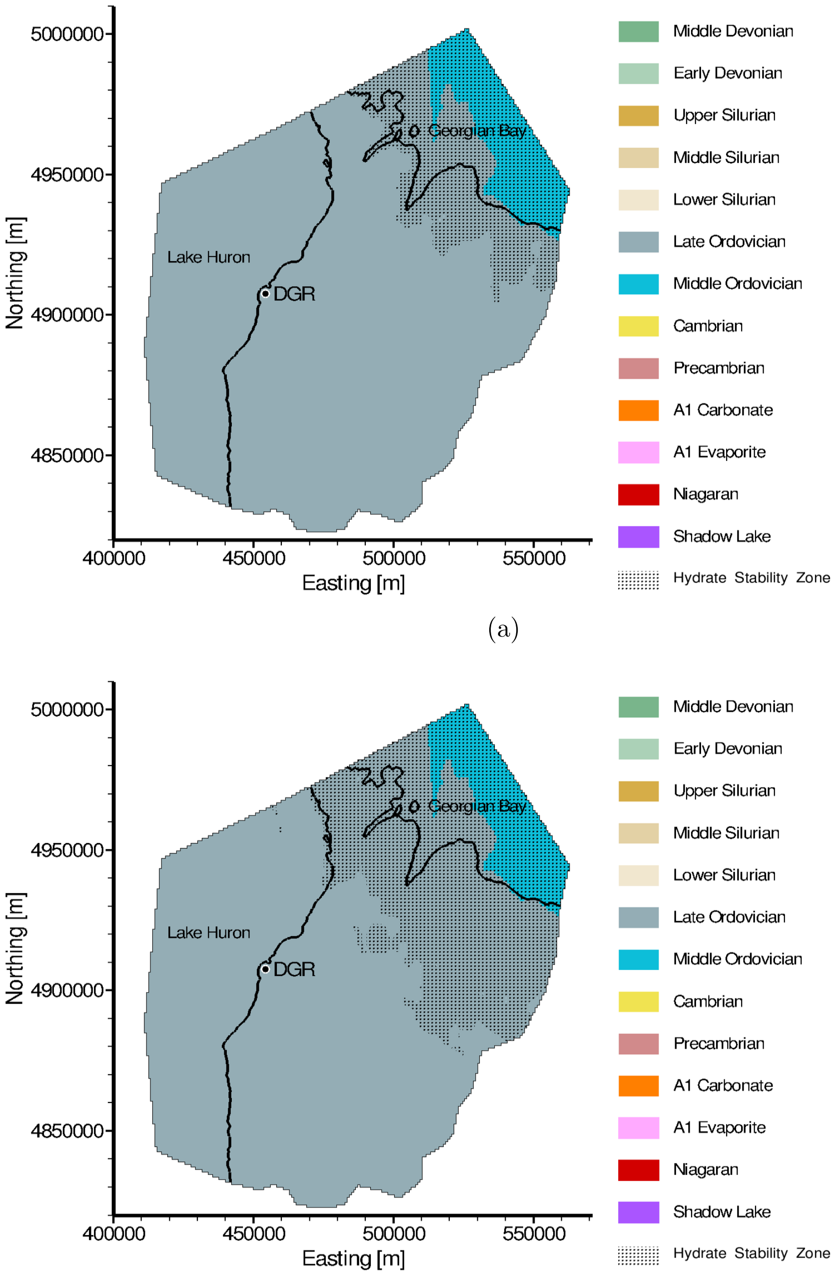

(a)

(b)

Figure 5.3: Plan view showing the extent of the potential hydrate formational zone within the Late Ordovician Blue Mountain formation at the a) first (58.5 kaBP) and b) second (19.5 kaBP) maximum formational zone extents. Note that the potential hydrate zone (indicated by dotted area) applies only to the Blue Mountain formation and the underlying units as they subcrop to the northeast.

Chapter 6

Conclusions and Recommendations

A gas hydrate refers to the specific case in which a gas molecule is entrapped by a lattice of hydrogen-bonded water molecules. Methane hydrates are found in vast quantities around the world, deposited in ocean sediments on the continental margins and terrestrial lithologies in permafrost regions. Estimates of the quantity of methane stored in the global hydrate reservoirs are highly varied, although the approximate value of 1×10^{19} g of methane carbon has been proposed by (Kvenvolden and Rogers, 2005) to represent a 'consensus estimate' of the present size of the hydrate-stored methane. To date, a number of instances of gas hydrates forming in the subsurface below layers of permafrost have been identified, while the challenge of identifying past occurrences remains relatively unmet. The impacts of global cooling and glacial advance are understood to encourage the stabilize the formation of hydrates in terrestrial polar regions as a result of the lower temperatures and the increased pressures imparted on the subsurface pressure regime (Kvenvolden, 1998). During these periods of glacial/permafrost cover, the presence of hydrates could have a significant impact on the groundwater flow system, due to the significant reduction of the porosity and permeability of hydrate saturated sediments, resulting in the obstruction of glacial melt water penetration or pore fluid efflux (Stotler et al., 2010); however, it is difficult to measure these impacts because their dissociation leaves few definitive markers as to their spatial and temporal extent.

The formation of gas hydrates is limited to the locations where (1) the required pressure and temperature conditions for a given aqueous system are such that the equilibrium point between the hydrate, liquid and free-gas phases (called three-phase equilibrium point) is reached or exceeded; and (2) where the abundance of methane is sufficient to exceed the local solubility. Thermodynamic models initially proposed by Duan and Mao (2006) and Sun and Duan (2007) are used to determine the solubility of methane gas and the conditions for methane hydrate formation across the study area, respectively. The inputs required for the thermodynamic modelling of methane solubility and methane hydrate stability were generated in this study by combining the independently-run transient three-dimensional temperature model output, with the pressure and salinity outputs from the base-case regional-scale model prepared by Sykes et al. (2011).

6.1 Conclusions

This study presented a framework employing regional-scale numerical modelling and thermodynamic predictive modelling to identify potential paleo-methane hydrate stability zones in the subsurface at the Bruce nuclear site as a first step to ultimately assessing the extent of paleo-methane hydrates and their impact. Transient subsurface conditions were modelled over a period of 120ka, encompassing episodes of glacial advance and retreat during the Pleistocene epoch. The major results of this study are as follows:

- Based upon the subsurface temperature-pressure-salinity histories determined using a three-dimensional regional-scale numerical modelling approach and a thermodynamic model for hydrate stability, subsurface paleo-conditions at the Bruce nuclear site become conducive to methane hydrate formation during the 120,000 year study period.
- Two episodes of methane hydrate stability conditions were identified at the study site – lasting from 62.5 kaBP to 56 kaBP and 23 kaBP to 13.5 kaBP – and presumably separated by periods of hydrate dissociation.
- Both of the potential hydrate formation episodes correspond to periods of substantially increased hydrostatic pressures within the shallow geologic units due to the mechanical loading of ice sheets during glacial advance across the site.
- During both episodes, potential hydrate formational zones grow from the north end of the site following the southward progression of the advancing glaciers, ultimately extending horizontally across the entire study site.
- The second of the two events of potential hydrate stability represents that larger episode both in terms of spatial extend (covering 11.3 % of the study domain) and duration (9.5 ka).

- The vertical extent of the estimated hydrate stability zone varies across the site, however it generally follows the limits of the Upper Silurian units, penetrating to deeper elevations towards the south west end of the study area. At the north east end of the study area where the sedimentary units pinch out against the Algonquin Arch, the potential hydrate formational zone extended down to the Precambrian basement.

- During the periods of glacial advance, potential hydrate formational zones were found to form across the area of the site where the sedimentary units of the Silurian and Ordovician outcrop below the ice sheets. These are generally regarded as major conduits of meltwater penetration beneath the ice sheets, in which the formation of methane hydrates would result in the constriction of rock permeability and the limiting of recharge.

- Due to the limited availability of hydrogeochemical data within the portion of the study area identified as being a potential site of paleo- hydrate formation, evaluation of the potential natural tracer evidence was not possible, and remains a goal for future research (described in section 6.2).

6.2 Recommendations for Future Work

The recommendations for future work related to the framework proposed in this study (both specific to the Bruce nuclear site, as well as the more general application of this approach to other sites with potential hydrate stability zones) can be grouped into two fields of focus: (1) the augmentation and refinement of the spatial and temporal input parameters, derived from regional-scale numerical modelling work, and (2) the expansion of the means by which hydrate stability zones are identified within the model.

Although the focus of this research was the application of the thermodynamic model to identify the occurrences of methane hydrate stability zones, the accuracy of the results depends heavily upon the ability to predict subsurface conditions throughout the glacial advances and retreats during the 120 ka study period using regional-scale numerical models. To reduce the model complexity (and closely-related computation-time), simplifying assumptions were made to allow for the development and implementation of the approach used in this study; however, given the criticality of having accurate output from the numerical modelling work, the following improvements are recommended to address the following assumptions:

- The assumption that no free-gas phase is present in the subsurface ignores the pressure buffering impact that a free-gas phase would impart during the mechanical loading of glaciers. As a result, the pressure spikes that result from these episodes of glacial cover may be overestimated. Since the results of this study indicate that these drastic increases in hydrostatic pressure caused by these glacial episodes are the initiators of the methane hydrate stability zones, further modelling should be performed to determine the sensitivity of the hydrate stability zone occurrences to the impact of free-phase gas in the subsurface.

- Coupling of the regional-scale heat flow model with the regional-scale hydraulic head and solute transport model, to allow for the penetration of cool glacial meltwaters into the subsurface. The incorporation of latent heat effects of the permafrost and rock matrix into the model should be considered. Although the results of this study seem to suggest that the episodes of hydrate formation were induced by the increase in hydrostatic pressure from the glacial loading rather than reduced temperatures, refinement of the temperature history may help to elucidate hydrate stability zones occurring at the fringes of those predicted by this study, as well as the persistence of these zones due to the thermal buffering effects of the permafrost (Taylor et al., 2005).

- While this study uses a simplified approach to handle the composition of salinity within the regional domain, by assuming all TDS is dominated by NaCl, the use of formation specific mineral compositions is accommodated by the thermodynamic model and would improve the accuracy of the study results. Present day formation water mineral compositions could be applied to the TDS profiles generated by the numerical modelling; in this way, the need for complex, multi-solute modelling may be mitigated.

The outputs generated by numerical modelling work are compiled and then processed using the thermodynamic model based on the theory by Duan and Mao (2006) to predict the location and timing of possible hydrate stability zones within the study domain. The approach taken in this study offers encouraging evidence for the occurrence of methane hydrates during glacial episodes at the Bruce nuclear site; however, even with highly accurate inputs from numerical modelling work, the ability to declare with certainty if and when hydrates have formed will remain elusive without due consideration of a number of factors that have, as yet, not been incorporated into this study. The following recommendations are made regarding future work to improve both the accuracy and certainty with which these paleo- hydrate stability zones are identified:

- Indicators such as δD depleted methane molecules (Hachikubo et al., 2007) and elevated concentrations of the C1 (methane) and C2 (ethane) gases compared to the C3+ gases have been suggested as possible signatures of methane hydrates (Milkov et al., 2004). These could be evaluated given the availability of reliable data in the predicted hydrate stability region of the study area. It should be noted that these geochemical characteristics are far from unique to hydrates and should not be considered as stand-alone qualifiers for the presence of hydrates.

- Since methane must be present at concentrations exceeding local saturation to facilitate hydrate growth, further delineation and quantification of methane in the subsurface is critical in order to accurately identify the occurrence of methane hydrates. Contemporary values could be used to infer concentrations during the paleo-simulations in place of modelling the multi-phase evolution of methane gas over the study period, which would seem impractical given the size and complexity of the study domain, and the duration of the simulation. Such an attempt would need to be approached with careful consideration given to the selection of representative data, since the distribution of methane is not continuous within lithologies across the site.

- Based on the delineation of potential hydrate formational sites provided by this study, the impact of hydrates on the subsurface flow system should be examined to determine whether they can account for TDS profiles and environmental tracer distributions that are present at the study site - specifically the anomalous salinity and δ^{18}O profile found in the Middle and Upper Silurian units. Supporting modelling work could be conducted to explore the case where the presence of hydrates results in reduced permeability, acting as a barrier to freshening of groundwater from meltwater penetration and solute transport.

- In order to better understand both the extent and impacts of the presence of paleo-hydrates in the subsurface, the use of a kinetic model is recommended (particularly for the dissociation of methane hydrates during glacial retreat) in future work to better answer the question of how long hydrates persisted in the subsurface subsequent to their formation. Although the thermodynamic model used in this study is sufficient for providing a conservative estimate of how long methane hydrates might persist, dissociation of a hydrate field will not occur spontaneously once conditions are no longer conducive to hydrate stability. While a number of studies have been conducted which propose methods for predicting dissociation rates of hydrates that could be applied to the framework implemented in this study, the effective implementation of these models is challenging due to the complexity of the multi-phase kinetics of these compounds (Sloan, 2003).

- Although the impact of porosity on the thermodynamics of methane hydrate formation was not included in this study, pore size does affect hydrate stability conditions (Dallimore et al., 2005). Future work should therefore include the addition of this component to the predictive model, which would extract porosity values from the finite element mesh along with temperature, pressure, and salinity from regional-scale numerical model output.

References

Adams, J., Bachu, S., 2002. Equations of state for basin geofluids: algorithm review and intercomparison for brines. Geofluids 2, 257–271.

Al, T., Beauheim, R., Crowe, R., Diederichs, M., Frizzell, R., Kennell, L., Lam, T., Parmenter, A., Semec, B., 2011. Opg's deep geologic repository for low and intermediate level radioactive waste: Geosynthesis report, Nuclear Waste Management Organization.

Armstrong, D., Carter, T., 2006. An updated guide to the subsurface Paleozoic stratigraphy of southern Ontario. Ontario Geological Survey, Sudbury, Canada.

Armstrong, D., Carter, T., 2010. The subsurface Paleozoic stratigraphy of southern Ontario. Ontario Geological Survey.

Armstrong, D., Dodge, J., 2007. Paleozoic geology of southern ontario. Ontario Geological Survey .

Barker, J., Pollock, S., 1984. The geochemistry and origin of natural gases in southern ontario. Bulletin of Canadian Petroleum Geology 32, 313–326.

Barton, K., Howell, D., Vigil, J., Wheeler, J., 2003. The north america tapestry of time and terrain.

Bear, J., 1988. Dynamics of fluids in porous media. Dover publications.

Beerling, D., Lomas, M., Gröcke, D., 2002. On the nature of methane gas-hydrate dissociation during the Toarcian and Aptian oceanic anoxic events. American Journal of Science 302, 28–49.

Bense, V., Person, M., 2008. Transient hydrodynamics within intercratonic sedimentary basins during glacial cycles. Journal of geophysical research 113, F04005.

Burnett, R., Frind, E., 1987. Simulation of contaminant transport in three dimensions: 2. dimensionality effects. Water Resources Research 23, 695–705.

Busey, R., 1984. Thermodynamic properties of aqueous-sodium chloride solutions. J. Phys. Chem. Ref. Data 13.

Carroll, J., 2009. Natural gas hydrates: a guide for engineers. Gulf Professional Publishing.

Chapoy, A., Mohammadi, A., Richon, D., Tohidi, B., 2004. Gas solubility measurement and modeling for methane–water and methane–ethane–*n*-butane–water systems at low temperature conditions. Fluid phase equilibria 220, 111–119.

Clarke, I., Liu, I., Mohammadzadeh, H., Zhang, P., Mohapatra, R., Wilk, M., 2010b. Pore Water and Gas Analyses in DGR-3 and DGR-4 Core. Intera Engineering Ltd. Report TR-08-19 Rev 0. Technical Report. Ottawa, Canada.

Clarke, I., Mohapatra, R., Mohammadzadeh, H., Kotzer, T., 2010a. Pore Water and Gas Analyses in DGR-1 and DGR-2 Core. Intera Engineering Ltd. Report TR-07-21 Rev 0. Technical Report. Ottawa, Canada.

Collett, T., Kvenvolden, K., Magoon, L., 1990. Characterization of hydrocarbon gas within the stratigraphic interval of gas-hydrate stability on the north slope of alaska, usa. Applied geochemistry 5, 279–287.

Collett, T., Lewis, R., Dallimore, S., 2005. Japex/jnoc/gsc et al. mallik 5l-38 gas hydrate production research well downhole well-log and core montages. Bulletin-Geological Survey of Canada 585, 111.

Collett, T., Lewis, R., Winters, W., Lee, M., Rose, K., Boswell, R., 2011. Downhole well log and core montages from the mount elbert gas hydrate stratigraphic test well, alaska north slope. Marine and Petroleum Geology 28, 561–577.

Culberson, O., Horn, A., Mc Ketta Jr, J., 1950. Phase equilibria in hydrocarbon-water systems: the solubility of ethane in water at pressures up to 1200 pounds per square inch. Trans. Am. Inst. Min. Met. Eng 189, 1–6.

Dallimore, S., et al., 2005. Scientific results from the Mallik 2002 gas hydrate production research well program, Mackenzie Delta, Northwest Territories, Canada. Geological Survey of Canada.

De Roo, J., Peters, C., Lichtenthaler, R., Diepen, G., 1983. Occurrence of methane hydrate in saturated and unsaturated solutions of sodium chloride and water in dependence of temperature and pressure. AIChE Journal 29, 651–657.

Denbigh, K., Denbigh, K., 1981. The principles of chemical equilibrium: with applications in chemistry and chemical engineering. Cambridge Univ Pr.

Dickens, G., ONeil, J., Rea, D., Owen, R., 1995. Dissociation of oceanic methane hydrate as a cause of the carbon isotope excursion at the end of the. Paleocene Paleoceanogr 10, 965–971.

Dickens, G.R., 2003. Rethinking the global carbon cycle with a large, dynamic and microbially mediated gas hydrate capacitor. Earth and Planetary Science Letters 213, 169–183.

Duan, Z., Mao, S., 2006. A thermodynamic model for calculating methane solubility, density and gas phase composition of methane-bearing aqueous fluids from 273 to 523°K and from 1 to 2000 bar. Geochimica et Cosmochimica Acta 70, 3369–3386.

Duan, Z., Moller, N., Weare, J., 1992. An equation of state for the CH4-CO2-H2O system: I. Pure systems from 0 to 1000°C and 0 to 8000 bar. Geochimica et Cosmochimica Acta 56, 2605–2617.

Dubessy, J., Thiery, R., Canals, M., 1992a. Modelling of phase equilibria involving mixed gas clathrates: application to the determination of molar volume of the vapour phase and salinity of the aqueous solution in fluid inclusions. European journal of mineralogy 4, 873–884.

Ethier, A., Clark, I., Dallimore, S., Matsumoto, R., Middlestead, P., 2005. High-resolution isotope geochemistry of the gas hydrate-free gas transition in the japex/jnoc/gsc et al. mallik 5l-38 gas hydrate production research well. Bulletin-Geological Survey of Canada 585, 100.

Everham, W.D., Huntoon, J.E., 1999. Thermal history of a deep well in the michigan basin: Implications for a complex burial history , 177–202.

Freeze, R., Cherry, J., 1979. Groundwater, 604 pp. PrenticeHall, Englewood Cliffs, NJ .

Frind, E., 1982. Simulation of long-term transient density-dependent transport in groundwater. Advances in Water Resources 5, 73–88.

Grace, J., Collett, T., Colwell, F., Englezos, P., Jones, E., Mansell, R., Meekison, J., Ommer, R., Pooladi-Darvish, M., Riedel, M., et al., 2008. Energy from gas hydrates: Assessing the opportunities & challenges for canada. Report of the Expert Panel on Gas Hydrates, Council of Canadian Academies .

Guvanasen, V., 2007. FRAC3DVS-OPG enhancements: subgridding, hydromechanical deformation and anisotropic molecular diffusion. Nuclear Waste Management Organization Report NWMO-TR-2007-05 .

Hachikubo, A., Kosaka, T., Kida, M., Krylov, A., Sakagami, H., Minami, H., Takahashi, N., Shoji, H., 2007. Isotopic fractionation of methane and ethane hydrates between gas and hydrate phases. Geophysical Research Letters 34, L21502.

Handa, Y., 1990. Effect of hydrostatic pressure and salinity on the stability of gas hydrates. Journal of Physical Chemistry 94, 2652–2657.

Hesse, R., Harrison, W., 1981. Gas hydrates (clathrates) causing pore-water freshening and oxygen isotope fractionation in deep-water sedimentary sections of terrigenous continental margins. Earth and Planetary Science Letters 55, 453–462.

Hesselbo, S., Gröcke, D., Jenkyns, H., Bjerrum, C., Farrimond, P., Bell, H., Green, O., 2000. Massive dissociation of gas hydrate during a jurassic oceanic anoxic event. Nature 406, 392–395.

Hobbs, M., Frape, S., Shouakar-Stash, O., Kennell, L., 2011. Regional hydrogeochemistry–southern ontario. Nuclear Waste Management Organization Report NWMO DGR-TR-2011-12 R .

Holder, G., Corbin, G., Papadopoulos, K., 1980. Thermodynamic and molecular properties of gas hydrates from mixtures containing methane, argon, and krypton. Industrial & Engineering Chemistry Fundamentals 19, 282–286.

Hunter, R., Collett, T., Boswell, R., Anderson, B., Digert, S., Pospisil, G., Baker, R., Weeks, M., 2011. Mount elbert gas hydrate stratigraphic test well, alaska north slope: Overview of scientific and technical program. Marine and Petroleum Geology 28, 295–310.

INTERA, 2011. Descriptive Geosphere Site Model. Technical Report. Intera Engineering Ltd. report for the Nuclear Waste Management Organization NWMO DGR-TR-2011-24 R000. Toronto, Canada.

ITASCA Canada and AECOM, 2011. Three-Dimensional Geological Framework Model. Technical Report. Itasca Consulting Canada, Inc. and AECOM Canada Ltd. report for the Nuclear Waste Management Organization, NWMO DGR-TR-2011-42 R000.. Toronto, Canada.

Jaeger, J., Cook, N., Zimmerman, R., 2007. Fundamentals of rock mechanics. Wiley-Blackwell.

Jager, M., Sloan, E., 2001. The effect of pressure on methane hydration in pure water and sodium chloride solutions. Fluid Phase Equilibria 185, 89–99.

Johnson, M., Armstrong, D., Sanford, B., Telford, P., Rutka, M., 1992. Paleozoic and mesozoic geology of ontario. Geology of Ontario, Ontario Geological Survey, Special 4, 907–1008.

Van der Kamp, G., Gale, J., 1983. Theory of earth tide and barometric effects in porous formations with compressible grains. Water Resources Research 19, 538–544.

Kharrat, M., Dalmazzone, D., 2003. Experimental determination of stability conditions of methane hydrate in aqueous calcium chloride solutions using high pressure differential scanning calorimetry. The Journal of Chemical Thermodynamics 35, 1489–1505.

Kvenvolden, K., 1988. Methane hydrate–a major reservoir of carbon in the shallow geosphere? Chemical Geology 71, 41–51.

Kvenvolden, K., 1998. A primer on the geological occurrence of gas hydrate. Geological Society, London, Special Publications 137, 9–30.

Kvenvolden, K., Claypool, G., 1988. Gas hydrates in oceanic sediment. Department of the Interior, US Geological Survey.

Kvenvolden, K., Rogers, B., 2005. Gaia's breathglobal methane exhalations. Marine and Petroleum Geology 22, 579–590.

Lehmann, D., Brett, C.E., Cole, R., Baird, G., 1995. Distal sedimentation in a peripheral foreland basin: Ordovician black shales and associated flysch of the western taconic foreland, new york state and ontario. Geological Society of America Bulletin 107, 708–724.

Lemieux, J.M., Sudicky, E.A., 2010. Simulation of groundwater age evolution during the wisconsinian glaciation over the canadian landscape. Environmental fluid mechanics 10, 91–102.

Lorenson, T., Whiticar, M., Collett, T., Dallimore, S., Dougherty, J., 2005. Complete gas composition and isotopic geochemistry from the japex/jnoc/gsc et al. mallik 5l-38 gas hydrate production research well: cuttings, core, gas hydrate, and production testing results. Bulletin-Geological Survey of Canada 585, 94.

MacDonald, G., 1990. The future of methane as an energy resource. Annual Review of Energy 15, 53–83.

Matsumoto, R., 2006. Methane hydrate estimates from the chloride and oxygen isotopic anomalies: Examples from the blake ridge and nankai trough sediments. Annals of the New york Academy of Sciences 912, 39–50.

Matsumoto, R., Borowski, W., 2000. Gas hydrate estimates from newly determined oxygen isotopic fractionation (αgh-iw) and δ18o anomalies of the interstitial waters: Leg 164, blake ridge, in: Proceedings of the Ocean Drilling Program, Scientific Results.

Matsumoto, R., Tomaru, H., Chen, Y., Lu, H., Clark, I., 2005. Geochemistry of the interstitial waters of the japex/jnoc/gsc/et al. mallik 5l-38 gas hydrate research well. Bulletin of Geological Survey of Canada 585, 98–98.

McCollom, T.M., Seewald, J.S., 2013. Serpentinites, hydrogen, and life. Elements 9, 129–134.

McIntosh, J., Garven, G., Hanor, J., 2010. Impacts of pleistocene glaciation on large-scale groundwater flow and salinity in the michigan basin. Geofluids .

McIntosh, J., Walter, L., 2006. Paleowaters in silurian-devonian carbonate aquifers: geochemical evolution of groundwater in the great lakes region since the late pleistocene. Geochimica et cosmochimica acta 70, 2454–2479.

McIver, R., 1981. Gas hydrates. Long-term energy resources. Boston: Pitman , 713–26.

McIver, R.D., 1982. Role of naturally occurring gas hydrates in sediment transport. AAPG Bulletin 66, 789–792.

Meyer, R., 1981. Speculations on oil and gas resources in small fields and unconventional deposits. Long-term energy resources. Boston: Pitman , 49–72.

Milkov, A., Claypool, G., Lee, Y., Torres, M., Borowski, W., Tomaru, H., Sassen, R., Long, P., Leg, O., 2004. Ethane enrichment and propane depletion in subsurface gases indicate gas hydrate occurrence in marine sediments at southern hydrate ridge offshore oregon. Organic Geochemistry 35, 1067–1080.

Munck, J., Skjold-Jorgensen, S., Rasmussen, P., 1988. Computations of the formation of gas hydrates. Chemical engineering science 43, 2661–2672.

Neuzil, C., 2003. Hydromechanical coupling in geologic processes. Hydrogeology Journal 11, 41–83.

Normani, S., 2010. Paleoevolution of pore fluids in glaciated geologic settings. Ph.D. thesis. University of Waterloo.

O'Sullivan, T., Smith, N., 1970. Solubility and partial molar volume of nitrogen and methane in water and in aqueous sodium chloride from 50 to 125 deg. and 100 to 600 atm. The Journal of Physical Chemistry 74, 1460–1466.

Parrish, W., Prausnitz, J., 1972. Dissociation pressures of gas hydrates formed by gas mixtures. Industrial & Engineering Chemistry Process Design and Development 11, 26–35.

Paull, C., Matsumoto, R., Wallace, P., , et al., 1996. Proceedings of the ocean drilling program, vol. 164, initial reports, gas hydrate sampling on the blake ridge and carolina rise, Ocean Drilling Program.

Peltier, W., 2011. Long-term climate change. Nuclear Waste Management Organization Report Nuclear Waste Management Organization DGR-TR-2011-14 R .

Pitzer, K., 1991. Ion interaction approach: Theory and data correlation. Activity coefficients in electrolyte solutions 2, 75–153.

Pitzer, K., Mayorga, G., 1973. Thermodynamics of electrolytes. II. Activity and osmotic coefficients for strong electrolytes with one or both ions univalent. The Journal of Physical Chemistry 77, 2300–2308.

Ruppel, C., 2007. Tapping methane hydrates for unconventional natural gas. Elements 3, 193–199.

Schoell, M., 1988. Multiple origins of methane in the earth. Chemical Geology 71, 1–10.

Shibue, Y., 2003. Vapor pressures of aqueous NaCl and CaCl2 solutions at elevated temperatures. Fluid phase equilibria 213, 39–51.

Sloan, E., 2003. Fundamental principles and applications of natural gas hydrates. Nature 426, 353–363.

Sloan Jr, E., Koh, C., 2007. Clathrate hydrates of natural gases. CRC.

Spencer, R., Moller, N., Weare, J., 1990. The prediction of mineral solubilities in natural waters: A chemical equilibrium model for the Na—K—Ca—Mg—Cl—SO4—H2O system at temperatures below 25°C. Geochimica et Cosmochimica Acta 54, 575–590.

Stotler, R., Frape, S., Ahonen, L., Clark, I., Greene, S., Hobbs, M., Johnson, E., Lemieux, J., Peltier, R., Pratt, L., et al., 2010. Origin and stability of a permafrost methane hydrate occurrence in the canadian shield. Earth and Planetary Science Letters 296, 384–394.

Sun, R., Duan, Z., 2005. Prediction of CH4 and CO2 hydrate phase equilibrium and cage occupancy from ab initio intermolecular potentials. Geochimica et cosmochimica acta 69, 4411–4424.

Sun, R., Duan, Z., 2007. An accurate model to predict the thermodynamic stability of methane hydrate and methane solubility in marine environments. Chemical geology 244, 248–262.

Sykes, J., Normani, S., Yin, Y., 2011. Hydrogeologic modelling, Technical Report NWMO DGR-TR-2011-16 R000. Technical Report. Nuclear Waste Management Organization. Toronto, Canada.

Taylor, A., Dallimore, S., Hyndman, R., Wright, F., 2005. Comparing the sensitivity of permafrost and marine gas hydrate to climate warming. Bulletin-Geological Survey of Canada 585, 130.

Tester, J., Trout, B., Cao, Z., et al., 2002. Modeling of gas hydrates from first principles. Ph.D. thesis. Massachusetts Institute of Technology.

Therrien, R., Sudicky, E., McLaren, R., 2003. FRAC3DVS: an efficient simulator for three-dimensional, saturated-unsaturated groundwater flow and density dependent, chain-decay solute transport in porous, discretely-fractured porous or dual-porosity formations. Users guide , 146.

Tomaru, H., Matsumoto, R., Chen, Y., Lu, H., Clark, I., 2005. Evolution of a gas hydrate system as recorded by oxygen and hydrogen isotopes of the interstitial waters of the japex/jnoc/gsc et al. mallik 5l-38 gas hydrate production research well. Bulletin-Geological Survey of Canada 585, 99.

Torres, M., Collett, T., Rose, K., Sample, J., Agena, W., Rosenbaum, E., 2011. Pore fluid geochemistry from the mount elbert gas hydrate stratigraphic test well, alaska north slope. Marine and Petroleum Geology 28, 332–342.

Waals, J., Platteeuw, J., 1959. Clathrate solutions. Advances in Chemical Physics , 1–57.

Wagner, W., Pruss, A., 1993. International Equations for the Saturation Properties of Ordinary Water Substance: Revised According to the International Temperature Scale of 1990. American Chemical Society.

Waples, D., Waples, J., 2004. A review and evaluation of specific heat capacities of rocks, minerals, and subsurface fluids. part 1: Minerals and nonporous rocks. Natural resources research 13, 97–122.

Weast, R.E., 1983. Crc handbook of chemistry and physics. 64th edition. CRC Press Inc., Boca Raton, Florida, USA .

Welhan, J., 1988. Origins of methane in hydrothermal systems. Chemical Geology 71, 183–198.

Whiticar, M., 1999. Carbon and hydrogen isotope systematics of bacterial formation and oxidation of methane. Chemical Geology 161, 291–314.

Winters, W., Dallimore, S., Collett, T., Jenner, K., Katsube, J., Cranston, R., Wright, J., Nixon, F., Uchida, T., 2006. Relation between gas hydrate and physical properties at the mallik 2l-38 research well in the mackenzie delta. Annals of the New York Academy of Sciences 912, 94–100.

Winters, W., Walker, M., Hunter, R., Collett, T., Boswell, R., Rose, K., Waite, W., Torres, M., Patil, S., Dandekar, A., 2011. Physical properties of sediment from the mount elbert gas hydrate stratigraphic test well, alaska north slope. Marine and Petroleum Geology 28, 361–380.

Yakushev, V., Chuvilin, E., 2000. Natural gas and gas hydrate accumulations within permafrost in russia. Cold Regions Science and Technology 31, 189–197.

Ziegler, K., Longstaffe, F., 2000. Multiple episodes of clay alteration at the precambrian/paleozoic unconformity, appalachian basin: isotopic evidence for long-distance and local fluid migrations. Clays and clay minerals 48, 474–493.

APPENDICES

Appendix A

Regional-Scale Model Parameters for Groundwater Flow, Solute Transport and Temperature

Table A.1: Summary of Groundwater Flow Parameters for Formations of the Regional-scale Numerical Model. Modified from Sykes et al. (2011).

Formation	K_H (m/s)	K_V (m/s)	S_s (m^{-1})	θ_s	ζ_s	τ
Drift	1.0x10^{-8}	5.0x10^{-9}	9.9x10^{-5}	0.200	0.99	4.0x10^{-1}
Hamilton Group	2.2x10^{-11}	2.2x10^{-12}	1.5x10^{-6}	0.100	0.80	1.2x10^{-1}
Dundee	8.4x10^{-8}	8.4x10^{-9}	1.5x10^{-6}	0.100	0.80	1.2x10^{-1}
Detroit River Group	5.9x10^{-7}	2.0x10^{-8}	1.4x10^{-6}	0.077	0.84	9.4x10^{-2}
Bois Blanc	1.0x10^{-7}	1.0x10^{-8}	1.4x10^{-6}	0.077	0.84	9.4x10^{-2}
Bass Islands	5.0x10^{-5}	1.7x10^{-6}	2.0x10^{-6}	0.056	0.92	2.8x10^{-1}
Unit G	1.0x10^{-11}	1.0x10^{-12}	1.1x10^{-6}	0.172	0.55	3.0x10^{-3}
Unit F	5.0x10^{-14}	5.0x10^{-15}	9.5x10^{-7}	0.100	0.68	4.9x10^{-2}
Unit F Salt	5.0x10^{-14}	5.0x10^{-15}	9.5x10^{-7}	0.100	0.68	4.9x10^{-2}
Unit E	2.0x10^{-13}	2.0x10^{-14}	6.5x10^{-7}	0.100	0.51	5.7x10^{-2}
Unit D	2.0x10^{-13}	2.0x10^{-14}	6.4x10^{-7}	0.089	0.53	6.4x10^{-2}
Units B and C	4.0x10^{-13}	4.0x10^{-14}	9.5x10^{-7}	0.165	0.38	8.4x10^{-2}
Unit B Anhydrite	3.0x10^{-13}	3.0x10^{-14}	6.9x10^{-7}	0.089	0.53	1.0x10^{-3}
Unit A2 Carbonate	3.0x10^{-10}	3.0x10^{-11}	7.2x10^{-7}	0.120	0.46	1.2x10^{-2}
Unit A2 Evaporite	3.0x10^{-13}	3.0x10^{-14}	5.8x10^{-7}	0.089	0.53	1.0x10^{-3}
Unit A1 Carbonate	9.0x10^{-12}	5.0x10^{-13}	4.1x10^{-7}	0.007	0.84	1.0x10^{-2}
Unit A1 Evaporite	3.0x10^{-13}	5.0x10^{-14}	3.9x10^{-7}	0.032	0.94	5.2x10^{-3}
Niagaran Group	3.6x10^{-9}	2.5x10^{-13}	2.7x10^{-7}	0.026	0.66	1.2x10^{-2}
Reynales / Fossol Hill	5.0x10^{-12}	5.0x10^{-13}	2.9x10^{-7}	0.031	0.62	6.2x10^{-1}
Cabot Head	9.0x10^{-14}	5.0x10^{-15}	1.1x10^{-6}	0116	0.60	3.2x10^{-2}
Manitoulin	9.0x10^{-14}	9.0x10^{-15}	7.5x10^{-7}	0.028	0.86	6.4x10^{-3}
Queenston	2.0x10^{-14}	2.0x10^{-15}	9.0x10^{-7}	0.073	0.71	1.6x10^{-2}
Georgian Bay / Blue Mtn.	3.6x10^{-14}	3.3x10^{-15}	1.2x10^{-6}	0.070	0.79	8.8x10^{-3}
Cobourg	2.0x10^{-14}	2.0x10^{-15}	2.6x10^{-7}	0.015	0.80	3.0x10^{-2}
Sherman Fall	1.0x10^{-14}	1.0x10^{-15}	4.9x10^{-7}	0.016	0.88	1.7x10^{-2}
Kirkfield	8.0x10^{-15}	8.0x10^{-16}	4.9x10^{-7}	0.021	0.85	2.4x10^{-2}
Coboconk	4.0x10^{-12}	4.0x10^{-15}	4.6x10^{-7}	0.009	0.93	3.6x10^{-2}
Gull River	7.0x10^{-13}	7.0x10^{-16}	4.9x10^{-7}	0.022	0.85	1.4x10^{-2}
Shadow Lake	1.0x10^{-9}	1.0x10^{-12}	7.4x10^{-7}	0.097	0.56	7.6x10^{-2}
Cambrian	3.0x10^{-6}	3.0x10^{-6}	3.7x10^{-7}	0.071	0.34	1.3x10^{-1}
Upper Precambrian	1.0x10^{-10}	1.0x10^{-10}	2.6x10^{-7}	0.038	0.49	9.5x10^{-3}
Precambrian	1.0x10^{-12}	1.0x10^{-12}	1.5x10^{-7}	0.005	0.88	7.2x10^{-2}

Table A.2: Summary of Solute Transport Parameters for the Regional-scale Numerical Model. Modified from Sykes et al. (2011).

Formation	θ_s	τ	ρ (kg/m^3)	TDS (g/L)	D_e (m^2/s)[a]
Drift	0.200	4.0x10^{-1}	1,000	0.0	1.484x10^{-9}
Hamilton Group	1,008	1.2x10^{-1}	12.0	0.80	1.484x10^{-9}
Dundee	0.100	1.2x10^{-1}	1,005	8.0	1.484x10^{-9}
Detroit River Group	0.077	9.4x10^{-2}	1,001	1.4	1.484x10^{-9}
Bois Blanc	0.077	9.4x10^{-2}	1,002	3.2	1.484x10^{-9}
Bass Islands	0.056	2.8x10^{-1}	1,004	6.0	1.484x10^{-9}
Unit G	0.172	3.0x10^{-3}	1,010	14.8	1.484x10^{-9}
Unit F	0.100	4.9x10^{-2}	1,040	59.6	1.484x10^{-9}
Unit F Salt	0.100	4.9x10^{-2}	1,040	59.6	1.484x10^{-9}
Unit E	0.100	5.7x10^{-2}	1,083	124.0	1.484x10^{-9}
Unit D	0.089	6.4x10^{-2}	1,133	200.0	1.484x10^{-9}
Units B and C	0.165	8.4x10^{-2}	1,198	296.7	1.484x10^{-9}
Unit B Anhydrite	0.089	1.0x10^{-3}	1,214	321.0	1.484x10^{-9}
Unit A2 Carbonate	0.120	1.2x10^{-2}	1,091	136.0	1.484x10^{-9}
Unit A2 Evaporite	0.089	1.0x10^{-3}	1,030	45.6	1.484x10^{-9}
Unit A1 Carbonate	0.007	1.0x10^{-2}	1,120	180.2	1.484x10^{-9}
Unit A1 Evaporite	0.032	5.2x10^{-3}	1,229	343.7	1.484x10^{-9}
Niagaran Group	0.026	1.2x10^{-2}	1,206	308.4	1.484x10^{-9}
Reynales / Fossol Hill	0.031	6.2x10^{-1}	1,200	300.0	1.484x10^{-9}
Cabot Head	0116	3.2x10^{-2}	1,204	306.0	1.484x10^{-9}
Manitoulin	0.028	6.4x10^{-3}	1,233	350.0	1.484x10^{-9}
Queenston	0.073	1.6x10^{-2}	1,207	310.0	1.484x10^{-9}
Georgian Bay / Blue Mtn.	0.070	8.8x10^{-3}	1,200	299.4	1.484x10^{-9}
Cobourg	0.015	3.0x10^{-2}	1,181	272.0	1.484x10^{-9}
Sherman Fall	0.016	1.7x10^{-2}	1,180	270.0	1.484x10^{-9}
Kirkfield	0.021	2.4x10^{-2}	1,156	234.0	1.484x10^{-9}
Coboconk	0.009	3.6x10^{-2}	1,170	255.0	1.484x10^{-9}
Gull River	0.022	1.4x10^{-2}	1,135	203.0	1.484x10^{-9}
Shadow Lake	0.097	7.6x10^{-2}	1,133	200.0	1.484x10^{-9}
Cambrian	0.071	1.3x10^{-1}	1,157	235.0	1.484x10^{-9}
Upper Precambrian	0.038	9.5x10^{-3}	1,200	300.0	1.484x10^{-9}
Precambrian	0.005	7.2x10^{-2}	1,200	300.0	1.484x10^{-9}

[a] Brine effective diffusion coefficient for TDS transport modelling assumed to be NaCl at 1 mol/L (Weast, 1983).

Table A.3: Parameters for Equation 3.16

Formation	Lithology	ρ (g/cm^3)[b]	k (W/mK)	c_p $(J/kg/K)$[b]
Drift	Drift	2.00	2.00[c]	1100
Hamilton Group	Shale	2.35	2.23[a]	800
Dundee	Carbonate	2.80	2.98[a]	800
Detroit River Group	Dolostone/Limestone	2.77	2.98[a]	840
Bois Blanc	Dolostone	2.80	2.98[a]	900
Bass Islands	Dolostone	2.80	3.62[a]	900
Unit G	Evaporite/Shale	2.20	4.50[c]	780
Unit F	Shale	2.35	1.50[c]	800
Unit F Salt	Evaporite/Shale	2.20	4.50[c]	780
Unit E	Shale/Carbonate	2.80	1.50[c]	800
Unit D	Evaporite/Carbonate	2.80	4.50[c]	800
Units B and C	Shale	2.35	1.50[c]	800
Unit B Anhydrite	Evaporite	2.16	4.50[c]	765
Unit A2 Carbonate	Carbonate	2.80	2.50[c]	800
Unit A2 Evaporite	Evaporite	2.16	4.50[c]	765
Unit A1 Carbonate	Carbonate	2.80	2.50[c]	800
Unit A1 Evaporite	Evaporite	2.16	4.50[c]	765
Niagaran Group	Dolostone	2.80	2.57[a]	900
Reynales / Fossol Hill	Dolostone	2.80	2.57[a]	900
Cabot Head	Shale	2.35	1.50[c]	800
Manitoulin	Dolostone	2.80	2.57[a]	900
Queenston	Shale	2.35	1.50[c]	800
Georgian Bay / Blue Mtn.	Shale	2.35	1.50[c]	800
Cobourg	Limestone	2.77	2.50[c]	780
Sherman Fall	Limestone	2.77	2.50[c]	780
Kirkfield	Limestone	2.77	2.50[c]	780
Coboconk	Limestone	2.77	2.50[c]	780
Gull River	Limestone	2.77	2.50[c]	780
Shadow Lake	Shale	2.35	1.50[c]	800
Cambrian	Dolostone	2.80	2.50[c]	900
Upper Precambrian	Granitic Gneiss	2.70	2.50[c]	880
Precambrian	Granitic Gneiss	2.70	2.50[c]	880

Note: Parameter values provided by [a] Everham and Huntoon (1999), [b] Waples and Waples (2004) and [c] McIntosh et al. (2010)

Appendix B

Fence and Block-Cut Diagrams of Regional-Scale Modelling Results

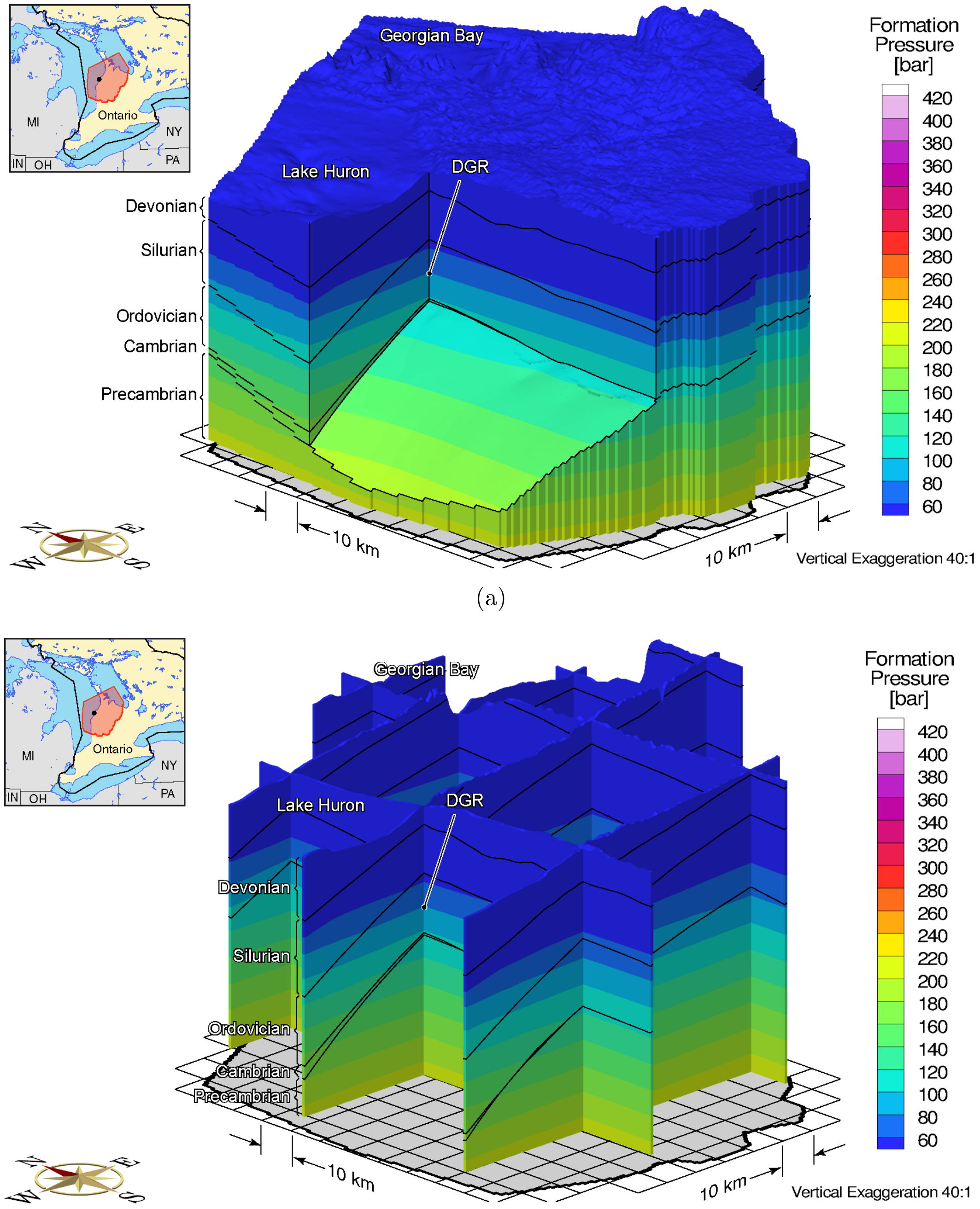

(a)

(b)

Figure B.1: Initial pressure distribution across the regional-scale model domain, presented using a) block-cut and b) fence diagrams

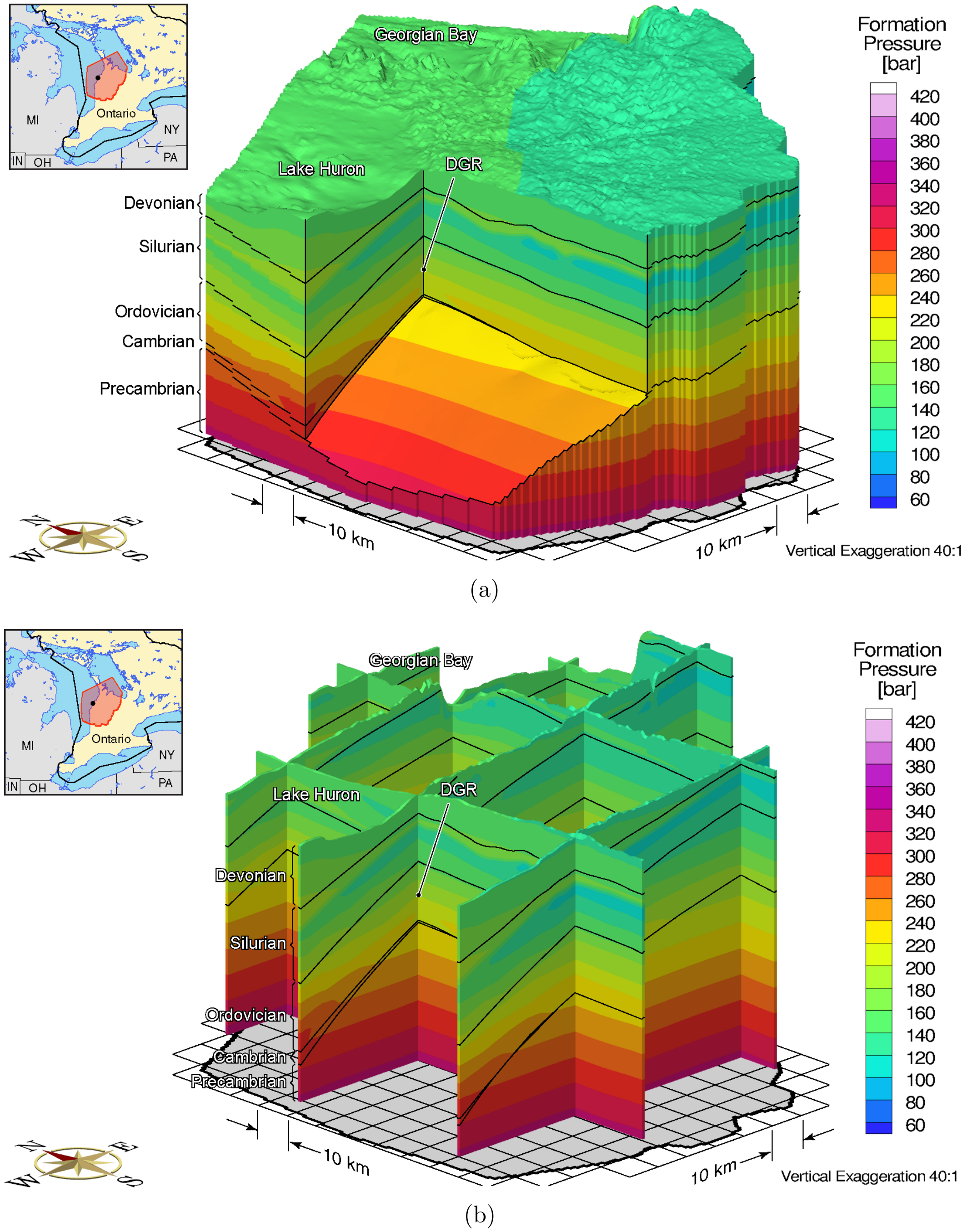

Figure B.2: Pressure distribution across the regional-scale model domain at 58 ka before present, presented using a) block-cut and b) fence diagrams

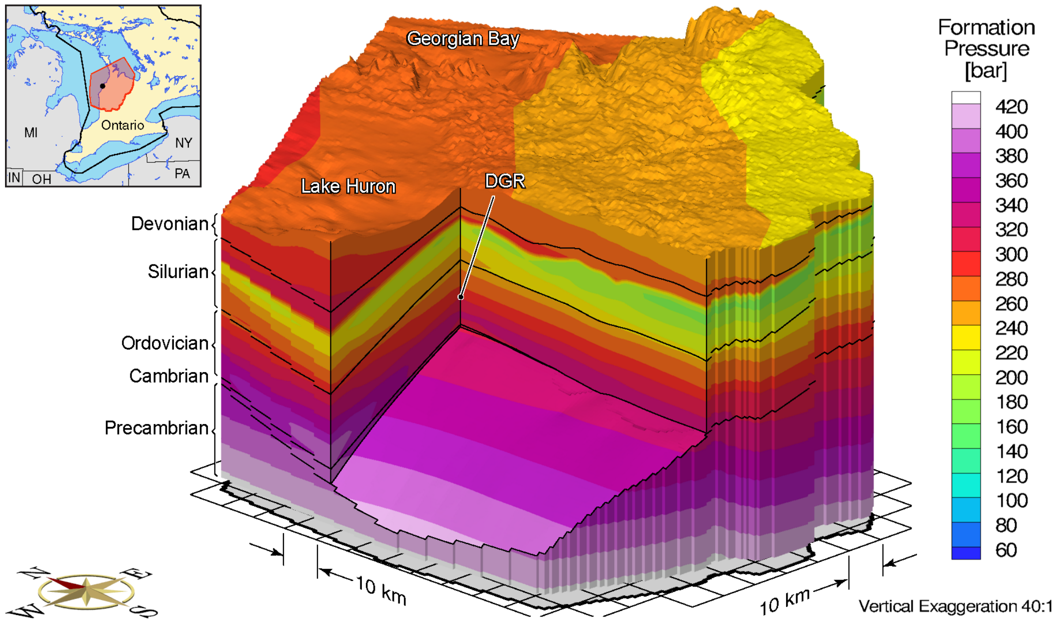

(a)

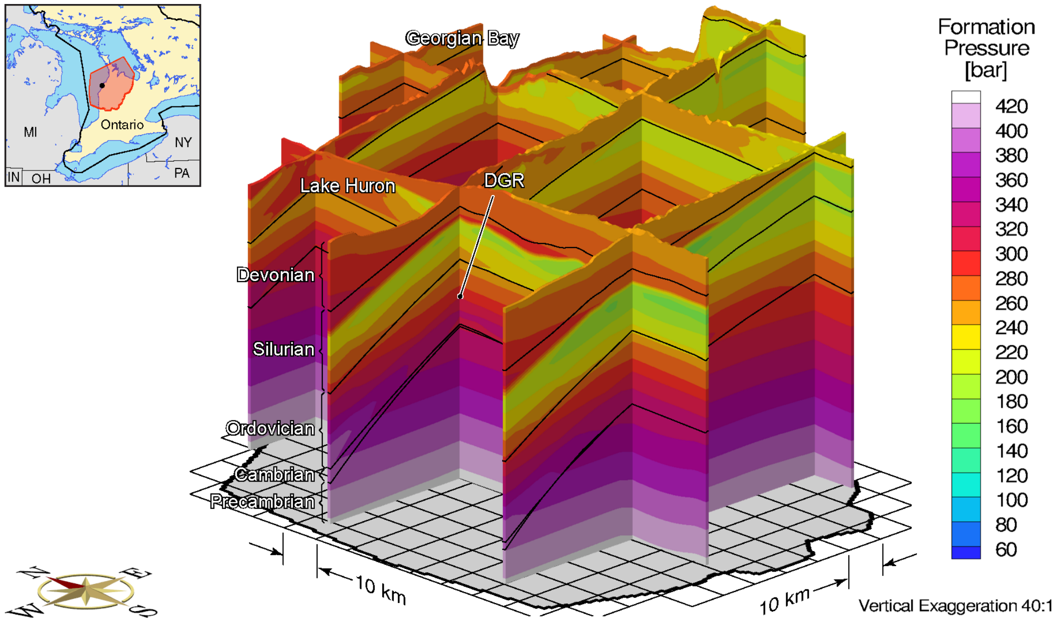

(b)

Figure B.3: Pressure distribution across the regional-scale model domain at 19.5 ka before present, presented using a) block-cut and b) fence diagrams

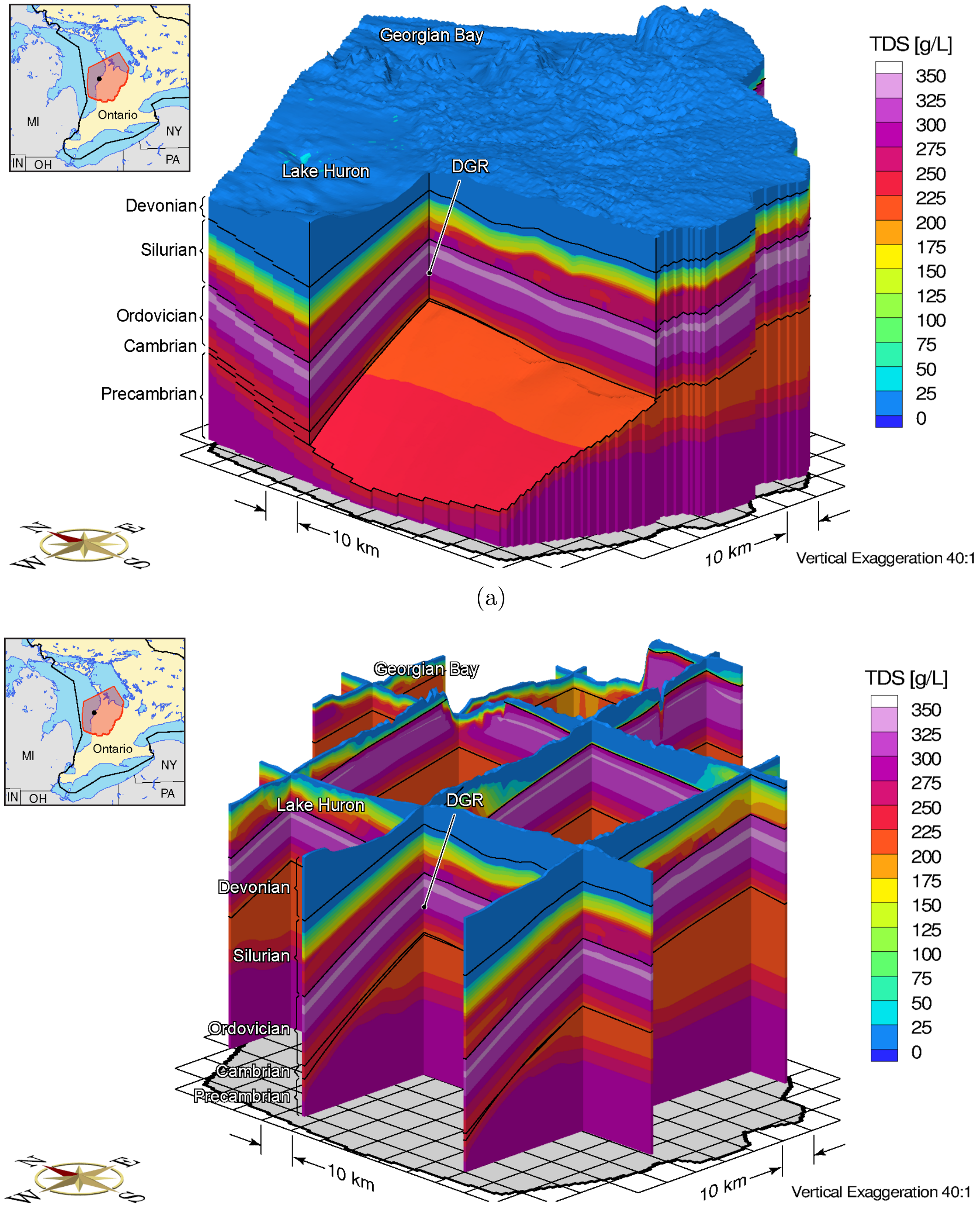

(a)

(b)

Figure B.4: Initial salinity (TDS) distribution across the regional-scale model domain, presented using a) block-cut and b) fence diagrams

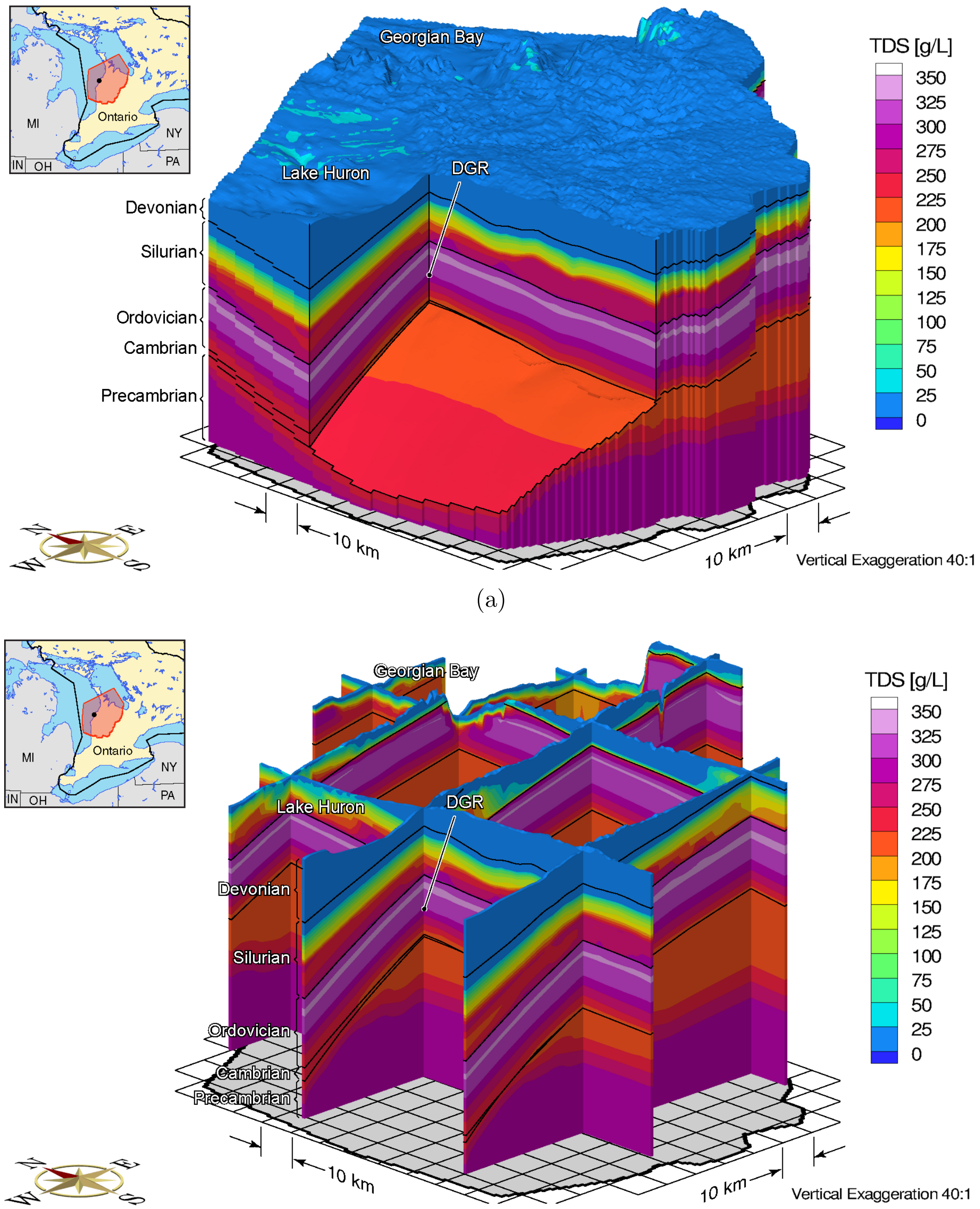

(a)

(b)

Figure B.5: Salinity (TDS) distribution across the regional-scale model domain at 58 ka before present, presented using a) block-cut and b) fence diagrams

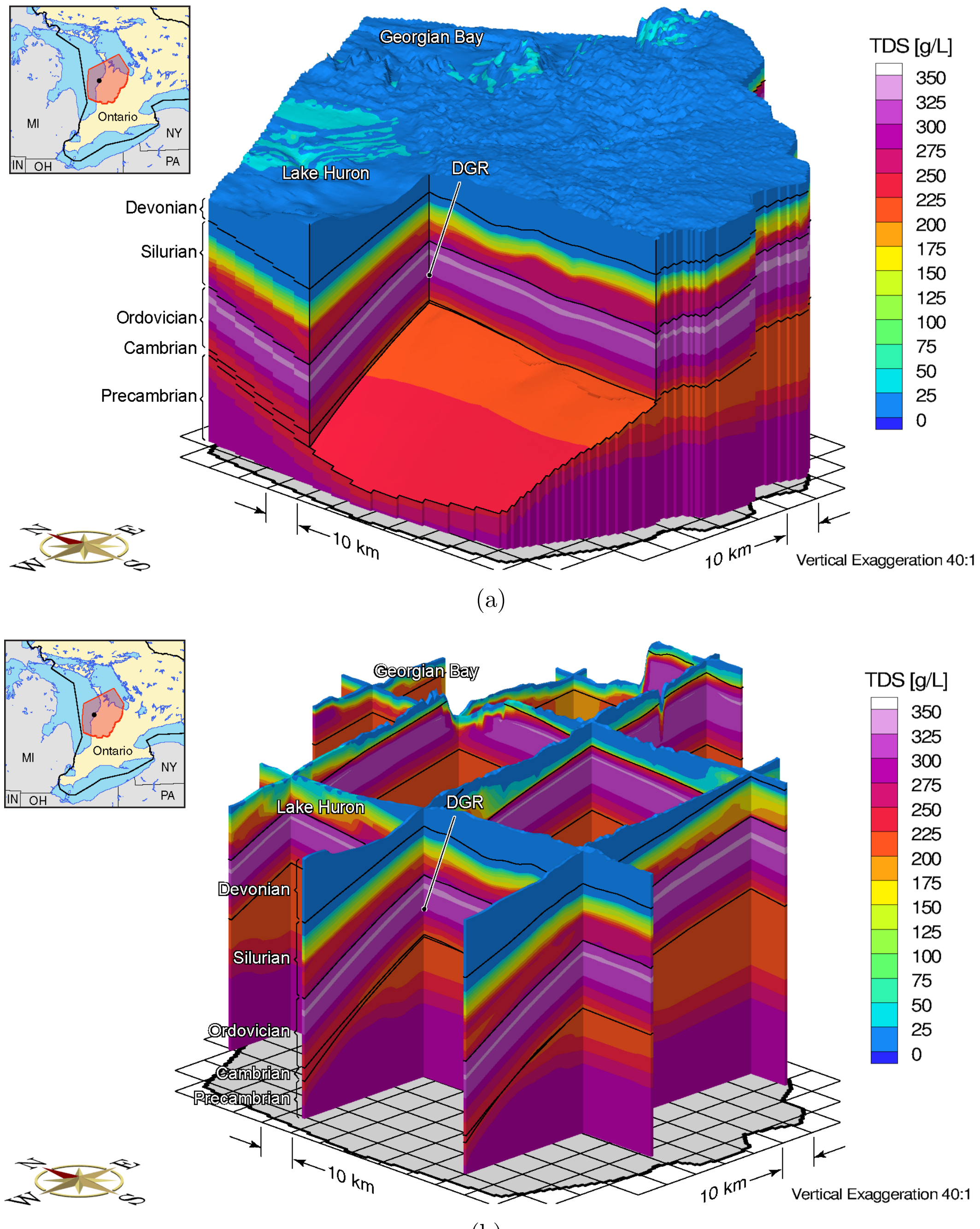

(a)

(b)

Figure B.6: Salinity (TDS) distribution across the regional-scale model domain at 19.5 ka before present, presented using a) block-cut and b) fence diagrams

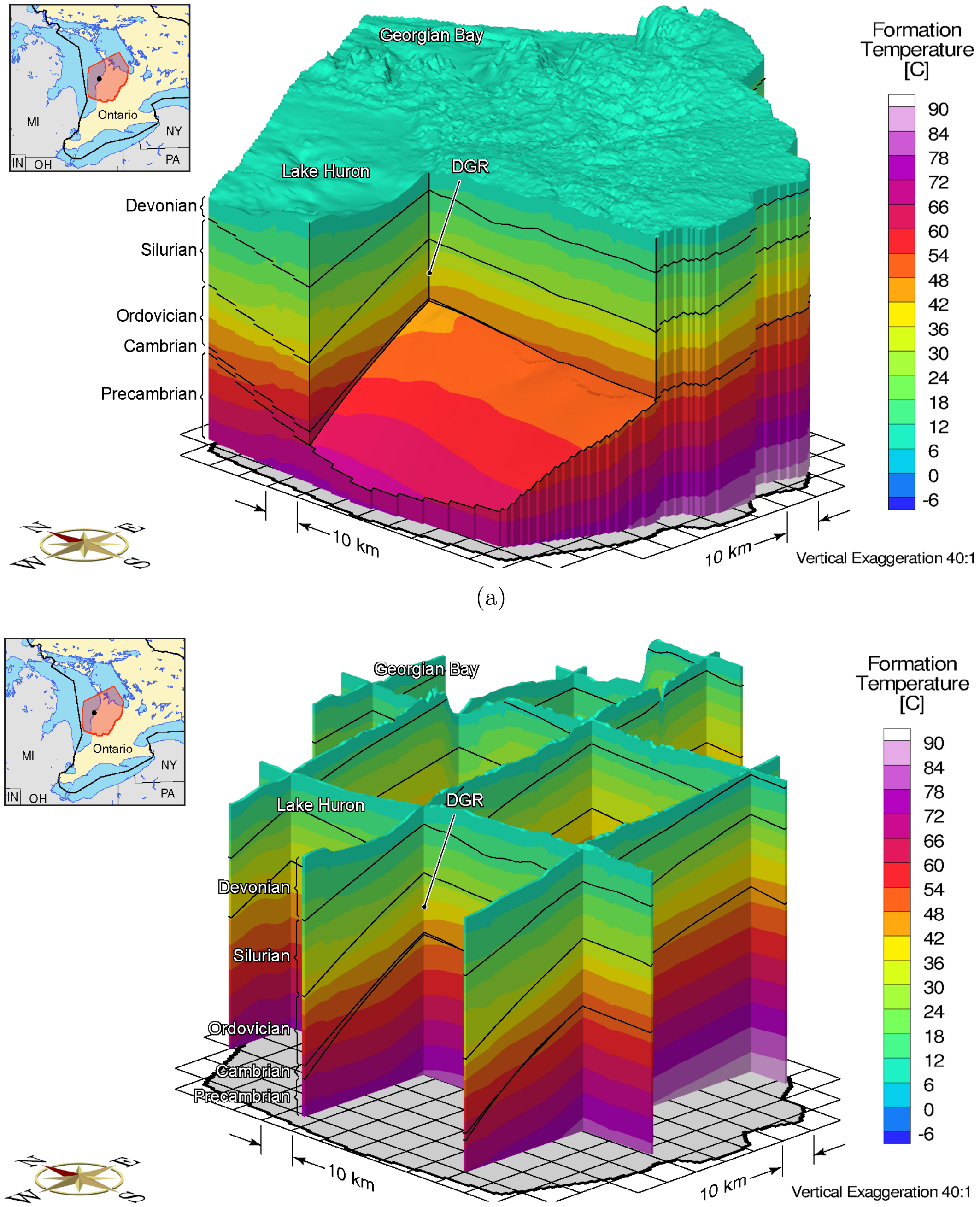

Figure B.7: Initial temperature distribution across the regional-scale model domain, presented using a) block-cut and b) fence diagrams

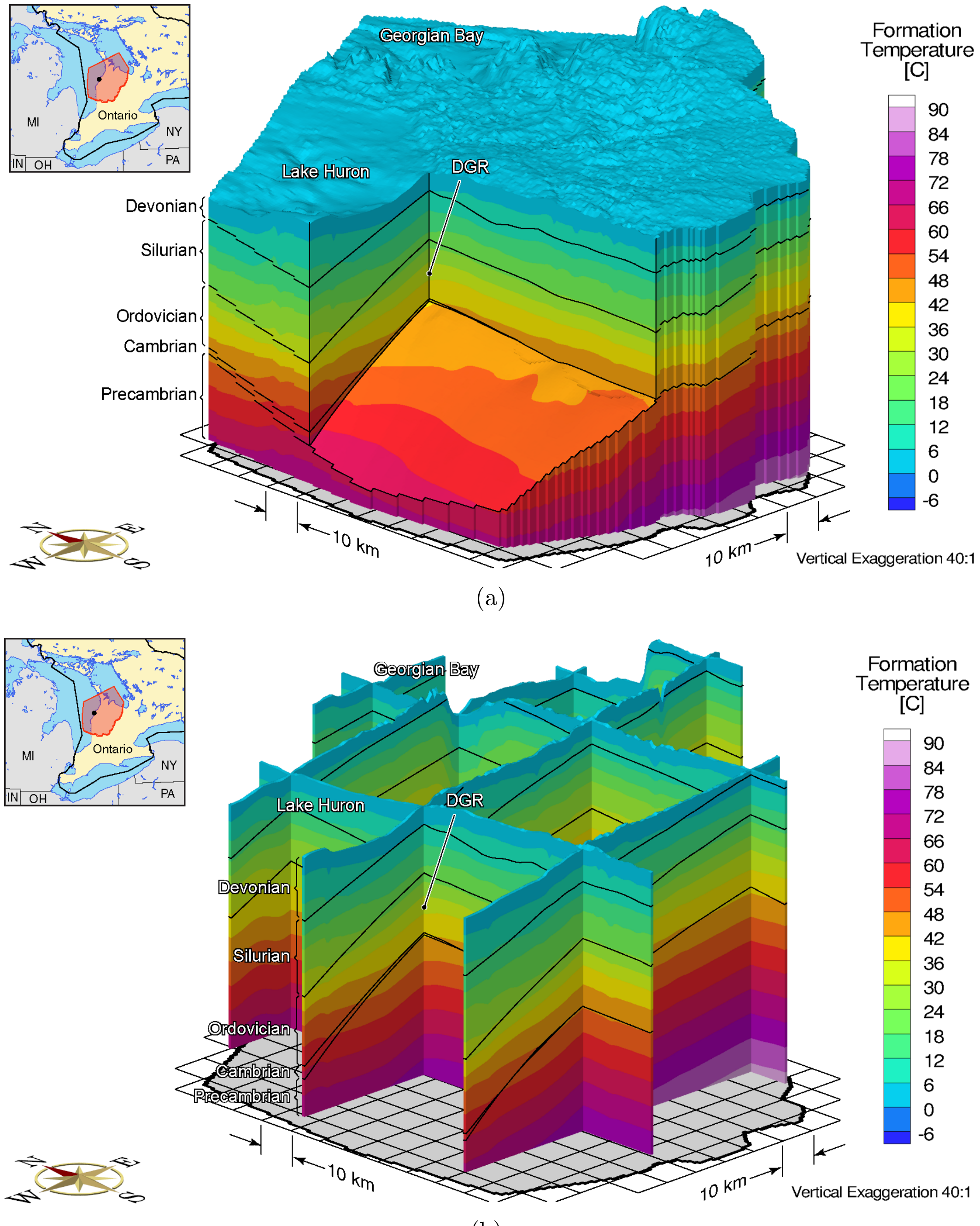

(a)

(b)

Figure B.8: Temperature distribution across the regional-scale model domain at 58 ka before present, presented using a) block-cut and b) fence diagrams

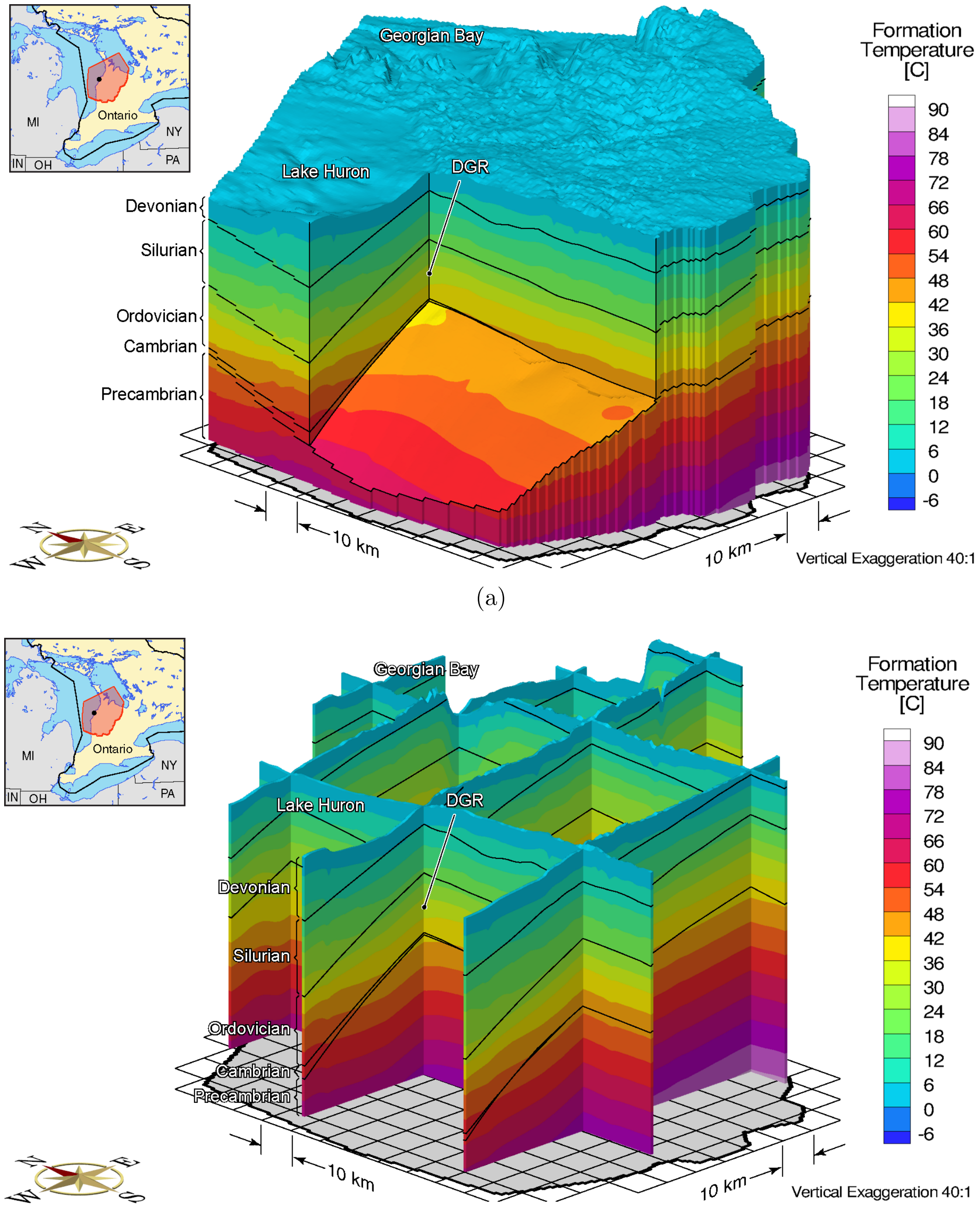

(a)

(b)

Figure B.9: Temperature distribution across the regional-scale model domain at 19.5 ka before present, presented using a) block-cut and b) fence diagrams

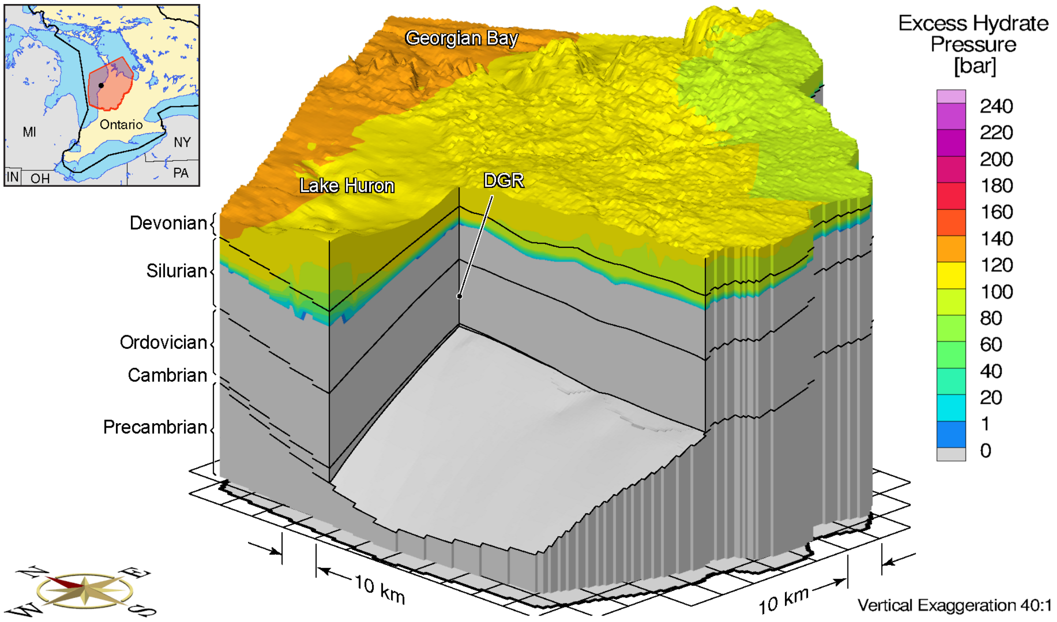

(a)

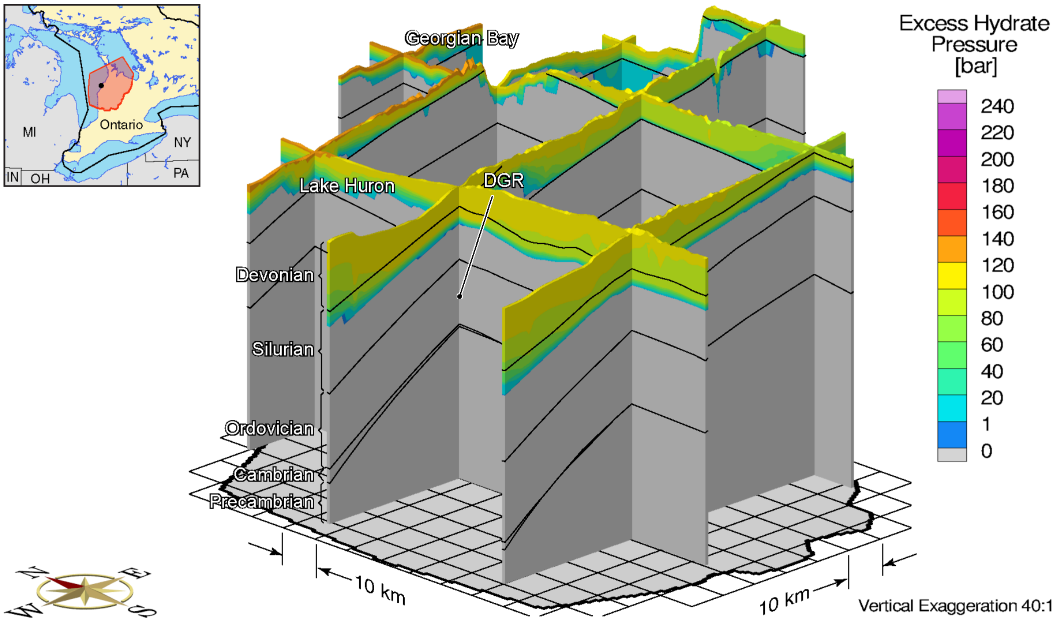

(b)

Figure B.10: Extent of potential hydrate stability zones across the regional-scale model domain at 58 ka before present, presented using a) block-cut and b) fence diagrams

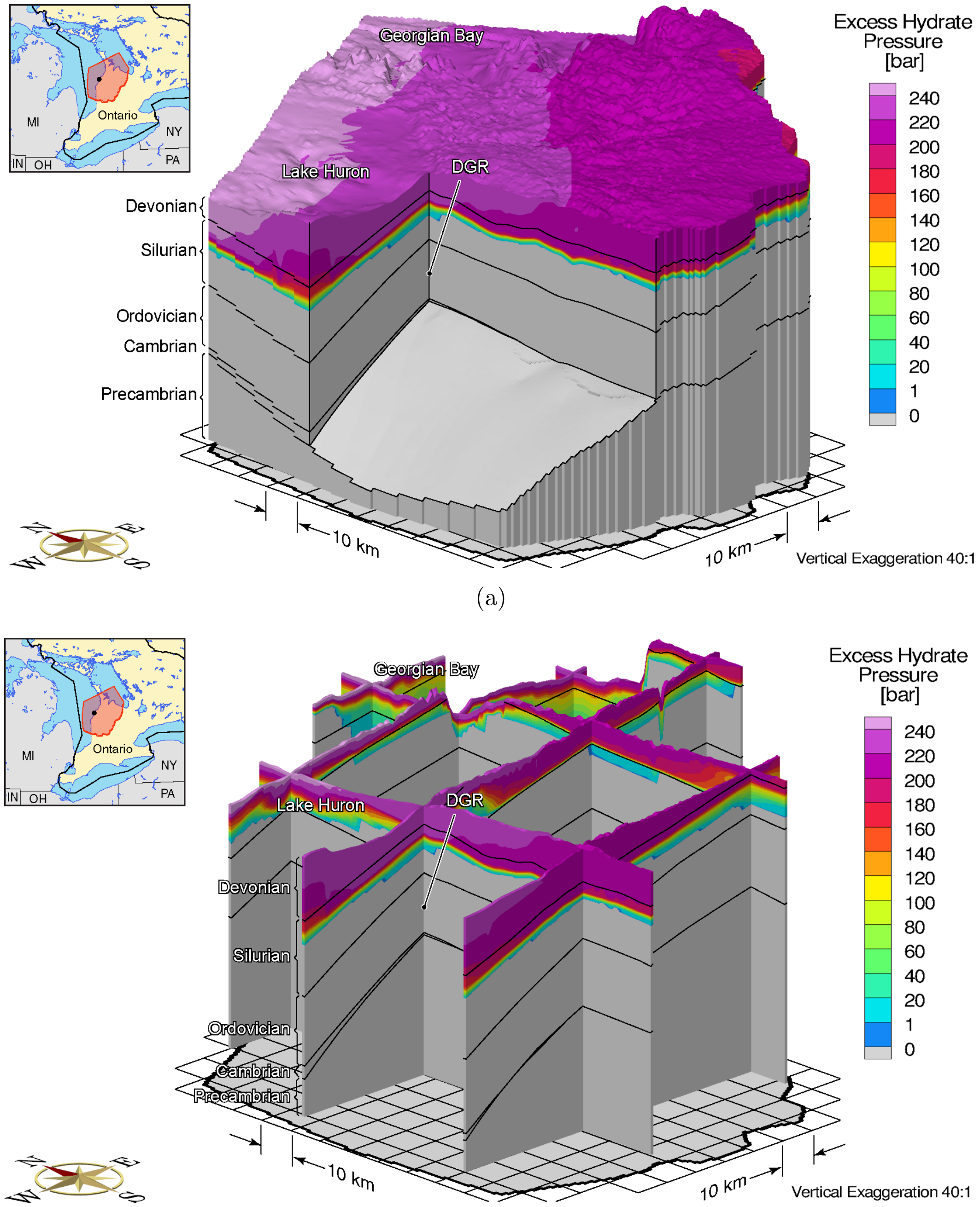

(a)

(b)

Figure B.11: Extent of potential hydrate stability zones across the regional-scale model domain at 19.5 ka before present, presented using a) block-cut and b) fence diagrams

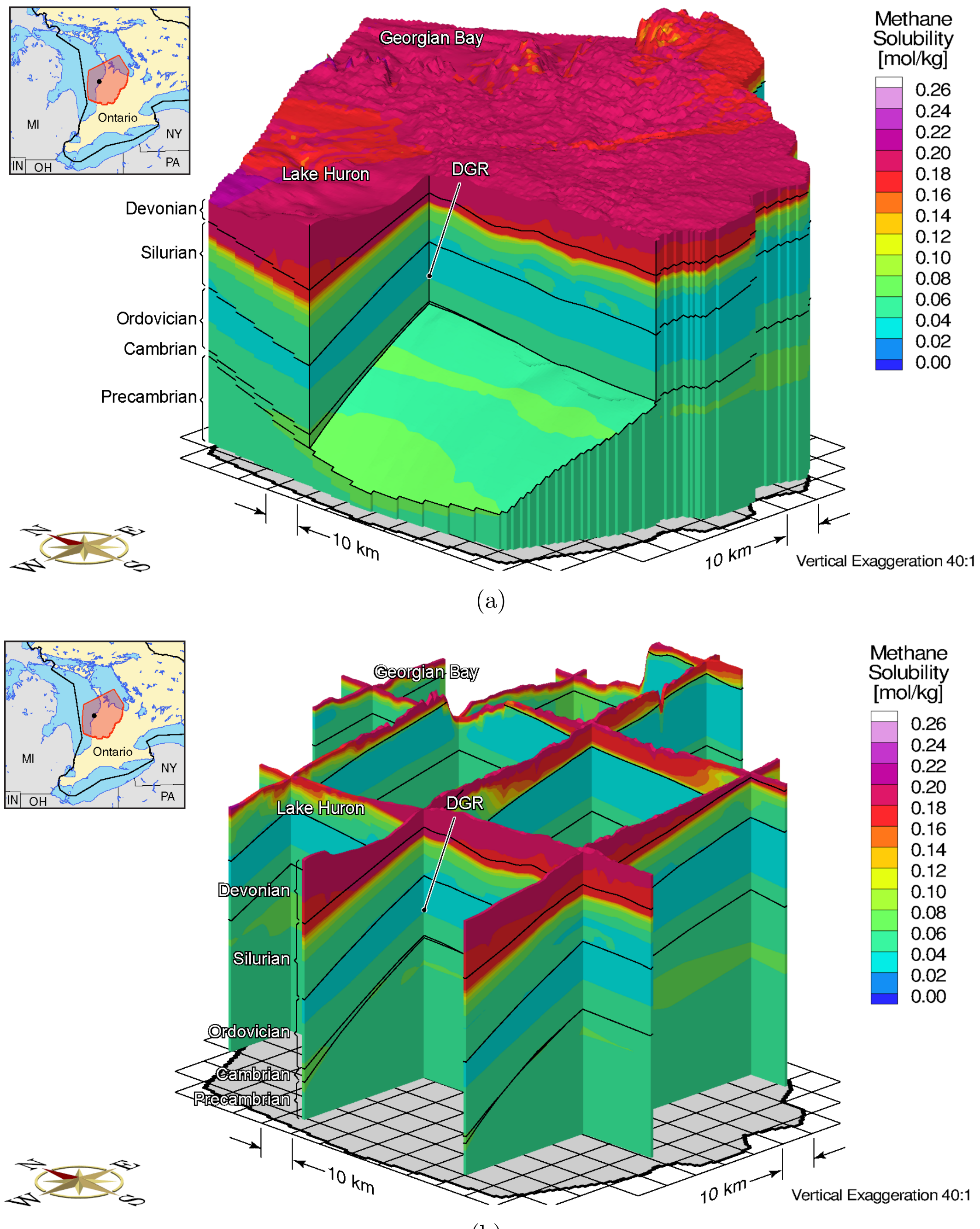

(a)

(b)

Figure B.12: Predicted solubility of methane gas across the regional-scale model domain at 58 ka before present, presented using a) block-cut and b) fence diagrams

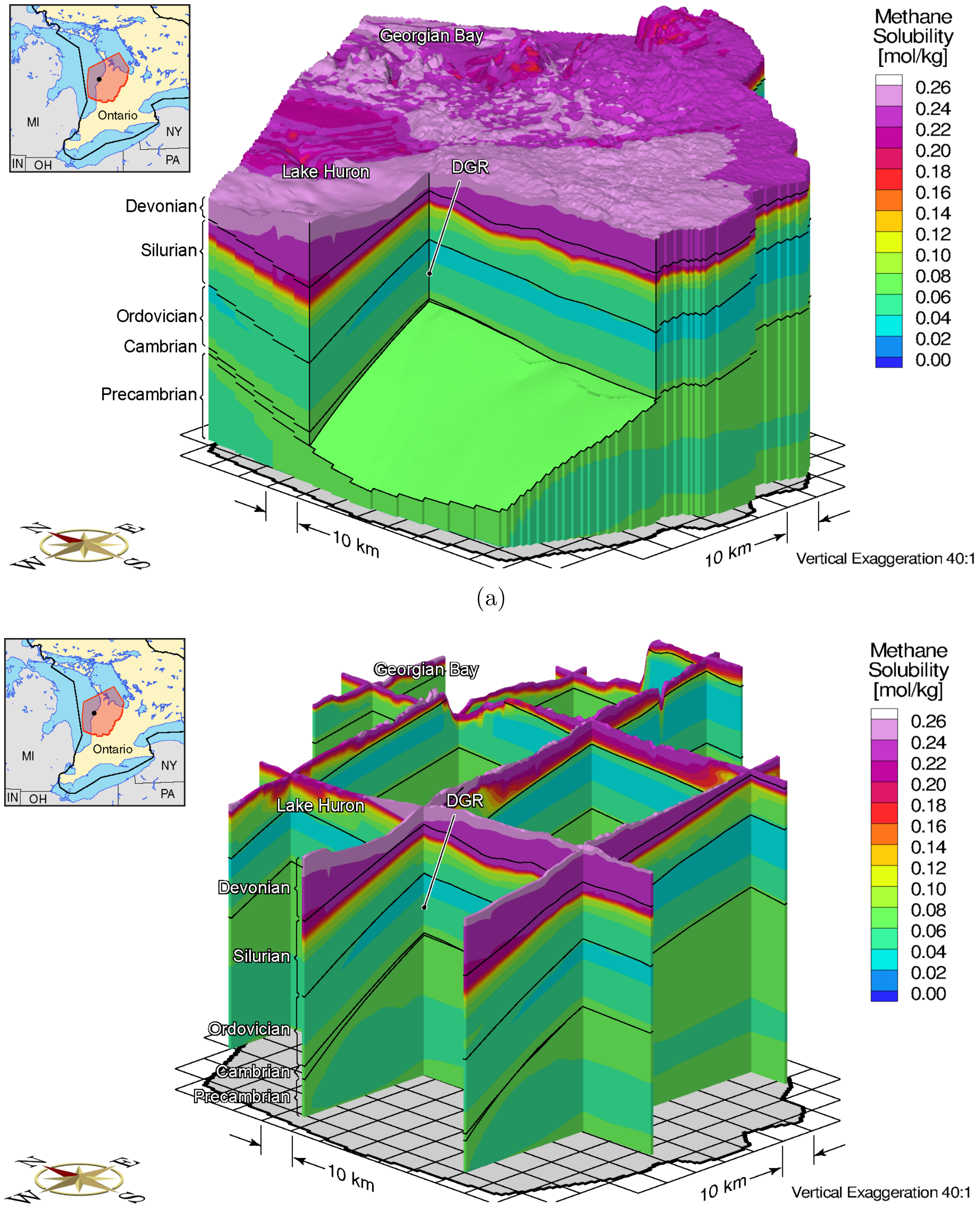

(a)

(b)

Figure B.13: Predicted solubility of methane gas across the regional-scale model domain at 19.5 ka before present, presented using a) block-cut and b) fence diagrams